Nano-scale Lithography and Microscopy of Organic Semiconductors

Dan Credgington

University College London, 2010

A dissertation submitted for the degree of Doctor of Philosophy

Acknowledgements

Over the (long!) years of this degree, I've been very fortunate to work with some wonderful and talented people; in particular I'd like to thank Lisa, Gustaf, Mar, Laurent and all the various denizens of the LCN for providing not only a stimulating scientific environment, but also some light relief from the dark of the SNOM lab. I especially want to thank Olly, for spending so much time in it with me, and keeping me sane throughout. My biggest thanks go to Franco, for his experience, support, ideas and patience, not to mention the many excuses he found to fund my trips to conferences, workshops and schools.

Finally I'd like to thank my parents, and especially Claire, for supporting me unwaveringly for so long, and pushing me to finish the job. For this and more I am truly grateful.

I, Dan Credgington confirm that the work presented in this thesis is my own. Where information has been derived from other sources, I confirm that this has been indicated in the thesis.

Abstract

The development of organic electronic and photonic devices increasingly requires the development of micro- and nano-structured morphologies, which in turn require the development of both prototyping and scalable patterning methods.

This thesis presents investigations which explore and develop unconventional patterning techniques for a variety of conjugated polymers and organic molecules, using scanning near-field optical lithography (SNOL), scanning thermal lithography (SThL) and molecular self-assembly. Optimised formation of organic nanostructures is demonstrated, at resolutions which equal or better the current state of the art, with patterning resolution for isolated structures below 60nm for SNOL and 30nm for SThL. SThL in particular is demonstrated as a technique which can achieve serial write-speeds of over 100 µm/s, with significant potential for up-scaling. Furthermore, arbitrarily defined two-dimensional large-area nanostructures up to 20 × 20 µm are demonstrated using SNOL while maintaining both high resolution and the integrity of the probe. The nanostructures fabricated in the course of this work, and others, are characterised using both optical and topographic techniques, primarily atomic force microscopy and near-field microscopy.

The detailed formation mechanisms for structures fabricated using SNOL via an in-situ conversion route are systematically investigated and contrasted with other formation routes, resulting in a comprehensive account of the factors affecting structure morphology. In addition, the optimised nanostructures achieved in this work are shown, within this context, to be very close to best achievable with an apertured scanning near-field system.

Table of contents

1. Introduction

1.1. Overview

This thesis is primarily concerned with the study of the abilities and limitations of the Scanning Near-field Optical Microscope (SNOM) both as a microscopy and as a lithography tool. The wider theme of this work is to explore and develop unconventional patterning techniques for a variety of conjugated polymers and organic molecules, using not only the SNOM, but also scanning thermal probes and molecular self-assembly. The following work is split into several sections, beginning with an introduction to the history, chemistry and applications of organic semiconductors, with a particular emphasis on conjugated polymers. In addition, the lithography work reported here is placed within the context of other lithography techniques.

In section 2, the theory underpinning the near-field microscope system is detailed, along with the attempts that have been made to model the behaviour of near-field probes. In section 3, the SNOM system used for the majority of these investigations is described. The remaining four sections describe the experimental investigations conducted using the SNOM, in addition to the other techniques mentioned above.

Section 4 represents the main focus of this thesis, exploring the ability of the SNOM system to be used as a direct-write lithographic tool for arbitrary patterning of organic semiconductor thin films. A number of different organic molecules and photo-patterning approaches are examined and contrasted. In particular, the detailed structure formation mechanism for one common polymer system is examined, and the practical and theoretical limits to patterning resolution are established. It is shown that the patterning resolution for isolated-features demonstrated in these investigations is very close to the minimum achievable with an apertured probe system.

Section 5 describes the related direct-write technique of Scanning Thermal Lithography (SThL) as a possible complement or alternative to near-field optical lithography. State-of-the-art patterning resolution for isolated structures is demonstrated both for micro-scale and nano-scale thermal probes, and routes for optimising this resolution further are identified.

Section 6 changes emphasis, and illustrates the use of the SNOM system for the microscopy of micron-scale self-assembled structures. In addition to exploring the capabilities of the SNOM system and demonstrating sub-wavelength resolving power, the limitations of apertured optical probes are highlighted, and possible solutions described.

Finally, in section 7, modelling work is presented showing that a particular type of self-assembled supramolecular fibres, deposited on top of patterned electrode structures, align with the weak local electric field. This in turn confirms that electric-field assisted alignment is a potential route to controlled patterning for this material.

However, before describing these results, I will first cover the work which underpins all of these investigations, beginning with a description of the particular group of organic semiconductors comprising the conjugated polymers. While this thesis is primarily concerned with the manipulation and measurement of conjugated polymer systems, where appropriate, references are made to conjugated small-molecule systems which exhibit similar behaviour.

1.2. Conjugated polymers

Conjugated polymers form a subset of the organic polymers, being long-chain carbon-based macromolecular systems. They are characterised by the presence of a delocalised π-electron systems, comprising (typically disordered) groups of related orbitals extended along each molecule, analogous to band structure in crystalline semiconducting materials. Continuing this analogy, a forbidden region can develop between the ground-state of the chain, or highest occupied molecular orbital (HOMO) and the first excited state, or lowest unoccupied molecular orbital (LUMO), which behaves similarly to the band-gap in crystalline materials. In the typical case that the Fermi level for the electrons in the system lies between the HOMO and LUMO, the conjugated polymer acts as an intrinsic semiconductor, allowing complex interactions with light and charge.

The utilisation of conjugated polymers, typically as dyes and phosphors, extends for over a century, with reports dating back to the 1860s describing the synthesis of a substance which would later be identified as the conducting polymer polyaniline [1]. However, it is the use of conjugated polymers in their role as organic semiconductors with which this thesis is primarily concerned. The initial identification that polymeric conductors existed was made in the middle of the 20th century, with various reports of conducting plastics and interest in the possibility of achieving superconductivity in organic materials [2]. Partly as a result of this increase in focus, some of the first widely reported (and peer reviewed) progress on optimising conducting polymers was made during the 1960s. Examples include the description of metallic conduction in iodine-doped polypyrrole in a number of papers by Bolto and McNeill [3] and reports on the use of conducting polyaniline, including its use as a plastic electrode – reviewed in [4]. The first polymer electronic devices were reported soon afterwards, with the demonstration of a voltage-controlled switch based on the mixed copolymer dopamelanin by McGinness and co-workers [5]. In 1977, MacDiarmid and co-workers reported metallic conductivity in iodine-doped polyacetylene, crucially demonstrating control over the resulting material properties sufficient to allow a full transition from insulator to metallic conductor [6]. This, and related, work eventually led to the award of the 2000 Nobel Prize for Chemistry to Heeger, MacDiarmid and Shirakawa.

In addition to this work on metallic polymers, it was the development of organic semiconductors in their role as electronic materials which further spurred their development. The shift in focus to device-based applications (rather than, for instance, transparent metallic coatings etc.) occurred during the late 1980s, with multiple demonstrations of the potential for incorporating organic materials into functional devices including transistors [7] and organic light-emitting diodes (OLEDs) [8, 9].

The use of these materials as a parallel technology to conventional inorganic semiconductors has continued to foster intense study, due to their continuously improving optoelectronic properties and solution processability [10]. The last two decades have seen ongoing developments in polymer electroluminescence [11, 12] transistor action [13], photovoltaic action [14], lasing [15] and amplification [16], with an increasing focus on technological development and commercialisation.

1.3. Chemistry

The semiconducting and metallic organic materials (and specifically conjugated polymers) referred to above are based on chains and sheets of sp^2 hybridised carbon. Neutral carbon contains six electrons, two tightly bound in 1s orbitals and four valence electrons in a $2s^2$, $2p^2$ configuration. This configuration is only maintained in atomic carbon (outside of any molecule or crystal), in a carbon-based molecule the total bond energy may be reduced by the formation of “sp” hybrid states between the filled 2s- and partially filled 2p-shells. Three primary hybrid states are possible: 1) tetrahedrally aligned sp^3 orbitals as found in diamond and saturated polymers, 2) planar hexagonal sp^2 orbitals as found in graphite, and organic semiconductors and 3) linear sp orbitals as found in linear acetylenic carbon, and in the terminal alkyne groups of the building blocks used in copper-catalysed “click” chemistry. Schematics of these configurations are shown in Figure 1.1 below.

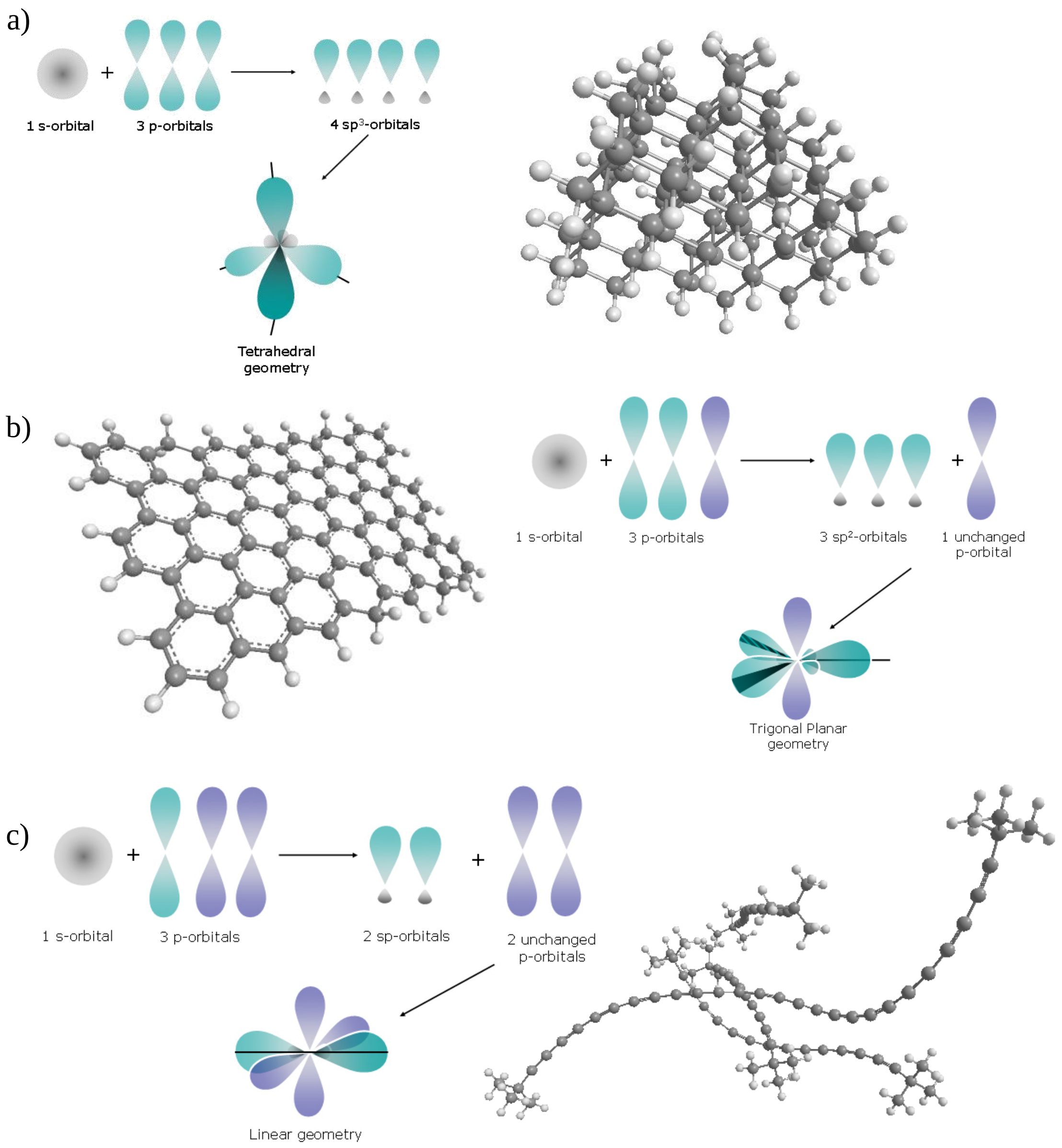

Figure 1.1: Schematics of the orbital structures of a) sp^3 hybridisation b) sp^2 hybridisation and c) sp hybridisation, along with examples showing the a) diamond, b) graphene and c) linear acetylenic carbon structures. Orbital diagrams reproduced from the Nottingham Trent CELS resource.

Since only three of the four valence electrons hybridise in the sp^2 configuration, the final electron occupies a perpendicular 2p orbital. The sharing of sp orbitals between adjacent carbons leads to strong σ-bonding, which allows the formation of long carbon chains, sheets and branched structures. Overlap between 2p orbitals leads to weaker π-bonding, encouraging a preferred orientation between the main σ-bonded "backbone" units but not otherwise greatly affecting the physical structure of the molecule. This preferred orientation encourages planarisation of the molecule and, consequently, allows delocalisation of π-electron states over many carbon atoms. It is this propensity to develop conjugated systems of overlapping π-bonds which leads to the semiconducting properties and rich photophysics seen in conjugated organic molecules.

With no delocalised states, sp^3 hybridised polymers, such as polyethylene, are good electrical insulators. However, conjugated sp^2 hybridised systems can exhibit semiconducting or metallic properties. By analogy with inorganic crystalline band-structure, the mixing of p-states in conjugated systems leads to bands of closely spaced molecular orbitals allowing conduction of charge throughout the conjugated sections of molecule. This does not necessarily lead to high conductivity however: in a typical organic semiconductor, the HOMO is primarily formed of π-bonding orbitals, while the LUMO is formed primarily of π*-antibonding orbitals, with a gap between them of approximately 1-3 eV. Under normal conditions, thermal excitation from the filled HOMO to the unfilled LUMO is negligible and the material acts as an intrinsic semiconductor. Doping of the molecule, or injection of external charge, is therefore necessary to initiate and exploit its conductive properties. In addition, each conjugated region will likely not extend over the whole molecule, due to energetic disorder – twists and folds in the structure break the symmetry of the overlapping π-orbitals, forcing carriers to tunnel from one conjugated region to the next. As a result, the highest conductivities reported in conjugated polymers are for stretch-oriented films with low inherent defect densities [17].

1.4. Excited states and optoelectronic properties

Optical excitation in conjugated materials occurs by absorption of light with photon-energy greater than the HOMO-LUMO gap, promoting charge from the lowest vibrational-energy electronic ground state to one of the manifold vibrational sub-states of the first electronic excited state. In general, absorption is followed by rapid equilibration and decay to the lowest-energy vibrational sub-state within the excited electronic state, resulting in a relaxed singlet electron-hole pair (exciton). Recombination of this bound pair can occur to one of the manifold vibrational sub-states of the ground-state, either non-radiatively via emission of phonons (typically assisted though interaction with inter-gap defect or impurity states) or, more usually, radiatively across the HOMO-LUMO gap via emission of a photon (fluorescence). Since electronic transitions are fast compared to nuclear rearrangement of the absorbing/emitting molecule (the Franck-Condon principle), the relative oscillator strength for transitions between the ground/excited vibrational sub-states is governed by the instantaneous overlap between electronic wave functions. A schematic of the contributions each vibrational-electronic transition makes to the resulting absorption and emission spectra is presented in Figure 1.2.

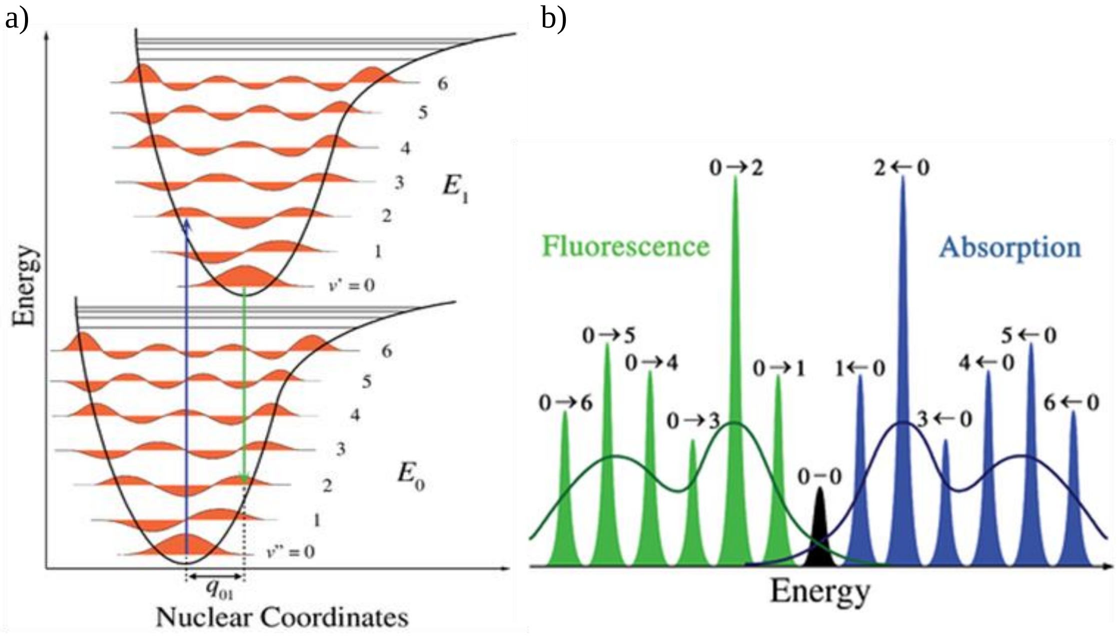

Figure 1.2: a) Schematic of the electronic (E_i) and vibrational (v) energy levels for a general molecule within the Franck-Condon model. The particular shift in relaxed nuclear coordinates upon excitation from E_0 to E_1 has been chosen to provide maximum overlap between the $v = 0$ and $v = 2$ vibrational states, with no change in the shape of the potential upon excitation. b) Reconstructed absorption and fluorescence spectra based on a superposition of the transitions available in a), with strength determined by wave-function overlap. Idealised spectra for homogeneously-broadened molecules in the gas phase are shown in lighter colours, inhomogeneously broadened spectra, as might be expected in the solid state, are shown as darker lines. Original figures made available by Mark M. Somoza under the Creative Commons Attribution ShareAlike Licence.

Migration of excitons through the semiconducting medium occurs via transfer of the bound pair from one conjugated molecule/chain segment to another by either Förster energy transfer [18], involving short range dipole-dipole interactions (equivalent to the exchange of a virtual photon) or Dexter energy transfer [19], involving direct exchange of electrons. Since Dexter transfer requires overlap between the donating and accepting species, whereas Förster transfer requires only coupling of dipoles, Dexter transfer is typically only dominant in situations where optical transition are forbidden, for example in the migration of triplet-excitons (generated by intersystem crossing by singlets, or coulomb-capture of free carriers)

Organic semiconductors typically display low dielectric constants (e.g. $\varepsilon_{\text{Pentacene}} \sim 4$, $\varepsilon_{\text{PPV}} \sim 2$ [20]) compared to inorganic crystalline semiconductors (e.g. $\varepsilon_{\text{Silicon}} \sim 12$, $\varepsilon_{\text{GaAs}} \sim 13$), which has a significant effect on the resulting excited-state behaviour.

In materials with a high dielectric constant, screening reduces the effective Coulomb attraction between the electron-hole pair, leading to excitons with very low binding energies and characteristic radii greater than the material's lattice spacing – i.e. they are delocalised over many unit cells. This subset of excitons, described by and named after Gregory Wannier [21], are characterised by binding energies of a few k_BT[*] at room temperature, and may thus undergo spontaneous dissociation into free charges via interactions with lattice phonons.

In materials with small dielectric constant, the coulomb interaction between electron and hole is not strongly screened, leading to tightly bound Frenkel-type excitons (after Jakov Frenkel who first described localised excited states in crystals in terms of "excitation waves" [22]) with binding energies of order 0.1-1 eV and characteristic radii of the same order of the unit cell (for crystals) or individual monomers/molecular units (for molecular materials). Dissociation of these excitons into free charge carriers is therefore not typically spontaneous, and must be achieved in other ways, such as the use of heterojunctions as described in section 1.6.2.

Charged excitations formed by dissociation of excitons, or direct injection from the electrodes in the case of devices, cannot usually be described as free charges in the same sense as the delocalised charge carriers associated with crystalline semiconductors. Instead, electrons and holes moving through an organic material are typically coupled to an associated "cloud" of phonons representing the molecular distortion induced both by polarisation of the surrounding medium and the breaking of local conjugation by the

---

[*] $k_B = 1.3806503 \times 10^{-23}\ m^2\ kg\ s^{-2}\ K^{-1}$

occupancy of the π* anti-bonding state. The fundamental charge carrier in organic materials is thus a quasiparticle, comprising the charge self-localised by its associated lattice/chain distortion – a polaron. The “binding” energy of the polaron (as compared to the energy of a free charge without distortion) is determined by the competition between energy gained by relaxation of the surrounding medium around the charged excitation and energy lost due to the resulting decrease in charge delocalisation. A consequence of this self-localisation is that the migration of polarons between polymer chains or conjugated regions involves a significant reorganisation energy and is limited by the electronic coupling between conjugated regions. As such, charge transport in disordered organic materials (such as those deposited from solution, as described in this work) occurs via a thermally-assisted hopping process, whereby polarons are relatively free to move around conjugated regions, but must jump directly to adjacent molecules/chain/regions in order to move through the bulk. Mobility in organic samples has therefore been found to be highly sensitive to processing conditions and material purity, which lead to variations in crystallinity, packing, disorder and polaron trap states. A pair of comprehensive reviews detailing the progress made in measuring and understanding charge transport and charge mobility in organic semiconductors have been presented in recent years by Brédas and co-workers [23, 24]

1.5. Polymer blends

For a wide range of applications, utilising combinations of materials rather than pure substances can produce advantageous physical or chemical properties which are absent or poorly expressed in their component parts. Examples include metal alloys, mechanical composites and liquid mixtures and can also apply to combining different polymers in a blend. A common mechanical example is the blending of tough rubber and stiff polystyrene to form the two-phase structure of high-impact polystyrene. Many of the organic photovoltaic devices described in section 1.6 rely on a two-phase blend of semiconducting polymers or small molecules to form their active layer. Homogeneous mixtures are also common, and may likewise display useful properties absent in the component parts – Poly(3,4-ethylenedioxythiophene): poly(styrenesulfonate) (PEDOT:PSS) is one such example, the two component ionomers exchanging charge to create a soluble, conductive composite.

Understanding the behaviour of polymer blends is therefore important in understanding their use in devices and in the nano-scale manipulation of their structure. To model the mixing process for two polymers, I follow here the scheme outlined in two papers published simultaneously in 1941 by Flory [25] and Huggins [26]. The Flory-Huggins approach gives a basic understanding of the possible behaviours and phases in a two-component blend by modifying the expression for the Gibbs free energy of a mixture to include molecules of dissimilar sizes.

The Gibbs free energy of a particular system is given by the difference between its enthalpy, H, and TS, a measure of the system's disorder, where T is temperature and S the entropy of the system.

$$G = H - T \tag{1.1}$$

This quantity estimates the useful energy currently available to a system, either to do work or to allow transitions to other states. The change in free energy, ΔG, encountered when moving from one state to another is therefore an indication of the nature of the transition: only transitions for which $\Delta G < 0$ are thermodynamically favourable. For a mixture, an initial state of a pure A phase and a pure B phase, and a final state of a mixed AB phase is considered. The change in free energy upon mixing is thus given by:

$$\Delta G_{MIX} = G_{AB} - \left(G_A + G_B\right) \tag{1.2}$$

Where G_i is the free energy associated with state i. In the Flory-Huggins approximation, ΔG_{MIX} is considered as a sum of two terms which capture the main changes in the system due to mixing:

$$\Delta G_{MIX} = \Delta G_{LOCAL} - T\Delta S_{TRANS} \tag{1.3}$$

captures the changes to the local chemistry and motions of the mixed units, including any changes to the local entropy due to volume changes, and ΔS_{TRANS} captures the change in translational entropy of the system. By approximating local interactions as arising from a mean-field originating from the rest of the mixture, and also that these are primarily enthalpic, it can be shown that:

$$\frac{\Delta S_{TRANS}}{R} = -n_A \ln \phi_A - n_B \ln \phi_B \tag{1.4}$$

where n_A and n_B are the molar quantities of components A and B, with ϕ_A and ϕ_B their volume fractions and R the molar gas constant. It may further be shown that:

(1.5) $$\Delta G_{LOCAL} = RT\frac{V}{v_c}\chi\phi_A\phi_B$$

where V is the volume of the system, v_c the molar volume of a reference unit common to both materials (generally taken for two polymers to be the volume of a single monomer) and χ the dimensionless 'Flory-Huggins' parameter, which represents the change in local free energy per reference unit. Together they give:

(1.6) $$\Delta G_{MIX} = RT\left(\frac{V\chi}{v_c}\phi_A\phi_B + n_A \ln\phi_A + n_B \ln\phi_B\right)$$

Considering the specific case of a two-polymer mixture, (1.6) may be expressed in more convenient terms by introducing n_c, the number of moles of reference unit, $v_{A,B}$ the molar volumes of polymers A and B and $N_{A,B}$, the degree of polymerisation of polymers A and B:

(1.7) $$v_{A,B} = V\frac{\phi_{A,B}}{n_{A,B}} \qquad n_c = \frac{V}{v_c} \qquad N_{A,B} = \frac{v_{A,B}}{v_c} = \frac{v_{A,B}n_c}{V}$$

So that:

(1.8) $$\Delta G_{MIX} = RTV\left(\chi\phi_A\phi_B + \frac{\phi_A}{N_A}\ln\phi_A + \frac{\phi_B}{N_B}\ln\phi_B\right)$$

Noting that mixing will only occur if $\Delta G_{MIX} < 0$, there are two important conclusions that can be drawn from this expression. The first is that, unlike for small molecules, the increased translational entropy associated with mixing is not necessarily sufficient to guarantee miscibility for incompatible polymers. As $N_{A,B}$ tends to infinity (corresponding to large degrees of polymerisation), the motion of the polymer chains is severely restricted and translational entropy plays little part. The second is that, if changes in translational energy may be neglected, local interactions between monomer units, represented by χ, dominate the mixing. Negative χ (corresponding to monomer units with a high degree of compatibility) necessarily encourages homogenous mixing whereas for most systems, and especially those with high degrees of polymerisation, positive χ precludes homogeneous mixing.

Importantly, the result of repulsive polymer-polymer interactions of the type described above is that a layer of two initially well mixed materials can lower its free energy via spinodal decomposition into a phase-separated morphology, with little entropic penalty. The resulting structure depends in detail on the nature of the mixed phases, but for a variety of applications can demonstrate significantly increased functionality over homogeneous blends. The demixing process can occur spontaneously or may be encouraged/influenced by physical interventions such as heating, solvent treatment or the inclusion of tertiary additives to the blend.

1.6. Organic semiconductor devices

One of the driving forces behind research into organic semiconductors, and semiconducting polymers in particular, has been the recognition of their potential to become a disruptive technology for low-mobility, large-area electronics applications. The two main device applications for organic semiconductors are OLEDs and solar cells, outlined below.

1.6.1. OLEDs

Since the discovery of efficient electroluminescence in poly(*p*-phenylene-vinylene) (PPV) [9], the primary commercial focus of polymer electronics has been the development of OLEDs, either for cheap, large area lighting or bright, low power (and potentially flexible) displays. Progress towards marketable OLED technologies has been rapid in the last decade, with the development of monochrome OLED displays quickly giving way to small-scale full-colour for mobile-telephone and PDA screens. Laptop-scale prototypes were demonstrated by Samsung and Sony in the mid-2000s, while in 2010 Sony, Samsung and DuPont all exhibited home-cinema-scale displays from 30”-50”, and Sony have revealed the first prototype 3D-OLED television. The primary reason for this strong focus on OLED development has been that the competing silicon- or III-V-based LED technology is suitable only for LCD displays, due to the prohibitive cost of producing multi-coloured active-matrix inorganic LEDs. The relatively low cost of OLED fabrication, combined with tuneable colour emission through molecular engineering and the extremely high contrast which results from switching from LCD to

LED technologies are the main commercial drivers, with the additional potential for building the displays on flexible substrates still in its relative infancy.

OLEDs are a thin-film technology, with the device consisting of an emissive layer sandwiched between a pair of electrodes. For polymer OLEDs (PLEDs) this emitter is typically spin-cast or inkjet-printed from solution on to a transparent conducting substrate such as indium tin oxide (ITO) on glass, and capped with an evaporated low work function cathode. The operating principle for an OLED is that electrons are injected preferentially into the emitter LUMO, while holes are preferentially injected into the emitter HOMO. Under these conditions, electrons and holes drifting through the device can form bound excitons across the HOMO-LUMO gap, which can in turn recombine radiatively to produce light. A schematic of an OLED device is shown in Figure 1.3.

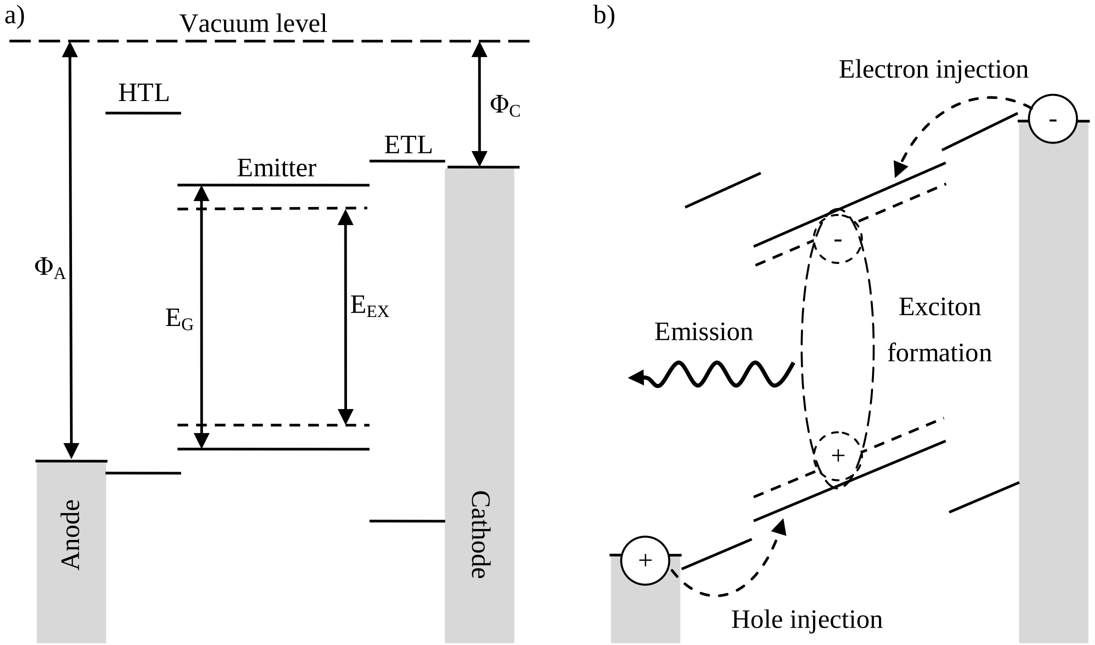

Figure 1.3: Schematic of an OLED device (energy vertical) under a) zero bias and b) forward bias, showing the device structure, electrode work functions $\Phi_{A,C}$, HOMO-LUMO gap E_G and exciton energy E_{EX}. Emission is typically through the (transparent) anode.

Several enhancements are possible to improve the electroluminescent efficiency. To ensure efficient preferential injection, dissimilar electrodes with work functions closely matching the HOMO/LUMO levels are chosen, with additional modification of the electrode work functions often achievable via the insertion of thin interlayers. The use of dedicated hole-transporting/electron blocking or electron transporting/hole blocking interlayers (HTL and ETL, respectively) either side of the emitter can reduce the amount of charge which escapes the device without recombining, and prevent exciton quenching at the electrodes. Finally, since statistically it is expected that only 25% of the excitons formed in the emitter will be fluorescent singlets, with the remainder being longer-lived phosphorescent triplets, the photon yield can be improved though the use of heavy metal complexes to enhance the efficiency of intersystem crossing and reduce competing triplet-triplet annihilation [27].

1.6.2. Photovoltaic cell

Organic photovoltaics (OPVs), like their inorganic counterparts, are primarily designed to absorb light energy and convert it into electrical energy, either for power generation (as a solar cell) or light sensing (as a photodetector). Their operating principle is essentially opposite to that of the OLED, in that excitons formed by the absorption of light must be separated, and the charge carriers extracted at the appropriate electrodes while retaining as much of the incident photon energy as possible.

The simplest solar cell design uses a single layer absorber deposited between dissimilar electrodes which, upon equilibration, set up a built-in electric field across the device. This architecture is identical to that of the simplest OLEDs described above. In this configuration, bound electron-hole pairs (geminate pairs) are formed upon absorption of light with photon energy greater than the HOMO-LUMO gap. Given sufficient thermal energy, these bound charges can spontaneously separate and drift to the appropriate electrode under the influence of the built-in field. However, as hot excitons typically equilibrate on timescales faster than they can separate, and since the resulting relaxed excitons are strongly bound Frenkel-type, this process is far less efficient for organic semiconductors than for inorganic crystalline materials. The approach now taken in all current OPV devices to circumvent this problem is to employ a heterojunction structure as the active layer, with two dissimilar materials (the “donor” and “acceptor”) chosen such that an offset exists between their LUMO energies (and/or HOMO energies) sufficient to drive charge separation. An exciton diffusing to the interface between the two materials may lower its energy either by transfer of the electron polaron from the donor LUMO to the acceptor LUMO, or via transfer of the hole polaron from the acceptor to the donor, thereby physically separating the bound charges. Providing the resulting charge-transfer complex is sufficiently hot, or a sufficiently large built-in field exists, separation of the geminate pair can be extremely efficient [28]. Initially, heterojunction structures were achieved using small molecule bilayers. These have the advantage of being conducive to vacuum deposition, which permits high crystallinity and mobility, and so efficient extraction, but suffer from an active layer thickness limited by the exciton diffusion length [29]. Bulk heterojunctions formed from solution processable materials, including polymers, have more recently taken over as the most efficient cell technology. These greatly increase the volume of the absorbing layer which lies within an exciton diffusion length of the heterojunction interface, but suffer from lower mobility and increased bimolecular recombination which can limit the extraction efficiency. Nevertheless, with power conversion efficiencies increasing from 2.5% [30] to around 8% over the last decade [31], an increasing number of commercial companies are working towards bringing bulk-heterojunction OPV technology to market. Figure 1.4 presents a schematic of an organic heterojunction cell, with a summary of the processes involved in charge generation.

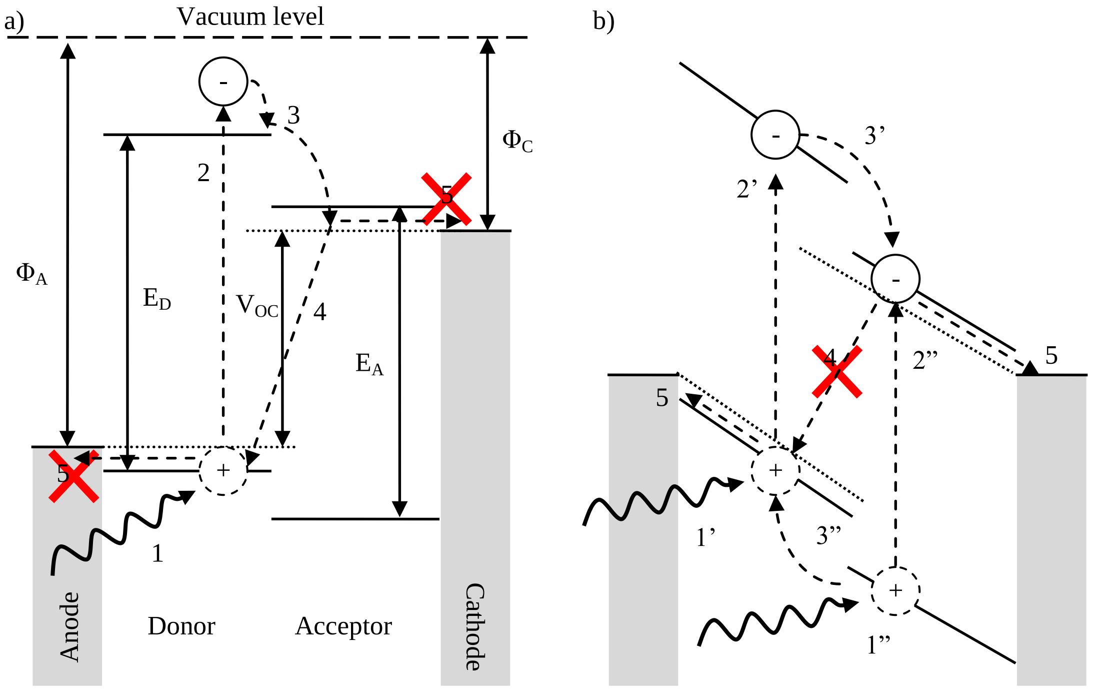

Figure 1.4: Schematic of a heterojunction solar cell (energy vertical) under a) open-circuit and b) short-circuit conditions. #, #' and #" indicate three possible pathways to recombination or extraction, dotted lines sketch the positions of the electron/hole quasi-Fermi levels under illumination. (1) Absorption in the active layer excites electrons across the donor/acceptor HOMO-LUMO gap E_D/E_A, forming a bound exciton which quickly equilibrates (2). If the exciton diffuses to the heterojunction interface, it will split, potentially creating a pair of free polarons (3). Under open circuit conditions (quasi-Fermi level splitting of V_{OC}), the majority of these polarons eventually recombine (4), with the few which reach the appropriate electrodes balanced by leakage through the device. Under short-circuit conditions, free polarons are typically swept out of the device by the built-in field before recombination can occur (5). Crosses indicate processes with minor importance.

1.7. Lithography techniques

Organic devices, and particularly polymer devices, are typically constructed using thin-film technology, primarily due to the strong optical interactions and relatively low mobilities associated with semiconducting polymers. While un-patterned films are sufficient for many large-area, low-cost applications [32], two-dimensional patterning over a range of length-scales is required for a number of more complex applications, such as multicoloured displays [33], "integrated plastic circuits" [34] and the fabrication of photonic structures [35, 36], in addition to the specific devices described above. For future applications in photonic devices and nanoelectronics, the ability to achieve lithographic resolution on the nano-scale is vital. The applications for high resolution lithography are limited only by the range of materials and lengthscales accessible by a particular technique, with current interest extending to the use of conjugated polymers in active systems such as nanoelectronics, nanophotonics, digital memory and spintronics, as well as passive systems such as microfluidics.

The result of patterning should be well-defined features fabricated from the active material with minimum physical and chemical damage to the material, since both can detrimentally affect its optoelectronic properties. To achieve this, a huge variety of techniques have been explored for patterning polymers, indicating the ongoing interest in the problem of how to pattern materials on the nanoscale. The range of techniques can be roughly divided into three families, summarised below.

Pre-patterned

Techniques which utilise pre-patterned substrates or stamps to guide or define the final structures, typically over large areas, such as site-selective chemical vapour deposition on patterned precursors [37], micro-moulding in capillaries [38], micro-contact printing [39], nanoimprint lithography [40, 41] and screen printing [42] as well as conventional etching and far-field photolithography still used in modern very-large-scale integrated circuits. The technique of holographic lithography [43] also fits loosely within this family, in the sense that a predetermined field structure is created and imposed on a sample.

Self assembly

Techniques which rely on a pre-formed or *in-situ* formed morphology to influence structure formation, including electrodeposition [44, 45], electrospinning [46] and all forms of aggregation in solution, including colloid, nanowhisker or vesicle formation.

Arbitrary

Techniques which pattern directly to an arbitrary design, typically over relatively small areas. These include inkjet printing [13] and electron-beam lithography [47], as well as the scanning-probe technologies such as dip-pen nanolithography (via electrostatic or electrochemical deposition) [48-50], selective damaging of a surface via scanning tunnelling microscopy [51], nano-thermal lithography [52, 53] and scanning near-field optical lithography [35, 54-56].

Each technique has particular strengths, which may be in terms of flexibility, resolution, or the amount of damage inflicted on the active polymer. For a recent comparative review see Nie and Kumacheva, 2008 [57].

Of the approaches above, scanning-probe techniques offer a variety of flexible methods for creating high-resolution arbitrary patterns without the need for expensive photo masks, and for prototyping designs. The development of massively parallel tip-arrays also offers the possibility that scanning probes could be used directly for manufacturing small area devices with high throughput [58, 59]. Similar considerations on throughput and scale apply in respect of the impressively high scan speed (100 frames per second at 20x20 µm) obtained by the Miles group at Bristol, who have shown the possibility of video-rate scanning for a number of scanning-probe techniques, including near-field optical microscopy [60]. Attempts to pattern conjugated polymers on submicron scales using a scanning probe often rely on selectively damaging exposed areas of the polymer. However, scanning near-field optical lithography (SNOL), and more recently scanning thermal lithography [52], have been shown to provide versatile direct-write, non-destructive methods for patterning materials on the nano-scale. This thesis is primarily concerned with near-field optical lithography of conjugated polymers, which I will examine in more detail in sections 4. Section 5 will detail the use of nano-thermal lithography in the same role.

2. Near-field microscopy and lithography: Theory

Conventional microscopy and photolithography involve illumination of a sample through a lens or pre-made shadow mask, either to interact with the active material or pattern a photo-resist. The specific photo-sensitive materials used in this investigation will be discussed in section 4.

The physics of both microscopy and lithography are essentially identical, in that controlling patterns of light over small areas is required. Any limit on the resolving power of a microscope system can, by reversing the beam path, equally be thought of as a limit on the achievable resolution of features when the system is used as a lithographic tool. As such, to avoid repetition, all references in this section to microscopy and microscopic resolution will be assumed to apply equally to (photo) lithography and lithographic resolution. Specific experimental factors affecting the achievable resolution of near-field photo lithography will be discussed in more detail in section 4.

2.1. Fresnel-Kirchhoff integral

Optical microscopy is inherently a far-field method, in that the light used is assumed to consist of propagating plane waves. The resolution limit of these techniques is therefore limited by the extent to which these waves can be focussed, which will depend on the extent to which light is diffracted by the collection optics. This may be calculated by considering the propagation of an optical field emanating from a general aperture**.** The electric field amplitude *E* at position **P**(x,y,z) for a general aperture function *A*, where *A* is assumed to lie in the z=0 plane and represent the field amplitude in that plane, is given by using the Huygens principle that every point on a wave-front is itself a source of spherical waves. By considering integrating over these, the Fresnel-Kirchhoff integral is obtained:

$$E(x,y,z)=-\frac{i}{\lambda}\iint A(x',y',0)\frac{e^{ikr}}{r}\cos\theta dx'dy \tag{2.1}$$

Where $r^2 = |\mathbf{r}|^2 = (x-x')^2 + (y-y')^2 + z$, λ is the wavelength of the light passing through the aperture, $k = \frac{2\pi}{\lambda}$ and θ is the angle between r and the normal to the aperture plane, such that $\cos\theta = \frac{\mathbf{r}.\hat{\mathbf{z}}}{|\mathbf{r}|}$.

A schematic of the assumed aperture arrangement is shown in Figure 2.1. For most geometries, the resulting field pattern must be calculated numerically.

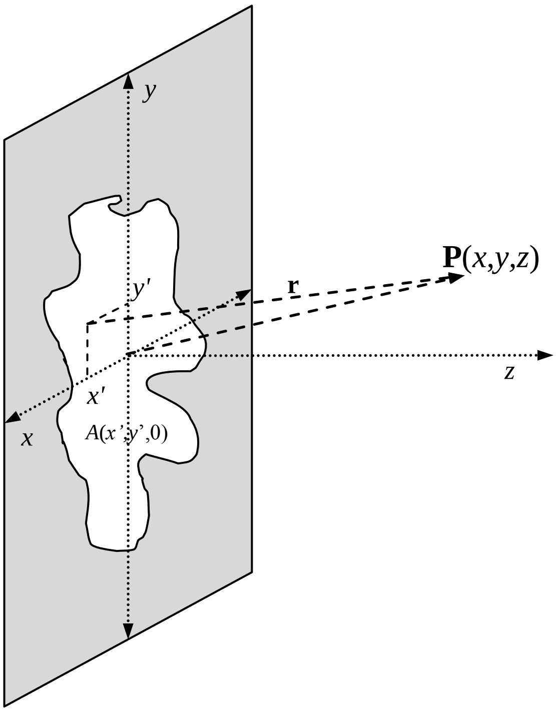

Figure 2.1: Schematic of an aperture *A* indicating the principle axes and the point **P** at which the field is to be calculated.

2.2. The Fresnel approximation

The main difficulty in solving the integral above is the convenient expression of *r*. However, if *z* is much greater than ρ, where ρ is given by:

(2.2) $$\rho^2 = (x-x')^2 + (y-y')^2$$

Substituting into the expression for *r* gives:

(2.3) $$r = z\sqrt{\left(1+\frac{\rho^2}{z^2}\right)}$$

Expanding binomially yields:

$$r = z\left[1+\frac{\rho^2}{2z^2}-\frac{1}{8}\left(\frac{\rho^2}{z^2}\right)^2+O\left(\frac{\rho}{z}\right)^6\right] \tag{2.4}$$

$$r = z+\frac{\rho^2}{2z}-\frac{\rho^4}{8z^3}+\ldots$$

Given that $z >> \rho$ over the whole aperture, this simplifies to:

$$r \approx z+\frac{(x-x')^2+(y-y')^2}{2z},\ \cos\theta \approx 1 \tag{2.5}$$

and so:

$$E(x,y,z) = -\frac{ie^{ikz}}{\lambda z}\iint A(x',y',0)e^{\frac{ik}{2z}\left[(x-x')^2+(y-y')^2\right]}dx'dy' \tag{2.6}$$

This is the Fresnel integral, which describes the propagation of a spherical wave originating at the aperture and propagating along z, with modulation in x and y. However, this too is also only soluble in certain simple cases. One further approximation is to assume that distance both from the aperture to the image plane and from the light source to the aperture are sufficiently large that curvature of the wave-fronts can be neglected (the light is parallel). This is equivalent to requiring that $x'^2+y'^2 << \frac{z}{k}$ over the whole aperture. More usually this is written $z >> \frac{a^2}{\lambda}$, where a is the maxiumum extent of the aperture. In this approximation, the Fresnel integral may be simplified further such that it reduces to the Fraunhofer form:

$$E(x,y,z) = -\frac{ie^{ikz}e^{\frac{ik}{2z}(x^2+y^2)}}{\lambda z}\iint A(x',y',0)e^{-\frac{ik}{z}(x'x+y'y)}dx'dy' \tag{2.7}$$

2.3. Fraunhofer diffraction

Providing the preconditions are met (parallel illumination, aperture and image plane far apart) this is simply a scaled two-dimensional Fourier transform of the aperture function, which may be calculated analytically for regular geometries, and using an efficient numerical method such as FFT for arbitrary aperture shapes. In particular, this regime applies to the situation of a collimated laser beam focussed through a lens or, reversing the beam path, light collected from a sample through a microscope objective.

To establish the resolution limit of such a system, I follow the considerations of Rayleigh [61] and assume a circular aperture of radius a at sufficient distance from the sample that the Fraunhofer approximation is valid. The angular diffraction pattern formed by the aperture will be radially symmetric and is given by its Fourier transform:

$$I(\theta) = I_0\left(\frac{2J_1(ka\sin\theta)}{ka\sin\theta}\right)^2 \tag{2.8}$$

Where θ is the observation angle (measured from the central axis of the system), I_0 is the intensity at $\theta = 0$ and J_1 is the Bessel function of the first kind of order one. This function has its first minimum at $ka\sin\theta = 3.8317$. Assuming that two point sources may be resolved, or two point objects defined, if the maximum of one coincides with the first minimum of the other (the Rayleigh criterion) then:

$$\sin\theta = 1.22\frac{\lambda}{d} \tag{2.9}$$

where $d = 2a$. Taking other resolving criteria, such as the Houston or Sparrow approach, leads to slightly different limits.

For a microscope objective with focal length f operating in a material with refractive index n, the minimum resolution $\Delta x \approx f\sin\theta$ is given by:

$$\Delta x = \frac{1.22 f\lambda}{nd} = \frac{1.22\lambda}{2n\tan\phi} \tag{2.10}$$

where ϕ is the angular aperture of the lens. Operating in air, with a high quality oil-immersion objective (numerical aperture 1.25, $n = 1.6$, $\phi = 50°$), an ultimate resolution limit of around 0.3-0.4λ is predicted from this criterion, with aberrations in the lens neglected. I have also assumed here that for the purpose of establishing resolution, obtaining a monochrome image is acceptable. For many high-resolution microscopy applications where specific spectroscopic information is sought, for instance in fluorescence microscopy, this is entirely appropriate.

In practice, contributions to the image from signals out of the focal plane of the lens (in addition to any other noise sources) reduce the available contrast, and therefore resolution, so that a typical far-field microscope will achieve a somewhat lower resolving power, typically no better than λ/2. One commonly used method to improve the performance of far-field microscopy is to focus both illuminating and collecting lenses at the same point, and spatially filter the collected light so that only components originating from the focus reach the detector – a so-called confocal arrangement, shown in Figure 2.2. The increased contrast this provides allows higher resolution to be achieved (< λ/2) at the expense of higher collection times due to the reduction in available light. In addition, the focal spot must be scanned over the object, both laterally and vertically, to build an image of the object. Confocal microscopes such as these are typically used to conduct high-resolution fluorescence microscopy, where monochromatic illumination and collection are appropriate.

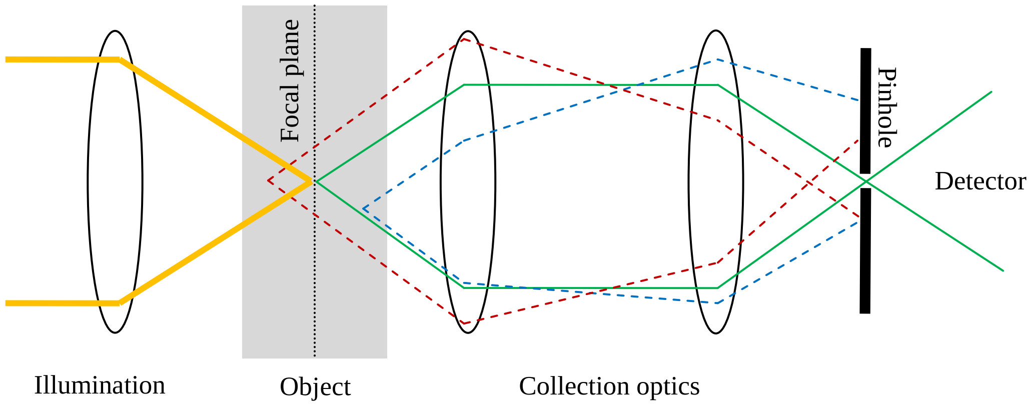

Figure 2.2: Schematic of a transmission-mode confocal microscopy arrangement. Out-of-focus beams are removed using a spatial filter (pinhole). For optimal resolution, the pinhole must be approximately the same diameter as the first minimum of the Airy disc associated with the collection optics.

In general, it is sufficient to note that for reasonable assumptions, a resolution limit of around λ/2 exists for far-field systems. Systems which operate close to this limit are said to be “diffraction limited”. For the lowest wavelength visible light (≈400 nm) a practical resolution limit of around 200 nm is typically observed.

2.4. Breaking the diffraction limit

To understand how to circumvent the limit described above, I return to the original expression for the pattern of light originating from an aperture or source. Instead of considering spherical waves, the local electric field strength U at the light source may instead be modelled, as a function of position, **R** and time, *t*, as a sum of three-dimensional plane waves, such that:

(2.11) $$U(\mathbf{R},t)=\sum_{\mathrm{all}\,\mathbf{K}} a_k e^{i(\mathbf{K}.\mathbf{R}-\omega t)}$$

Where **K** is the three-dimensional wave vector of each plane-wave component, a_k its magnitude and $\mathbf{K}=(k_x,k_y,k_z)$. In general, these components represent waves propagating along **K**. The *x* and *y* axes are taken for convenience to be in the plane of the light source, and the *z* axis to be in the direction of the object.

For monochromatic light of wavelength λ:

(2.12) $$\begin{gathered}|\mathbf{K}|^2=\left(\frac{2\pi}{\lambda}\right)^2=k_x^2+k_y^2+k_z^2\\ \Rightarrow\left(\frac{2\pi}{\lambda}\right)^2-\left(k_x^2+k_y^2\right)=k_z^2\end{gathered}$$

Therefore, if:

(2.13) $$k_x^2+k_y^2>\left(\frac{2\pi}{\lambda}\right)^2$$

then k_z is imaginary. For $k_{x,y,z}$ combinations where this is true, propagating plane waves are no longer described. Instead, in general it is found that:

(2.14) $$U(\mathbf{R},t)=\sum a_k e^{-|k_z|r_z} e^{i(k_x r_x+k_y r_y-\omega t)}$$

This describes a wave decaying exponentially in the z direction, over a length scale inversely dependent on the size of k_z. This is equivalent to saying that spatial components of the light source which vary laterally on a scale smaller than the wavelength of the light emitted will quickly decay away and be lost. This also predicts that the smallest intensity variations observable in the far-field will be of order λ/2, in agreement with the Rayleigh criterion. If short-wavelength spatial components of the light source are lost, the illumination across the sample can no longer be varied on short length scales. Equally, short-wavelength variations in the optical field originating from the sample will quickly be lost as they propagate through the optics.

Several solutions exist to the problem of how to increase this resolution. The first and most obvious is to reduce the wavelength of the illumination system. This can be done using particles with inherently low wavelengths – for example x-rays, γ-rays, electrons, neutrons or heavy ions. However, it is often the case that the window of responsiveness for the material being patterned/observed is fixed to a small region of the electromagnetic spectrum, removing this choice. For example, the rich photochemistry of conjugated polymers is typically accessed with visible or near-UV light. Another option mentioned previously is to immerse the system in a high-index material – for instance an oil – to reduce the effective wavelength of the incident light while retaining the energy per photon, but this can risk contaminating the sample, especially where the material is intended for use in an electronic device. Other possible solutions are to propagate the evanescent waves through a negative refractive index superlens [62], which shows considerable promise, or to entangle the incident photons, which has been predicted to allow them to act as a single photon with half the original wavelength [63]. However, the difficulty in obtaining two- or three-photon entangled light sources currently precludes widespread use of this phenomenon.

A direct method for retaining the high spatial-frequency features of a light source is to bring that source close to the sample being patterned/imaged, such that the evanescent components have not decayed by the time they reach the sample - moving from the far-field regime to the near-field regime. To estimate how close this needs to be, consider the following example. Using parameters applicable to those introduced in later sections, an incident wavelength λ of 325 nm and a required spatial modulation of the field of 50 nm in both the x and y directions are assumed. Combining (2.12) with (2.14), and noting that the inequality (2.13) is clearly satisfied, the field strength of this particular evanescent field component in air decays in amplitude by 50% by approximately 5 nm from the light source. This introduces two constraints if this near-field is to be utilised – one is the requirement that the source be held extremely close to the surface of the sample, and the other is the fact that optical focussing is clearly not possible in such a confined space. I have also so far ignored the fact that propagating, non-evanescent, components of the field still exist, and even close to the source these will dominate. To remove these problems, a pure near-field (i.e. purely evanescent) light source is needed.

2.5. The near-field microscope

The problem of how to produce a near-field light source was addressed by Synge in 1928 [64], and later, independently, by O'Keefe in 1956 [65]. Synge originally envisaged using the scattered light from a particle illuminated via total internal reflection as a near-field source. This was at first considered experimentally intractable, though it was later demonstrated both for fixed and optically trapped particles [66, 67], and today forms the basis of the scanning-tunnelling optical microscopy (STOM) technique, whereby a sharp pointed probe is used to locally frustrate the evanescent field generated within a sample through total internal reflection [68]. Synge went on to describe the alternative method of utilising a sub-wavelength aperture, which would block propagating components while establishing the tightly confined evanescent field required in this arrangement. The aperture is held very close to the sample surface, and scanned over it point by point to build up an image. The size of the area illuminated for such a system depends primarily on the size of the aperture, rather than on the wavelength of the incident light. The technical challenges associated with realising such a scanning near-field optical microscope are considerable, and were not overcome for nearly half a century. The first scanning near-field infrared microscope was demonstrated by Ash and Nicholls at UCL in 1972, achieving $\lambda/60$ resolving power with 3cm radiation [69]. True near-field optical microscopy, using apertured optical-fibre probes, took another 12 years to realise and was first demonstrated independently by Lewis [70] and Pohl [71] in the same year, describing the technique respectively as near-field scanning optical microscopy (NSOM) and near-field optical stethoscopy (NFOS), respectively – the latter in reference to similarities with the inherently sub-wavelength technique of medical stethoscopy. I shall use the convention, introduced some years later, of referring to the technique as scanning near-field optical microscopy (SNOM) to emphasise its place amongst the family of other scanning probe technologies.

An alternative arrangement leading to a similarly confined field may be achieved by illuminating a sharp conducting spike, typically using polarised light, first described in 1985 [72] and demonstrated in 1994 [73]. Local field enhancement at the tip generates a strongly confined high-intensity region which can be used as an excitation source for near-field microscopy. The resolution of such a system is limited primarily by the sharpness of the tip, since no aperture is used, but from the perspective of the investigations described below, the need for continuous far-field illumination is a disadvantage. The use of apertureless microscopes has a significant associated literature [74], but will not be considered further in this thesis.

2.6. Numerical methods

To understand the nature of the aperture-based near-field source described above, a description of the field profile close to the aperture is required. An exact analytical solution for the field present around a sub-wavelength aperture does not exist, however numerous numerical methods have been developed.

One approach is to use the Green's function method first proposed by Martin [75]. In this approach, the system is split into reference and scattering (background and sample) contributions with dielectric functions ε_r and ε_s respectively. In response to an arbitrary incident field, $E_0(\mathbf{r})$, the scattered field, $E(\mathbf{r})$ is then a solution of the vectorial wave equation:

$$-\nabla\times\nabla\times E(\mathbf{r})+k^2\varepsilon_r(\omega)E(\mathbf{r})+k^2\varepsilon_s(\mathbf{r},\omega)E(\mathbf{r})=\mathbf{0} \tag{2.15}$$

The associated Green's function, **G**, then obeys:

$$\left(-\nabla\times\nabla\times+k^2\varepsilon_r(\omega)+k^2\varepsilon_s(\mathbf{r},\omega)\right)\mathbf{G}=\mathbf{1} \tag{2.16}$$

The Greens function is calculated iteratively, and the scattered electric field can then be calculated from:

$$E(\mathbf{r})=\int d\mathbf{r}'\left[\partial(\underline{\mathbf{r}}-\mathbf{r}')-k^2\mathbf{G}(\mathbf{r},\mathbf{r}',\omega)\cdot\varepsilon_s(\mathbf{r}',\omega)\right]\cdot E_0(\mathbf{r}') \tag{2.17}$$

Since the method depends on solving for Green's tensor (or generalised field propagator) **G**, discretised over the scattering system, the complexity of the problem scales with the size and granularity of the system. The particular advantage of this technique is that once the generalised field propagator has been calculated for a particular scattering system, it may be re-used for differing illumination conditions at reduced computational cost. This has allowed the near-field around general objects in free space under different illumination conditions to be modelled, and in particular has been used to model the field near to an apertureless probe [76] . It has also been used to investigate the role of imaging mode (e.g. reflection or transmission – see section 6) and scanning mode (constant height, constant gap – see section 3) on the appearance of objects in SNOM images [77].

Another approach to solving near-field problems numerically is the finite difference time domain (FDTD) technique. This has been used to self-consistently solve Maxwell's equations at fixed points across an illuminated object by considering it as a collection of discrete cells with individually assigned complex refractive indices. Milner *et al* [78] have used this method to investigate the field enhancement generated by back-illumination (i.e. through the substrate) of a sharp conducting tip as a function of wavelength. This geometry is particularly important for tip-enhanced Raman spectroscopy and apertureless SNOM. In the case of apertured probes, the effect of the cladding thickness and excitation mode have been considered by Liu and He, and resulted in the theoretical design of a more intense field profile [79]. Furukawa and Kawata [80] have used FDTD to simulate line scans at constant-height and constant-distance across a back-illuminated feature with emission collected through the probe aperture, where multiple scattering events are considered, while Krug *et al* have used the method to suggest routes to the rational optimisation of apertureless probes [81].

One common property of the modelling approaches above is that the relative complexity of the calculation scales with the size, dimensionality and required spatial (and temporal) resolution of the system. This typically renders them suitable for small volumes, reduced dimensionality problems or problems where a single length-scale dominates. Numerical modelling of larger systems and far-field effects is typically extremely time-consuming. One particularly useful approximation which reduces the complexity of the problem of simulating the field was developed by Bethe [82] and Bouwkamp [83], and implemented by Stevenson *et al*. [84] in a computationally affordable manner.

They consider a sub-wavelength aperture, radius a, which is in the x–y plane. The incident field E_i propagates along the z-axis and is polarized along the x-axis. The origin of coordinates is taken as the centre of the aperture. The sample surface is a distance z_0 from the aperture. Figure 2.3 summarises this information.

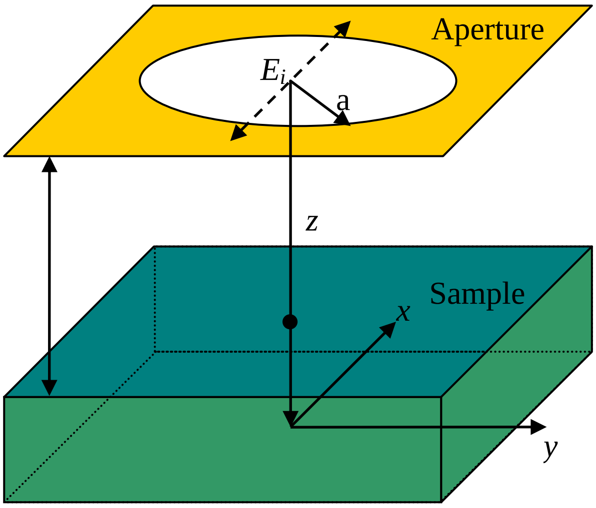

Figure 2.3: Schematic diagram of the sub-wavelength aperture and semiconductor sample, indicating the coordinate system used in the calculation. Reproduced from [84].

Making the assumptions that the aperture is defined in an infinite, perfectly conductive metal screen, which is thin compared to the aperture size, and that it is illuminated by monochromatic light with wave vector $k_0 = 2\pi/\lambda$, the electric field in the aperture, E_0, may be calculated. By further assuming that the aperture is illuminated normally and with polarisation aligned along $\theta = 0$, the expression for the electric field given by Bouwkamp simplifies to:

$$\mathrm{E}_{\rho} = -\frac{8ik_0}{3\pi}\frac{a^2 - \frac{1}{2}\rho^2}{\left(a^2 - \rho^2\right)^{1/2}}\cos(\theta)E \tag{2.18}$$

$$\mathrm{E}_{\theta} = -\frac{8ik_0}{3\pi}\left(a^2 - \rho^2\right)^{1/2}\sin(\theta)E_i \tag{2.19}$$

Where ρ and θ are cylindrical coordinates within the aperture, ρ < a, and E_i is the incident field strength. Transforming to Cartesian coordinates such that $\boldsymbol{\rho} = \rho(\cos\theta, \sin\theta)$, and considering the terms of components of the aperture field E_0 polarized along the x or y axes, gives:

$$\mathrm{E}_{0,\mathrm{x}}(x, y) = -\frac{4ik_0}{3\pi}\frac{2a^2 - x^2 - 2y^2}{\left(a^2 - x^2 - y^2\right)^{1/2}}E_i \tag{2.20}$$

$$\mathrm{E}_{0,\mathrm{y}}(x, y) = -\frac{4ik_0}{3\pi}\frac{xy}{\left(a^2 - x^2 - y^2\right)^{1/2}}E_i \tag{2.21}$$

where *x* and *y* subscripts refer to polarization directions. This result is correct, but differs very slightly from the results quoted both by Stevenson and Richards [84] and by van Labeke *et al* [85], the former missing a factor of two in the numerator of the *x*-polarised field and the latter introducing an extra factor of two into both denominators.

To simulate the propagation of the field away from the aperture, one approach due to van Labeke [85] is to calculate the two-dimensional Fourier transform of the field, allowing it to be expressed in terms of its spatial frequency components $\mathbf{k} = k(\cos\phi, \sin\phi) = (k_x, k_y)$.

(2.22)
$$\mathrm{E}_0(k) = \int_0^\infty \int_0^{2\pi} \mathrm{E}_0(\rho,\theta) e^{-i\mathbf{k.\rho}} \rho \,\mathrm{d}\rho\,\mathrm{d}\theta = \int_0^\infty \int_0^{2\pi} \mathrm{E}_0(\rho,\theta) e^{-ik\rho\cos(\theta-\phi)} \rho\,\mathrm{d}\rho\,\mathrm{d}\theta$$

By making the substitution $\psi = \theta - \phi$, and noting that the field is partially separable in ρ and θ, the integral may be rewritten as:

(2.23)
$$\mathrm{E}_0(k) = \int_0^\infty \mathrm{R}(\rho)\rho\,\mathrm{d}\rho \int_0^{2\pi} \Theta(\psi+\varphi) e^{-ik\rho\cos(\psi)}\,\mathrm{d}\psi$$

Taking the *x*- and *y*-polarised components to be independent, this may be split into:

(2.24)
$$E_{0,\mathrm{x}}(k) = -\frac{4ik_0}{3\pi}\left[\int_0^a \frac{2a^2\rho}{\left(a^2-\rho^2\right)^{1/2}}\,\mathrm{d}\rho \int_0^{2\pi} e^{-ik\rho\cos(\psi)}\,\mathrm{d}\psi - \int_0^a \frac{\rho^3}{\left(a^2-\rho^2\right)^{1/2}}\,\mathrm{d}\rho \int_0^{2\pi} 1+\sin^2(\psi+\phi) e^{-ik\rho\cos(\psi)}\,\mathrm{d}\psi\right]$$

(2.25)
$$E_{0,\mathrm{y}}(k) = -\frac{4ik_0}{3\pi}\left[\int_0^a \frac{\rho^3}{\left(a^2-\rho^2\right)^{1/2}}\,\mathrm{d}\rho \int_0^{2\pi} \sin(\psi+\phi)\cos(\psi+\phi) e^{-ik\rho\cos(\psi)}\,\mathrm{d}\psi\right]$$

By using the zeroth-order Bessel functions of the first kind:

(2.26)
$$J_0(z) = \frac{1}{2\pi}\int_0^{2\pi} e^{-iz\cos(\alpha)}\mathrm{d}\alpha$$

(2.27)
$$J_0{}'(z) = -\frac{i}{2\pi}\int_0^{2\pi} \cos(\alpha) e^{-iz\cos(\alpha)}\mathrm{d}\alpha$$

And noting both that:

(2.28)
$$\int_0^{2\pi} \sin(\psi)\cos(\psi) e^{-ik\rho\cos(\psi)}\,\mathrm{d}\psi = 0$$

and:

(2.29)
$$\int_0^{2\pi} \sin^2(\psi) e^{-ik\rho\cos(\psi)}\,\mathrm{d}\psi = -\frac{1}{ik\rho}\int_0^{2\pi} \cos(\psi) e^{-ik\rho\cos(\psi)}\,\mathrm{d}\psi = -\frac{2\pi J_0'(k\rho)}{k\rho}$$

By expanding those functions in $\psi + \phi$ and integrating over ψ it may be shown that:

(2.30)
$$\mathrm{E}_{0,\mathrm{x}}(k) = -\frac{4ik_0}{3\pi}\left[2a^2\int_0^a \frac{\rho}{\left(a^2-\rho^2\right)^{1/2}} 2\pi\,\mathrm{J}_0(k\rho)\mathrm{d}\rho - \left(1+\sin^2\phi\right)\int_0^a \frac{\rho^3}{\left(a^2-\rho^2\right)^{1/2}} 2\pi\,\mathrm{J}_0(k\rho)\mathrm{d}\rho + \left(\cos^2\phi - \sin^2\phi\right)\int_0^a \frac{\rho^3}{\left(a^2-\rho^2\right)^{1/2}} \frac{2\pi\,\mathrm{J}_0'(k\rho)}{\mathrm{k}\rho}\mathrm{d}\rho\right]$$

(2.31)
$$\mathrm{E}_{0,\mathrm{y}}(k) = -\frac{4ik_0}{3\pi}\left[\cos\phi\sin\phi\int_0^a \frac{\rho^3}{\left(a^2-\rho^2\right)^{1/2}} 2\pi\,\mathrm{J}_0(k\rho)\mathrm{d}\rho + \left(2\cos\phi\sin\phi\right)\int_0^a \frac{\rho^3}{\left(a^2-\rho^2\right)^{1/2}} \frac{2\pi\,\mathrm{J}_0'(k\rho)}{\mathrm{k}\rho}\mathrm{d}\rho\right]$$

Considering the three integral components separately:

(2.32)
$$I_1 = \int_0^a \frac{\rho}{\left(a^2-\rho^2\right)^{1/2}} J_0(k\rho)\mathrm{d}\rho$$

(2.33)
$$I_2 = \int_0^a \frac{\rho^3}{\left(a^2-\rho^2\right)^{1/2}} J_0(k\rho)\mathrm{d}\rho$$

(2.34)
$$I_3 = \int_0^a \frac{\rho^2}{\left(a^2-\rho^2\right)^{1/2}} \frac{J_0'(k\rho)}{k}\mathrm{d}\rho$$

(2.35)
$$\frac{dI_1}{dk} = \int_0^a \frac{\rho^2}{\left(a^2-\rho^2\right)^{1/2}} J_0'(k\rho)\mathrm{d}\rho = kI_3$$

These may be solved using their similarity to the zeroth-order Hankel transform:

(2.36)
$$\mathrm{H}_0(k, f(\rho)) = \int_0^\infty f(\rho) J_0(k\rho)\rho\,\mathrm{d}\rho$$

$$I_1 = \mathrm{H}_0\left(k, \frac{1}{\left(a^2-\rho^2\right)^{1/2}}\right) = \frac{\sin(ak)}{k} \tag{2.37}$$

$$I_3 = \frac{a\cos(ak)}{k^2} - \frac{\sin(ak)}{k^3} \tag{2.38}$$

$$I_2 = \mathrm{H}_0\left(k, \frac{\rho^2}{\left(a^2-\rho^2\right)^{1/2}}\right) = -\left[\frac{d^2}{dk^2} + \frac{1}{k}\frac{d}{dk}\right]\mathrm{H}_0\left(k, \frac{1}{\left(a^2-\rho^2\right)^{1/2}}\right) = -\frac{d^2 I_1}{dk^2} - \frac{1}{k}\frac{dI_1}{dk} = -\frac{d}{dk}kI_3 - I_3 \tag{2.39}$$

$$I_2 = \frac{a}{k^2}\cos(ak) + \left(\frac{a^2}{k} - \frac{1}{k^3}\right)\sin(ak) \tag{2.40}$$

Returning to the original field expressions:

$$\mathrm{E}_{0,\mathrm{x}}(k) = -\frac{8ik_0}{3}\left[2a^2 I_1 - \left(1+\sin^2\phi\right)I_2 + \left(\cos^2\phi - \sin^2\phi\right)I_3\right] \tag{2.41}$$

$$\mathrm{E}_{0,\mathrm{y}}(k) = -\frac{8ik_0}{3}\left[\cos\phi\sin\phi\left(I_2 + 2I_3\right)\right]E_i \tag{2.42}$$

$$\mathrm{E}_{0,x}(k) = -\frac{8ik_0E_i}{3\pi}\left(\frac{1}{k^4}\right)\left[-3ak_y^2\cos(ak) + \frac{1}{k}\left(a^2k_x{}^4 + a^2k_x^2k_y^2 + 3k_y^2\right)\sin(ak)\right] \tag{2.43}$$

$$\mathrm{E}_{0,\mathrm{y}}(k) = -\frac{8ik_0E_i}{3\pi}\left(\frac{k_xk_y}{k^4}\right)\left[3a\cos(ak) + \frac{1}{k}\left(a^2k^2 - 3\right)\sin(ak)\right] \tag{2.44}$$

To construct the field away from the aperture, the three-dimensional vectors **R** = (x,y,z) = ($\boldsymbol{\rho}$,z) and the wave vector **K** = (k_x,k_y,k_z) = (***k*,** k_z) must be introduced, noting also that where it is used as a scalar, $k = |\boldsymbol{k}|$.

The electric field strength at position ***R*** in vacuum, $E_v(\boldsymbol{R})$, is given by the integral over all ***K*** vectors, such that:

$$E_v(\boldsymbol{R}) = -\frac{1}{4\pi^2}\iint E_v(k,z)e^{(ik\cdot r)}dk \tag{2.45}$$

$$E_v(k,z) = E_0(k)e^{(iz\kappa_v(k))} \tag{2.46}$$

where $\kappa_v(k) = \sqrt{k_0^2 - k^2}$ and leads to both evanescent and propagating waves, as encountered previously. Maintaining the same notation, the electric field E_s in the sample at the sample/vacuum interface ($z = z_0$) is related to E_v by:

$$[E_s(k, z_0)]_x = \left(\alpha + \frac{k_x^2 \beta}{k^2}\right)[E_v(k, z_0)]_x + \frac{k_x k_y}{k^2}\beta[E_v(k, z_0)]_y \tag{2.47}$$

$$[E_s(k, z_0)]_y = \left(\alpha + \frac{k_y^2 \beta}{k^2}\right)[E_v(k, z_0)]_y + \frac{k_x k_y}{k^2}\beta[E_v(k, z_0)]_x \tag{2.48}$$

where:

$$\alpha = \frac{2\kappa_v}{\kappa_v + \kappa_s} \tag{2.49}$$

$$\beta = \frac{2k^2(n^2 - 1)}{(\kappa_v + \kappa_s)(n^2\kappa_v + \kappa_s)} \tag{2.50}$$

$$\kappa_s(k) = \sqrt{n^2 k_0^2 - k^2} \tag{2.51}$$

and n is the refractive index of the sample.

Finally, the field within the sample, at $z > z_0$, is given, as in equation (2.45), by the Fourier transform of the k-space field representation:

$$E_s(\boldsymbol{R}) = -\frac{1}{4\pi^2}\iint E_s(k, z)e^{(ik\cdot r)}d \tag{2.52}$$

$$E_s(k, z) = E_s(k, z_0)e^{[i(z-z_0)\kappa_s(k)]} \tag{2.53}$$

An example of the field profile produced using this technique is shown in Figure 2.4 assuming aperture diameter 50nm, sample thickness 20 nm and film refractive index 1.73 + 0.067i. The fields shown here and elsewhere are calculated using a MATLAB code to implement the method described here and written by Dr Oliver Fenwick at UCL.

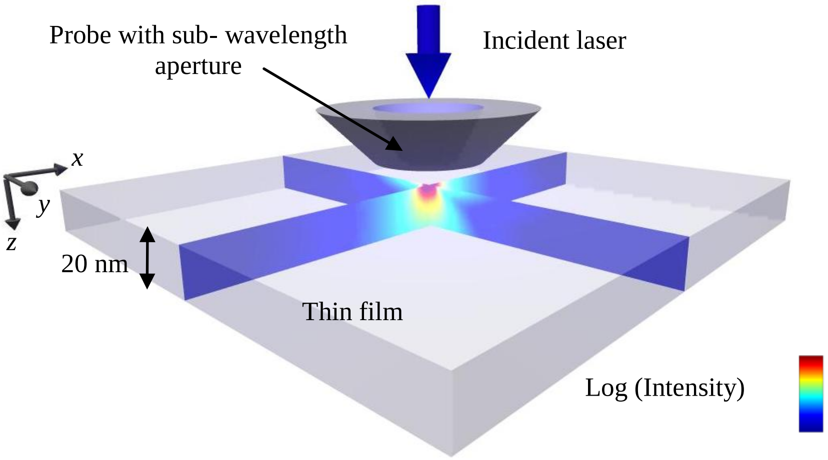

Figure 2.4: three-dimensional representation of the optical field strength in a thin film placed below the tip of an apertured SNOL probe. Incident laser polarisation assumed to be parallel to the *x*-axis.

3. Instrumentation

3.1. The Scanning Near-Field System

The scanning probe system used in the near-field investigations described below is shown schematically in Figure 3.1. The tip assembly is positioned laterally and brought close to the sample using both coarse stepper motors and a three-way micrometer translation stage, with the approach observed using the CCDs shown in Figure 3.1. The final approach is controlled electronically, described below.

The scanning head, expanded in Figure 3.2, consists of a piezoelectric quartz tuning fork mounted on a piezoelectric bimorph, to which an optical fibre near-field probe is glued, described in section 3.2. The bimorph is driven close to the fundamental acoustic resonant frequency of the combined tuning fork/probe system using a lock-in amplifier. As the fork oscillates, cycles of strain and relaxation generate an alternating response voltage between the fork tines, which is detected via electrodes attached to the fork and amplified close to the tip assembly to reduce the effects of transmission-line noise, before being fed back to the control electronics. The amplitude of the response signal depends on the strength of the acoustic oscillations of the fork. As the tip moves close to the sample, short-range lateral shearing interactions between the fibre and sample surface dampen these oscillations. This causes a drop in the response signal, the size of which is related to the strength of damping. Light contact (probe just interacting with surface) typically leads to a 0.1-1% drop in signal and hard contact (probe crushed into sample) leads to a 10-20% drop in signal compared to the free-space amplitude, with further variation depending on noise and cross-talk between the drive and response and on the resonant profile of the system, which can be controlled using a resonance controller unit (see section 3.3).

In this configuration, two modes of operation are possible – constant height and constant gap. For constant height mode, the probe is scanned close to the sample with no modulation in the vertical (*z*) direction, and changes in the feedback signal are recorded as a proxy for local topography. For constant gap mode, the feedback signal is used to maintain a constant distance between the probe and sample by modulating the vertical position of one or both of them. This mode is necessarily slower, but since a direct measure of local topography is typically required and, most importantly, a convolution between sample topography and illumination intensity must be avoided, it is the preferred mode of operation.

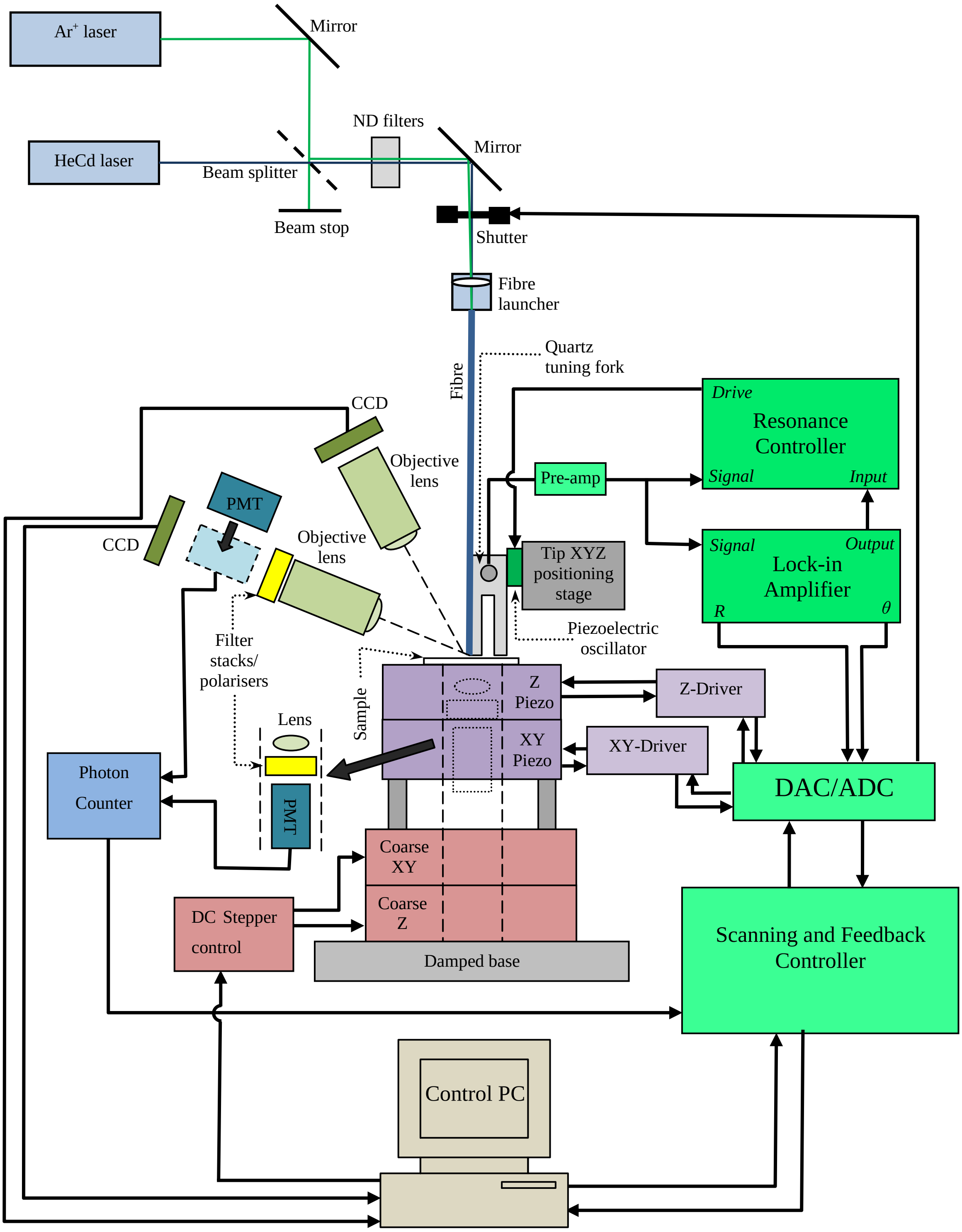

Figure 3.1: Schematic of the scanning near-field probe system used in the investigations described in sections 4 and 6. Solid arrows indicate signal direction.

To implement this mode, the response signal from the fork tines is fed back to the driving lock-in, which calculates the response amplitude and phase shift at the drive frequency. These data are recorded by a semi-automated ADC/DAC/control system – all contained within a programmable ADWin Gold unit – and compared to a pre-chosen set-point, i.e. the damping level required for the particular experiment being conducted. The difference between the measured and required signals is used to calculate an offset voltage *dV*, which is applied to the piezoelectric *z*-translation stage on which the sample rests. The offset voltage controls the relative vertical position of tip and sample, and depends on the signal offset Δ through the relationship given by equation (3.1) below

$$dV = G_p \Delta + \frac{G_I}{T_i} \int \Delta dt + G_d T_d \frac{d\Delta}{dt} \tag{3.1}$$

Where G_p is the proportional gain, G_i the integral gain, G_d the differential gain and $T_{i/d}$ are the integration and differentiation times, respectively. By suitable choice of constants, and iteratively applying this feedback relationship, Δ can be minimised and the tip held at a constant distance from the sample. The feedback loop is activated when the probe is within the travel distance of the *z*-translation stage (maximum 20 µm), and automatically brings the tip into close contact with the sample. Shear-force feedback using a quartz tuning fork was first described by Karrai and Grober [86], and is functionally analogous to tapping-mode Atomic Force Microscopy (AFM), in that short-range damping interactions rather than constant physical contact are used to maintain close proximity between tip and sample. Previous work has indicated that by this method, the tip-sample distance for this system is kept within approximately 5-10 nm for a 1-5% damped signal [87].

The feedback calculations are controlled indirectly using a software interface to the ADWin unit which allows the gains and set-point to be adjusted in real-time, and approach/retraction initiated. Indirect control is necessary to prevent software crashes, processing lag and other errors arising from the control PC interfering with the maintenance of feedback. Loss of feedback can very quickly lead to hard contact between the tip and sample, destroying the delicate aperture of the probe. Excessive noise can also interfere with the feedback loop, reducing the ability of the system to respond to changes in sample topography. To reduce vibrational noise, the entire system is isolated on a heavy granite base suspended by rubber springs above an air-damped optical table. Electronic noise is reduced by metallic shielding around the probe pre-amplifier and cabling, and through the use of high quality copper-guarded parallel bundles of BNC cables to pass signals to and from the lock-in/ADC and probe.

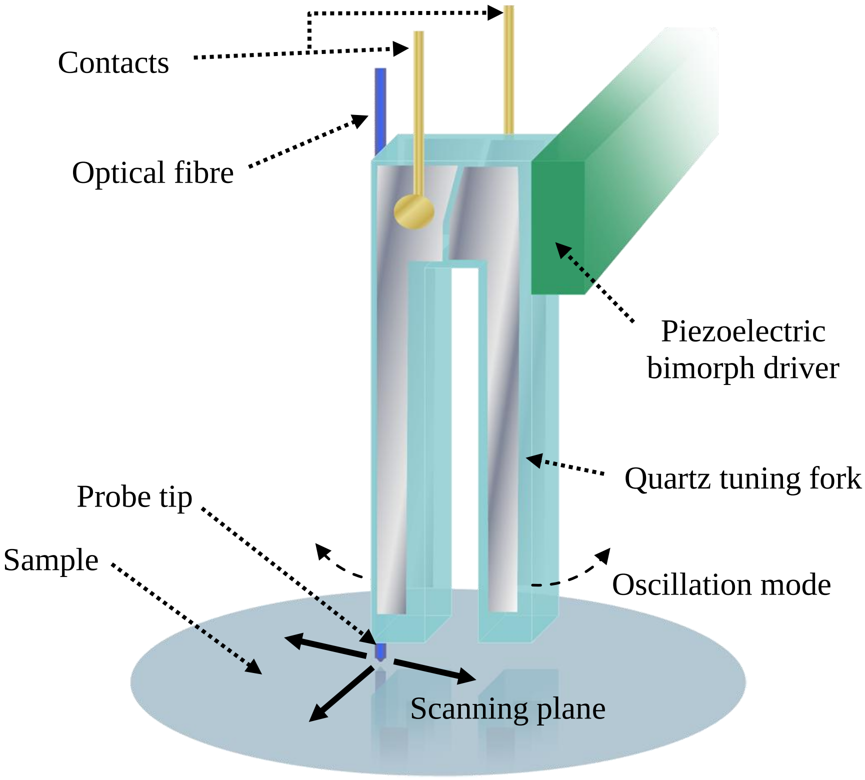

Figure 3.2: Schematic of the scanning probe tip assembly. Resonant oscillations in the piezoelectric quartz tuning fork are detected as an oscillating voltage between the two tines. The amplitude of this oscillation is used to calculate the strength of interaction between the probe tip and the sample.

The tip is scanned over the sample using the ADWin DAC to control an *x*-*y* piezoelectric translation stage (maximum travel 200 µm). While scanning, the three-dimensional position of the sample is monitored using capacitative sensors in the piezoelectric stages. Provided close contact is maintained, these provide a topological profile of the sample being scanned – in other words, the probe acts as a shear-force AFM.

The probe aperture is illuminated using lines from either a Helium-Cadmium or Argon Ion laser launched into the probe fibre through a neutral-density (ND) filter wheel and an electronically controlled mechanical iris shutter with a nominal response time of 10 ms. The latter allows arbitrary illumination sequences to be applied as the probe scans over the sample. Light transmitted through the sample (both incident and emitted) is collected though a lens and filter stack by a photomultiplier tube (PMT) mounted inside the column of scanning stages. Light reflected from the sample is similarly collected using a PMT which can be inserted into the approach-optics beam path. An electronic discriminator is used to count the collected photons, with background light minimised by operating the system within a sealed box inside a darkened laser laboratory. The number of photons collected at each point in the scan is recorded simultaneously with the topographic signal by the ADWin controller.

3.2. Near-field probes

In the work presented here, the apertures are created at the apex of sharpened, gold-coated optical fibres purchased from Jasco Ltd. of Japan, and have typical aperture diameters of 30-80 nm. The probes have a double-tapered structure which has been shown to increase throughput as compared to single-taper (needle-like) probes. They are shown in Figure 3.3. It should be noted that the light-path of such a system can easily be reversed, allowing light *from* a sub-wavelength area of the sample to be collected via the aperture, although this alternative set-up will not be considered further in this thesis.

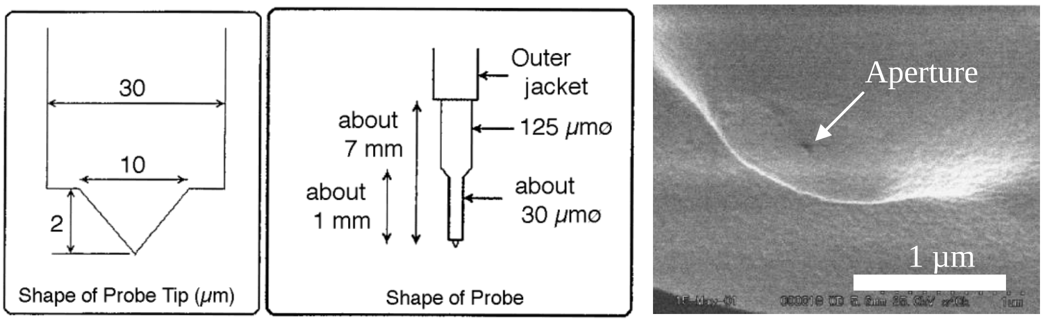

Figure 3.3: (left) Schematic of a double-tapered Jasco SNOL probe (right) SEM image of the apex of such a probe, showing the aperture, provided by Jasco. Typical throughputs are of order 10^{-3}-10^{-4} at optical wavelengths.

While it is clear that these probes are not infinite in extent, or infinitely conducting, and have coatings of comparable thickness to the aperture size, it is expected that the Bethe-Bouwkamp model will offer a reasonable approximation to the correct field close to the aperture. The field calculated using the Bethe-Bouwkamp model described in section 2.6 is therefore used to estimate that which exists close to a real near-field aperture. The choice of wavelength of the light transmitted and/or collected depends on the intended application, be it photoluminescence imaging as described in section 6 or lithographic patterning detailed in section 4. Figure 2.4 shows the field shape expected at a probe tip with 50 nm aperture for illumination at 325 nm – suitable for several lithographic patterning routes.

3.3. Improving resonance

One significant limitation affecting the achievable resolution of the near-field system described in section 3.1 is the quality of the contact between the probe and the sample to be patterned. As has been outlined in section 2.6, the field around the probe tip has an extremely high gradient, such that deviations in the height of the probe above the sample will lead directly to large variations in the illumination intensity and loss of control of the illumination profile. Maintaining a constant probe-sample distance is therefore critical to the performance of the system, and in the setup described in section 3.1, two factors fundamentally limit the feedback response.

The first is noise, both electrical interference picked up in the cabling and potentially amplified by the probe pre-amplifier, and ambient vibrational noise entering through the superstructure. Suitable equipment choices (low-noise amplifiers, highly-shielded cables, inertial and pneumatic damping), and elimination of ground loops mitigate this influence as far as possible. The second factor relates to the sensitivity of the feedback system. The quartz tuning forks used for shear-force feedback exhibit extremely sharp (high Q) resonance peaks, even with the fibre-optic probe glued to one tine. Bringing the probe close to the sample shifts and damps this peak, as described. The high Q factor of the resonance means that the system is extremely sensitive to this damping effect, meaning that very high topographic resolution is possible.

However, some additional factors must be considered when assessing the ability of the system to maintain constant close contact. Firstly, close to resonance, the system is inherently unstable and the peak can move and change shape over time - due to heating effects, wear on the probe, exposure to dust or draughts, for example. Using a sharp peak has the consequence of amplifying these slight changes in the resonance profile, which makes maintaining contact with the sample for long periods very difficult. In effect, the feedback signal can become dominated by changes in the resonant envelope, rather than contact with the sample. Secondly, due to the configuration of the SNOM hardware, the resonance signal is sampled at a rate of approximately 512Hz. As a result, there is a tendency for the probe control to lag a few milliseconds behind the feedback signal. For a sharp resonance, where changes in signal are large and rapid, this leads to heavy ‘bouncing’ contact, where the control constantly overcompensates for changes in the feedback signal. The system is therefore limited not by the sensitivity of the probe, but by the ability of the control system to respond. This is particularly true if there is any remnant noise in the system. Because of these effects, it is desirable to damp the resonance peak, making it broader so that small changes in resonance characteristics do not mask the damping of the resonance by contact with the sample. By doing this, some of the sensitivity to topography is sacrificed, but provided this is below the sensitivity threshold of the rest of the system, in practice it makes little difference.

The resonance controller shown in Figure 3.1, an ActivResonance Controller unit (ARC), provides a way to alter the apparent Q factor of any given driven oscillator. It works by adding a component of the response signal from the oscillator into the drive signal for that oscillator. Both the phase (relative to the drive signal) and amplitude of this component can be modified by the controller. The resulting drive signal close to the resonant frequency can therefore be boosted, by adding the two signals in phase, or damped, by adding them out of phase. The Q factor of the resonance peak may therefore be enhanced or reduced by a suitable choice of feedback conditions. A schematic of this system is shown in Figure 3.4. Enhancement of the resonance is appropriate to inherently damped probe systems, such as those immersed in fluid. In general, I wish to damp the resonance for the reasons described above.

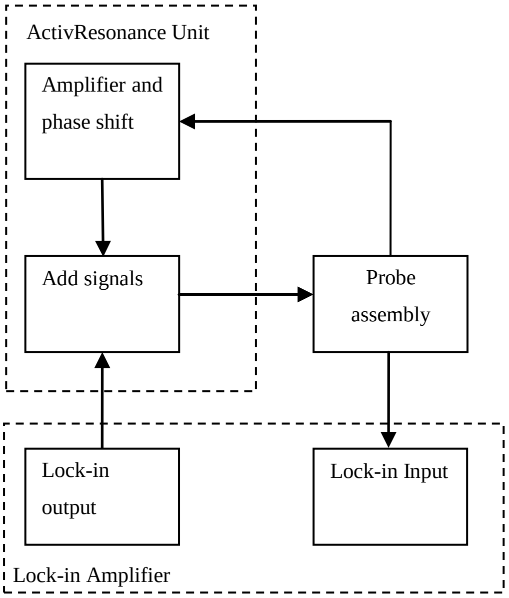

Figure 3.4: Schematic of the operating principle of the ARC unit. The ARC acts as a filter between the lock-in and probe assembly, and is invisible to the control hardware.

Figure 3.5 presents a set of data from a typical Jasco probe (30 nm aperture) showing the feedback signal both before and after the probe is attached, and after the ARC has been used to damp the resonance. The result of this modification is a smoothing of the feedback response, allowing vertical topographic resolution of around 1 nm to be achieved during scanning, and a decoupling of optical signal from feedback quality. All images and lithographic scans presented in later sections using the near-field system utilised the ARC unit, except for the images shown in Figure 6.14 and Figure 6.15.

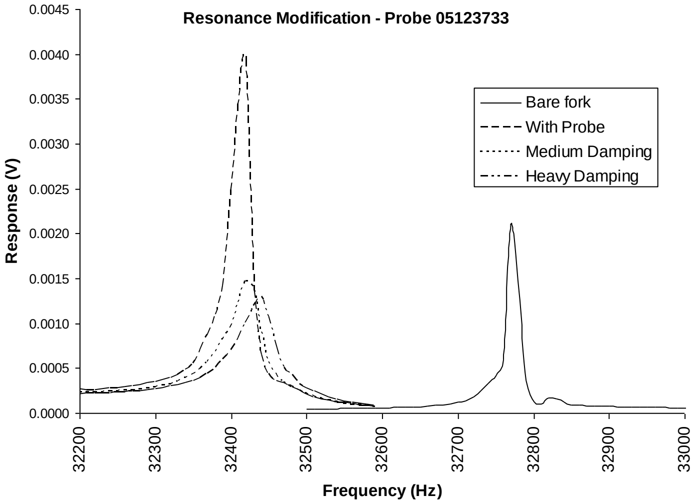

Figure 3.5: Frequency response of a typical probe/fork combination before and after attachment of the probe, and with and without electronic damping from the ARC.

4. Scanning near-field photolithography

Since the first demonstration of near-field photolithography by Betzig [88], who reported in 1992 the patterning a 50 nm photoresist film to 100 nm resolution, a number of approaches to near-field patterning have been described. The most popular uses Betzig's approach, using a scanning near-field probe to selectively pattern a thin precursor film by direct chemical modification, typically followed by an etching or development step. This has been shown to work for a large number of materials systems using apertured near-field probes. The greatest numbers of examples arise from utilising commercial photoresists [89-91], with the aim of generating structures in high resolution etched patterns. Examples of more functional and exotic materials include the patterning of PPV to 160 nm resolution via a precursor route [54], the patterning of self-assembled monolayers (SAMs) to resolutions limited only by the aperture size (~50nm), which could in turn be transferred to the underlying substrate via wet etching [92]. Even higher resolutions (20nm) have been achieved in SAMs by utilising unintended field enhancement by polycrystalline gold-film substrates [55]. Apertureless probes have also been used for patterning a number of materials, the most relevant for the investigations below is the direct (development-less) lithography of azobenzene-functionalised poly(methyl-methacrylate) [93-95].

Beyond the film-based approach above, somewhat more unconventional techniques have been demonstrated, including the fabrication of luminescent Zinc nano-dots deposited through the photo-dissociation of precursor diethylzinc gas by two-photon absorption [96]. Two-photon absorption is particularly well suited for use with near-field systems, because the field intensity near to the aperture is expected to vary very rapidly, reducing the effective excitation volume and avoiding unintended far-field exposure. This has been exploited in a number of ways, using both apertureless probes with pulsed excitation to fabricate 70 nm features in the commercial resist SU-8 [97] and using pre-fabricated nano-antennas to significantly enhance a far-field excitation field to generate 30 nm features in the same material [98].

The limits of near-field patterning technologies are still being extended, with the development of new, integrated cantilever probes which offer the chance of greater customisation and parallel production. An example of a fully-integrated cantilever probe with a built-in Gallium-Nitride LED light source was recently demonstrated by Kingsley *et al* and used to demonstrate 35 nm lithography, again in a commercial photoresist [56]. A recent review of the various routes to near-field nanofabrication, including additional examples, is given by Tseng [99].

In the following sections, top-down near-field lithography using the SNOL system outlined in section 3 is used to pattern a variety of conjugated polymers and small molecules via a number of routes. The theoretical background to this technique is detailed in section 2, while the context of near-field lithography within the broader family of lithography methods is outlined in section 1.7.

4.1. Lithography of PPV

PPV is an optically and electronically active material, and one of the most widely studied conjugated polymers. Its derivatives have attracted considerable interest for incorporation into organic devices. Blends of poly(2-methoxy-5-[3’-7’-dimethyloctyloxy]-1,4-phenylenevinylene) (MDMO-PPV) and [6,6]-phenyl-C61 butyric acid methyl ester (PCBM) were used as the active layer in some of the first efficient (>2.5%) organic photovoltaics [30], while unsubstituted PPV was used to construct the first polymer LEDs [9]. The large refractive index of highly oriented PPV also makes it suitable as a photonic material [100]. Using a home-built SNOL system, it has previously been demonstrated that thin PPV films can be patterned to a predetermined and reproducible design with sub-micron resolution [35]. The aims of the investigations reported herein were to significantly improve the resolution obtainable with this system, increase the complexity of patterning, and to further the understanding of structure formation under a SNOL tip.

4.1.1. Methodology

PPV was prepared *in-situ* via a Wessling-type precursor process [101], using UV light to convert the soluble polyelectrolyte poly(*p*-xylene tetrahydrothiophenium chloride) (PXT) into insoluble conjugated PPV through a “leaving group” reaction and thermal annealing step. A detailed review of the precursor routes to PPV and the flexibility they allow in film properties was presented by Bradley in 1987 [102].

Thin films of PXT were prepared by spin casting a solution of 0.25% PXT by weight in water (Sigma Aldrich, #540765) onto fused silica substrates, chosen for their high UV transmission (15mm Spectrosil® B windows, UQG. "Spectrosil" and "fused silica" should be considered synonymous in the following sections). Film thickness was controlled by varying the spin speed from 2400-1200rpm (corresponding to 15-35 nm thickness, measured using a Dektak surface profilometer), over which range good quality pinhole-free films were obtainable.

The absorbance of an as-spun PXT thin solid film, measured using a HP 8453 UV-Vis spectrophotometer, shows a peak around 325 nm corresponding to an initiation of the leaving-group reaction – as shown in Figure 4.1. Site-selective excitation at this wavelength forms the basis of the following sections.

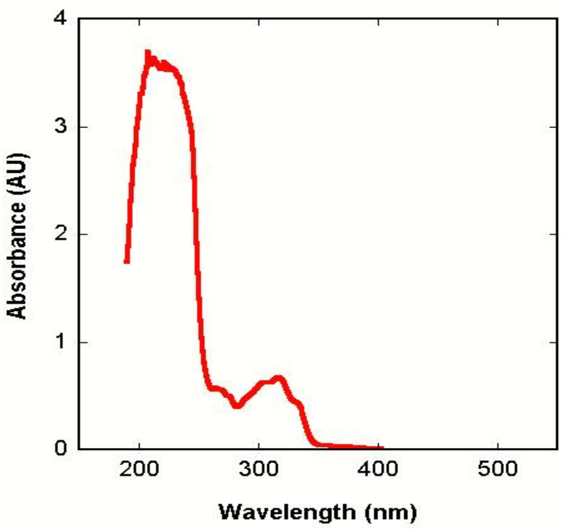

Figure 4.1: Absorbance profile of a PXT thin film spun onto fused quartz (Spectrosil). The large peak < 250nm is due to substrate absorption.

To create patterns, the SNOL was used under ambient conditions to selectively convert areas of the PXT films with light from a HeCd laser at 325 nm launched into the probe fibre. The electronic shutter placed between the laser and the fibre was used to allow arbitrary patterns to be defined as the probe moved over the sample. Removal of the leaving groups renders the PXT chain progressively less soluble. After sufficient exposure, this allows the unexposed PXT to be removed by rinsing in methanol for 20-30 seconds, leaving the desired patterns behind. Full conversion and solvent removal was achieved by baking under vacuum (< 10^{-3} mbar) at ~220ºC for two hours. This causes shrinkage of the observed features, addressed in section 4.1.4. A schematic of the reaction is shown in Figure 4.2. The effectiveness of this technique is heavily dependent on the response of the material being patterned to the light source illuminating it. One facet of the work on PPV done so far is to investigate the factors affecting the resolution of structures formed, particularly in relation to unintentional partial- or over- exposure of the PXT precursor.

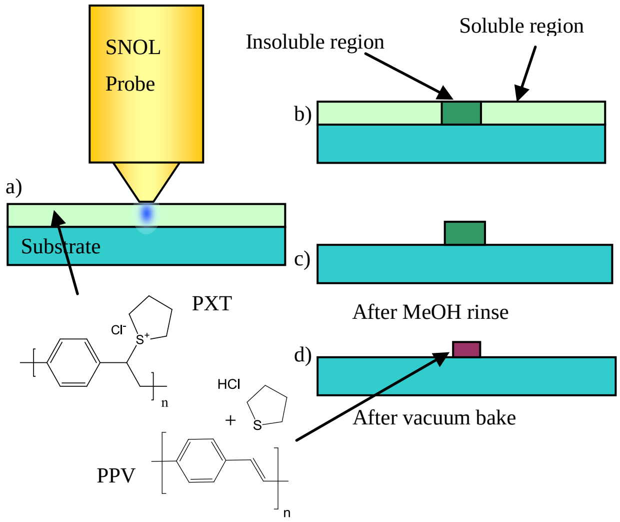

Figure 4.2: From a)-d), schematic of the process used to create isolated PPV structures using SNOL.

4.1.2. Minimum feature size

To optimise the achievable feature size, dot patterns were drawn in thin films of known thickness, with a varying UV dose controlled by adjusting exposure time and laser intensity. Figure 4.3 shows a set of such features drawn in a PXT thin film spin-cast to approximately 15 nm thickness. Exposure time per point increases from left to right (50-1000 ms), leading to a corresponding variation of feature widths from ~50-300 nm. It can be seen that a transition occurs from overexposed features at >500 ms, with semi-hollow cores (interpreted as due to breakdown and re-solubilisation of the PPV over long exposure times [103, 104], which is described more fully in section 4.1.5), to underexposed poorly attached or smear-like features at 50 ms. Optimal features are obtained at 100 ms exposure and are assumed to be close to ‘critical’, meaning that they are close to the smallest features that can be produced with acceptable compliance with the intended position. Figure 4.3 (middle-right) also shows a high resolution scan of the best resolved of these, displaying a minimum feature size of ~55 nm full-width at half-maximum (FWHM), which is only marginally larger than the nominal size of the aperture and the highest resolution structure produced by this system to date.

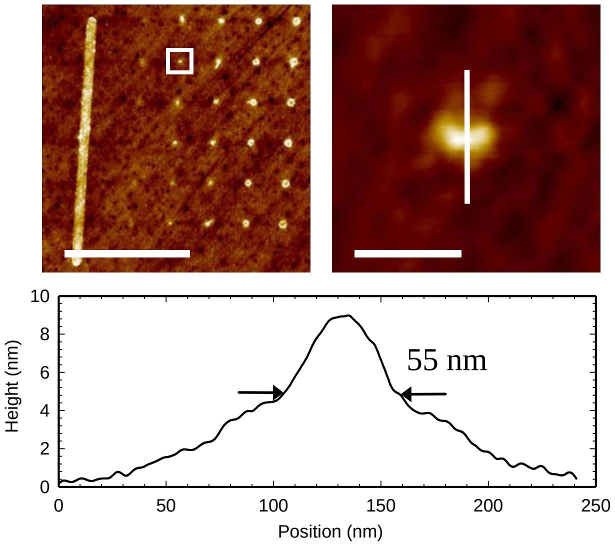

Figure 4.3: (Top left) tapping-mode AFM scan of an array of dots drawn in PPV from a 15 nm film, using a 50 nm probe aperture. From left to right by columns, exposure times (in ms) are 50, 100, 200, 500, and 1000. The large line is a reference feature. (Top right) tapping-mode AFM scan of the feature highlighted, taken to be close to the critical exposure. (Bottom) cross-section through this feature showing FWHM of approximately 55 nm.

4.1.3. Comparison with modelling

Previous work on understanding the mechanism of structure formation in SNOL-patterned PPV films has estimated the minimum achievable feature size by considering the field shape within the precursor film and estimating the size of a *critical insoluble core*. This is defined here as the contour of electric field intensity that just touches the substrate/film interface, and is therefore assumed to represent the shape of the smallest structure anchored to the substrate. Larger structures are assumed to be sub-optimal, whereas smaller features are assumed not to be retained after rinsing. This concept is illustrated schematically in Figure 4.4.

In previous work [54] the experimental minimum dimensions of PPV features produced from a 40 nm thick precursor film were compared with those obtained by simulation of the near-field in the proximity of the probe aperture. In this work, it was assumed that a critical irradiation dose was needed to insolubilise the precursor through to the base of the film, so as to anchor it to the substrate. In this case a large discrepancy was found between the predicted and measured feature sizes, which were attributed to the existence of a partially converted, but not completely hardened phase (a gel phase).

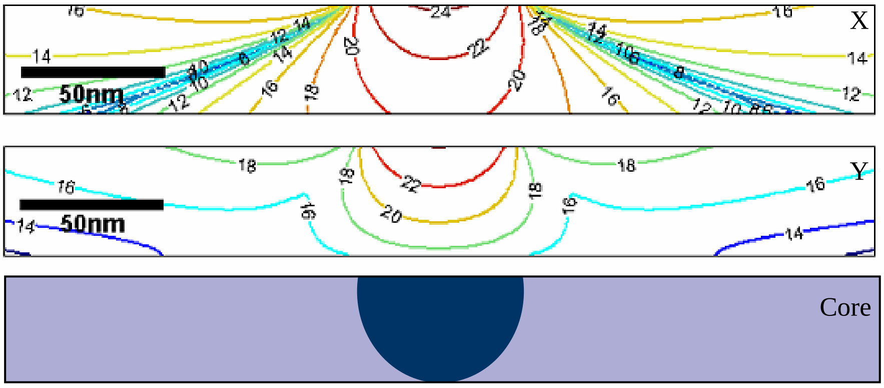

Figure 4.4: Cross-sections showing field strength in two perpendicular directions in a thin film calculated using the Bethe-Bouwkamp model, where the incident light is polarized along the Y-direction. Parameters used are the same as in Figure 2.4, the scale is logarithmic. Lower image shows a schematic of the expected “critical core” formed at optimal exposure for this field.

Evidence of different viscoelastic properties within a single photolithographed dot has also been found [35], which was suggested to result from the collapse of a swollen gel-phase as is also observed in some photoresists upon development [105]. At the lowest exposure that produced features, the features were not securely anchored to the substrates, as is also observed in a number of places in this work: for example array C of Figure 4.20 and in the thermolithographically defined lines in section 5.

Subsequent comparisons for a number of PPV films with thicknesses ranging from 15 nm to 40 nm over a wide range of exposure times and intensities were made, to measure more accurately the dependence of minimum feature size on film thickness, and thus comment on the validity of the critical core model. A sample of data obtained for baked films is presented in Figure 4.5, where the minimum measured FWHM for well-defined features over a number of samples is plotted as a function of film thickness. Film thicknesses have been estimated from previous film measurements and from maximum (unbaked) feature heights. Uncertainties on this data are significant, but it can be seen that the predicted minimum feature size correlates reasonably closely with the size predicted by the critical core model.

Two critical core predictions are shown, one giving the feature width in a direction perpendicular to the incident polarisation, the other in a direction parallel to the polarisation direction. In general, somewhat mixed polarisation is anticipated to be incident on the aperture, since the probe fibres used were not polarisation-maintaining. It is therefore expected that the worst-case (parallel) limit will dominate. It is however surprising that the data lie so close to the model prediction, given that the critical core model does not take into account any non-ideal behaviour of the probe, precursor or development process such as finite skin depth, precursor retention fraction, gel-formation and shrinkage. The role these play is examined in more detail below.

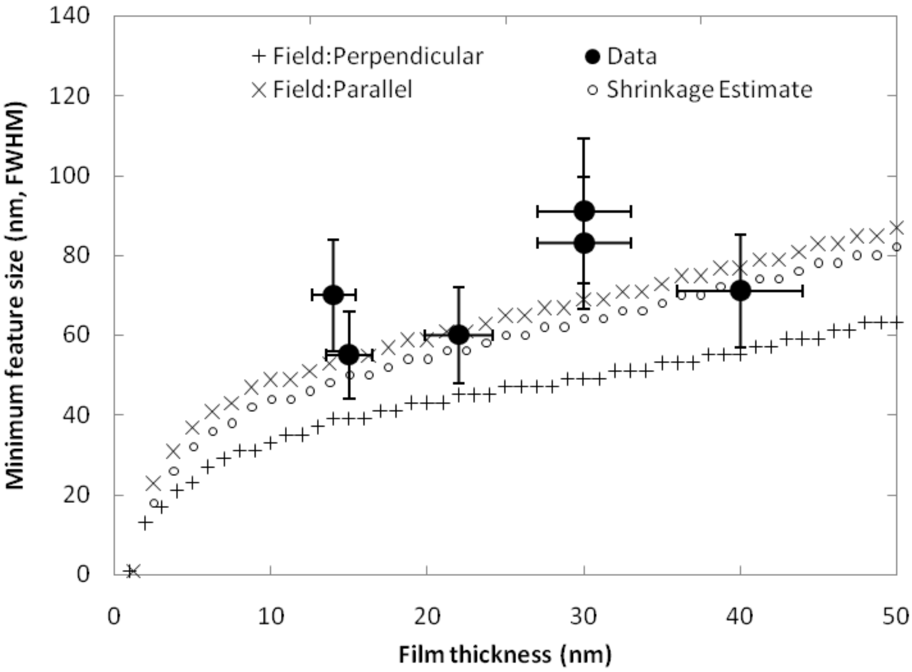

Figure 4.5: Comparison of predicted feature size (parallel and perpendicular to laser polarisation) to recorded feature size for a number of baked samples, using several different probes with nominal aperture 50±10 nm. Error bars indicate the extent of uncertainties on thickness measurements, variation between samples and the uncertainty over how well optimised the minimum feature size is. The shrinkage estimate is explained below.

4.1.4. Feature formation and shrinkage

To understand in more detail how close the dimensions of the features above are to the minimum physically achievable, and why the correspondence to simple modelling is relatively good, the nature of the structures formed by the system and their behaviour during processing has been investigated. For a physical aperture of diameter 50 nm at a negligible distance from an ultrathin precursor film, the ultimate minimum feature size will be given approximately as the sum of the near-field width (comprising aperture size and relative field spread, estimated using the critical core model above), twice the skin depth of the aperture material [106], and twice the characteristic gel thickness of the polymer – that is, the thickness of the transition zone from soluble precursor to fully-insoluble PPV (which is expected to be governed by the gradient of the optical field and the precursor molecular weight).

The skin depth for gold, which forms the aperture and probe cladding, is estimated from literature values of its extinction coefficient [107] to be 14 nm under 325 nm illumination. The gel thickness is hard to predict, due to the gradual increase in solubility away from the critical region as the field strength decreases, and due to chain entanglement effects which could extend the gel phase beyond the gyration radius – possibly even beyond the stretched chain length of the precursor polymer used (~10 nm). However, under optimised conditions and no entanglement, it is not expected that the gel layer will be thicker than the precursor polymer gyration radius (3-4 nm or less [108]). In the absence of a gel phase it is predicted that the minimum feature size of an object drawn in PPV from a 15 nm film under the conditions described will be 90-100 nm across, considerably greater than that that seen. If a significant gel phase exists, or if probe-dither and feedback quality play a role in determining resolution, then the expected feature size would be even larger.

It has previously been reported that bulk PXT films reduce in volume by approximately 50% during vacuum baking, as solvent and reaction products are removed [35]. The same process is observed to occur for the features described here, with the average volume reduction per feature observed to be approximately 45% over a wide range of sizes. However, for individual features, this shrinkage is not uniform. Figure 4.6 compares the relative lateral and vertical shrinkage for a large number of dot features drawn on five different silica substrates. The first point to note is that none of the features had an unbaked width below 110 nm, in reasonable agreement with the prediction above. Furthermore, linear fits to the data indicate that the unbaked widths and heights (W_{ub}, H_{ub}) are approximately related to the baked widths and heights (W_b, H_b) by the relationships:

$$\begin{aligned} W_b &= W_{ub} - 46nm \\ H_b &= 0.7H_{ub} + 3nm \end{aligned} \tag{4.1}$$

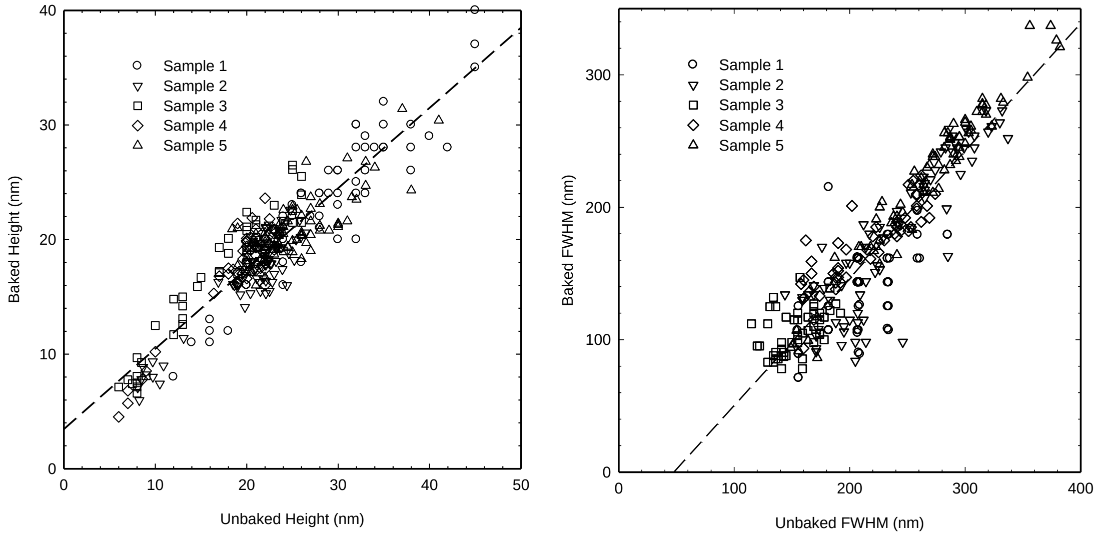

Figure 4.6: Comparison of heights and FWHM for features drawn in PPV on five different samples both before and after the post-process vacuum bake. Linear trend lines have been added which give equal weighting to all points. Fitting parameters are $W_b = 0.962W_{ub} - 45.98$ nm and $H_b = 0.701H_{ub} + 3.46$ nm.

The lateral shrinkage therefore is almost constant, with a fixed reduction in feature width of around 45 nm, whereas the features shrink proportionally by around 30% in the vertical direction. This is interpreted as a pinning of the features to the surface of the substrate, preventing lateral bulk shrinkage except for the collapse of outer layers of the features with characteristic width of around 20-25 nm. This is likely due to a collapse of the thin gel phase described above in combination with partial shrinkage of the bulk. The remaining bulk shrinkage is taken up by a collapse in the feature height. If this trend remains valid for the smallest features achieved, then it is expected that the 55 nm baked feature demonstrated in Figure 4.3 would arise from a 100 nm original feature, in good agreement with the estimated theoretical limit and therefore assumed to be very close to optimal for this system.

Furthermore, an estimate of the dependence of feature size on film thickness may be made by combining the critical core model with the assumption made above. The broadening effect of adding a more realistic formation process to the pure critical core model is almost entirely cancelled out by the inclusion of lateral shrinking behaviour. The resulting estimate (with significant uncertainty) for the expected post-baked feature size is plotted in Figure 4.5.

This analysis is able to account more completely for the somewhat unexpected accuracy of the pure critical-core model for the films studied. However, this is still not a complete account of structure formation. The model cannot, for instance, account for the evolution of feature shape away from optimal exposure conditions. In particular, the semi-hollow features and ridge-like edge effects seen in Figure 4.3, and for many other samples.

4.1.5. Mass loss

It has previously been shown that forming PPV via photolithography does not cause significant damage to the material, compared to standard thermal treatments, as demonstrated by the undiminished photoluminescence (PL) efficiency of the converted material [35]. However, it has been observed that over-exposure of the PXT precursor does lead to degradation of the material. For instance, photo-bleaching is commonly observed. Additionally, mass loss associated with individual features is seen, and interpreted as being due to a resolubilisation of the converted PPV. In bulk films, this effect has been studied by Cotton *et al* [109], who spun films of PXT from methanol and noted that the retained film thickness varied as a function of illumination dose. It was further noted that film thickness itself is a difficult quantity to measure accurately, since by definition it is an average quantity estimated from discrete measurements. However, it was also observed by the same authors that a representative proxy for film thickness could be obtained by measuring the integrated absorbance under the 420 nm peak associated with PPV (but not PXT). To establish the dependence of mass loss on exposure dose and exposure intensity, film–retention experiments were conducted in air using both a continuous wave HeCd laser at 325 nm and a pulsed Nitrogen laser at 337 nm (operating at 10^7 times the peak power of the HeCd). Figure 4.7, adapted from [109], demonstrates that the position of peak absorbance – and so peak film-retention – does not depend on radiation intensity or film thickness. The absorbance profile does however depend strongly on total radiation dose. A maximum is observed, below which the PXT appears not to be fully converted, and above which it appears to undergo some form of degradation.

Similar experiments carried out in nitrogen show that lowering the oxygen content reduces this trend, while eliminating both oxygen and the methanol solvent under vacuum seems to remove it entirely (Figure 4.8).

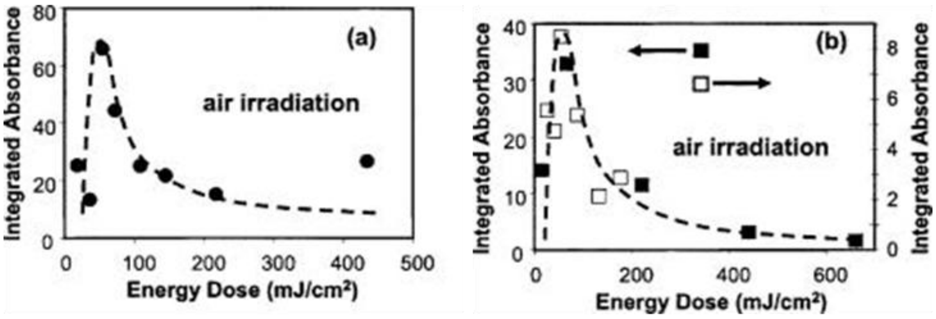

Figure 4.7: Variation of integrated absorbance with applied energy dose for samples irradiated with a) a HeCd laser and b) a N_2 laser in air. Initial PXT film thicknesses are 60 nm (filled circles), 70 nm (filled squares), and 10 nm (open squares). Adapted from [109].

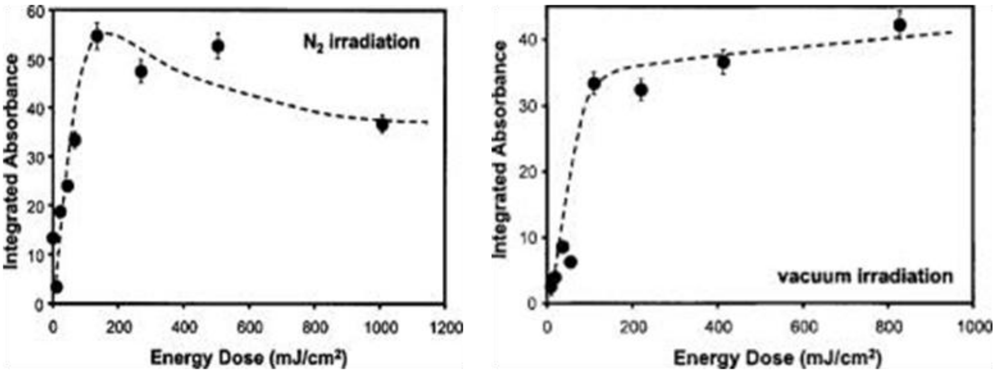

Figure 4.8: Variation of integrated absorbance with energy dose for samples irradiated with a HeCd laser under (left) nitrogen and (right) vacuum (1×10^{-6} Torr). Adapted from [109].

The mechanism for resolubilisation of the PPV can be understood in terms of these results. The PXT precursor is initially soluble in methanol. Irradiation by UV leads to removal of the sulphonium leaving group, producing a reactive intermediary. In vacuum, this intermediary subsequently forms a vinylene bond, as desired. In the presence of residual solvent, for example when the material is exposed in an inert atmosphere such as nitrogen at ambient pressure, additional reaction pathways become available. Depending on the solvent used, either hydroxyl or methoxyl groups can react at the site vacated by the sulphonium group.

This process is enhanced in a more reactive atmosphere such as air, with an additional pathway of simple oxidation available. At very high doses, direct cross-linking between chains or cleavage may occur. While the formation of a vinyl group reduces the average solubility of the chain, the addition of side groups or a reduction in chain length through cleavage will tend to increase the solubility, leading to loss of the exposed material. Direct cross-linking at high doses decreases the solubility, but also detrimentally affects the semiconducting properties of the resulting PPV film. An empirical model for this process was developed by Cotton *et al*, as applied to bulk films, and used to predict the optimal doses required for conversion.

A more complicated, but related, phenomenon is observed in isolated structures created with the near-field probe. Since the field strength varies rapidly in the vicinity of the aperture, so does the proportion of the film retained. Even taking into account the effects of core size, characterising how this process affects the structures formed is vital for correctly interpreting the results of lithography. The effect of this variation in film retention can be seen in Figure 4.9, which presents a series of features drawn in a 25 nm thick PXT film at varying exposure doses. The variable film retention manifests as a progressive “hollowing-out” of the features as exposure dose increases. All images were obtained using Dimension 3100 AFM operating in tapping-mode using ultra-sharp Silicon cantilevers with <10 nm nominal tip radius. Figure 4.10 presents cross-sections through these features so that direct comparison can be made. Effective exposure times are shown, calculated as equivalent exposure at full laser intensity through the probe – actual times were longer, but the laser intensity was reduced from its maximum using neutral density filters.

The features shown in Figure 4.9 are indexed by effective exposure time, rather than estimated exposure dose, due to the extreme difficulty of accurately determining the absolute three-dimensional local energy density under the near-field probe. At full intensity, power transmitted through the probe at 325 nm is estimated to be approximately 125nW, assuming 25mW incident laser power, ~10% coupling efficiency into the fibre, ~10% transmittance though 2m of the fibre and 0.05% (far-field) transmittance though the aperture (the latter from manufacturer’s data, taken at 630nm). Over an area estimated at 50x50nm, this gives a projected dose of the order 5kW/cm^2. The transmitted intensity in the near-field through the aperture is likely to be larger, though the metal coating of the probe may also absorb UV light. As a result of these approximations, uncertainty on the power value is extremely large. Finally, this is only an estimated average power, and the high field gradients under the aperture ensure that local field strengths will differ over orders of magnitude.

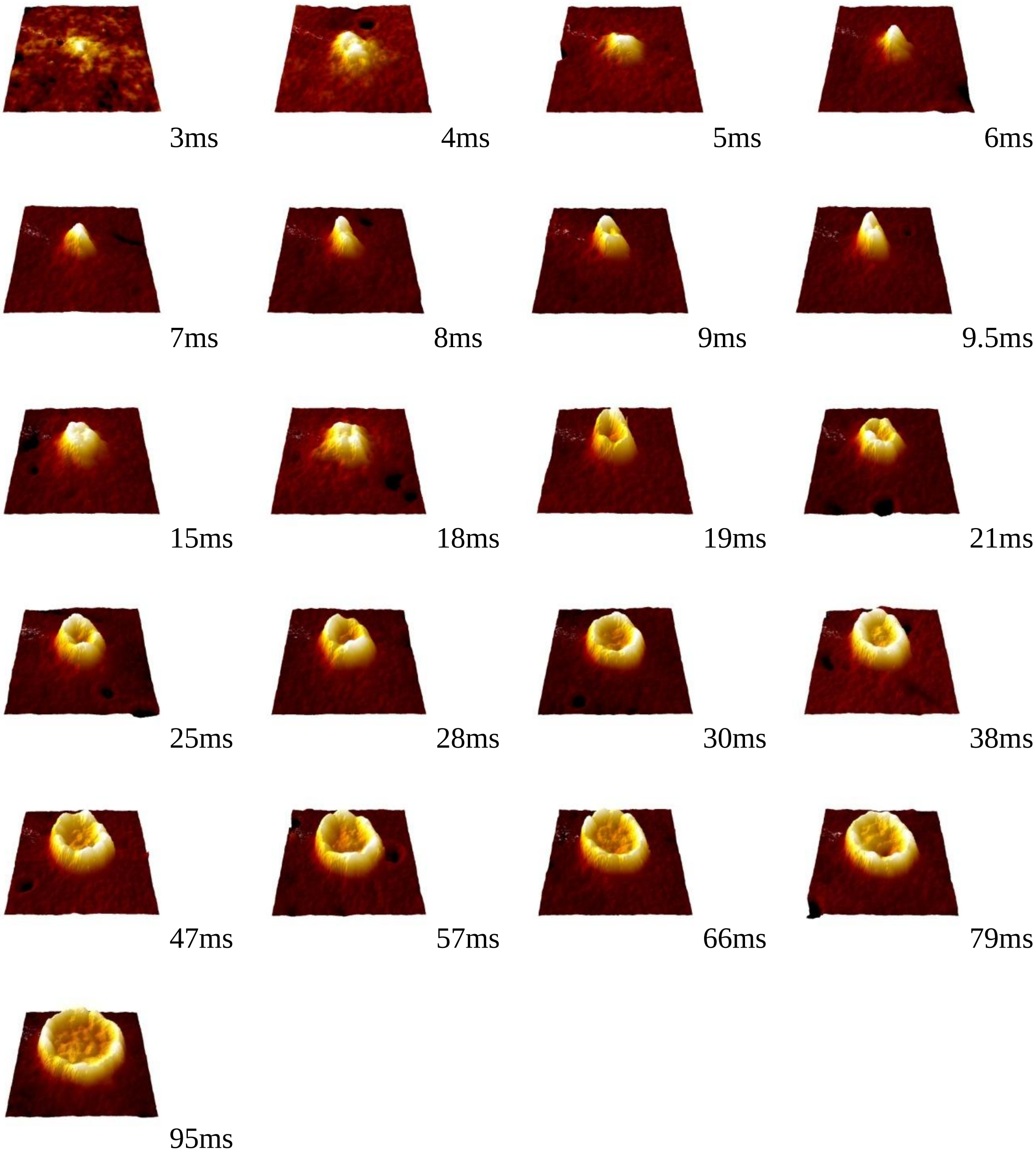

Figure 4.9: Series of 500nm-square images taken of baked features created from a 25 nm film using differing doses from a SNOL probe operating at 325 nm. All are drawn with a 25 nm vertical scale. The progression from underexposed features (top) to overexposed features (bottom) shows the progressive insolubilisation then resolubilisation of the film.

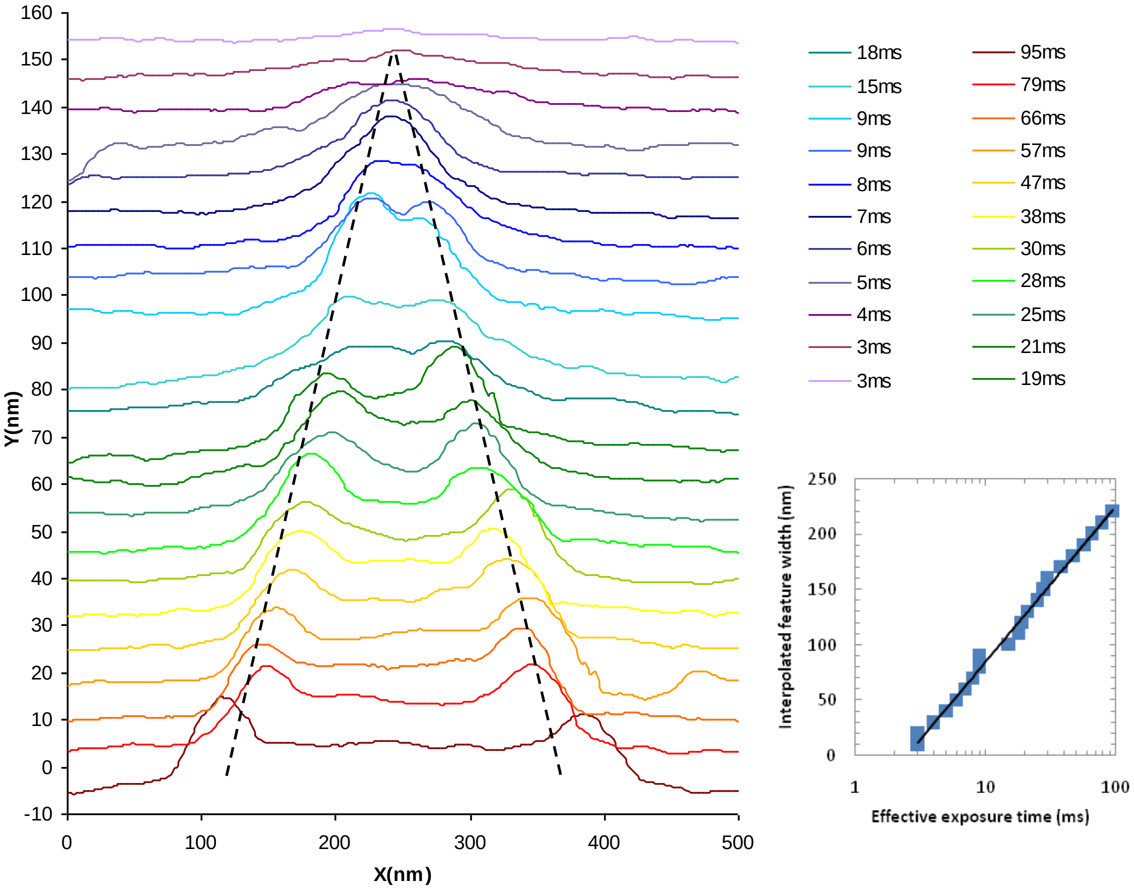

Figure 4.10: Cross-sections, offset for clarity, corresponding to different effective exposure times (shown right) underneath the SNOL probe, corresponding to the images shown in Figure 4.9. Dashed lines highlight the approximately linear trend between feature width and sample number. Inset shows logarithmic dependence of feature width on exposure time, assuming this trend holds.

It has previously been suggested that the ridges formed around the edges of lithographically defined features such as those illustrated in Figure 4.9 are the result of a large, partially converted gel-phase [35]. The discovery of an outer ring to structures fabricated using a SNOL system, visible in AFM phase images as a slight increase in the local phase signal, were interpreted as due to a region of softer material. These outer rings in the phase image are also observed for the structures presented above, and are shown in Figure 4.11. The ring is absent for normally-exposed features (e.g. 5 ms), but grows as the feature becomes overexposed (e.g. 25 ms, 95 ms). Overlaying the phase and topographic images show that, for these structures, the higher phase shift (indicative of higher damping) correlates with the regions of steepest topography – both inside and outside the outer ring – suggesting that they can also be explained by the increased interaction of the AFM probe with steeper surfaces (except for the “inner southern” surface here, which can be interpreted as the surface towards which the AFM tip was oriented). No features indicative of a softening of the structure around its outer ring are therefore resolved. In addition, as the data on structure formation and shrinkage discussed in section 4.1.4 is consistent with the gel region being rather small, an alternative explanation for the ridge formation must be sought for these features.

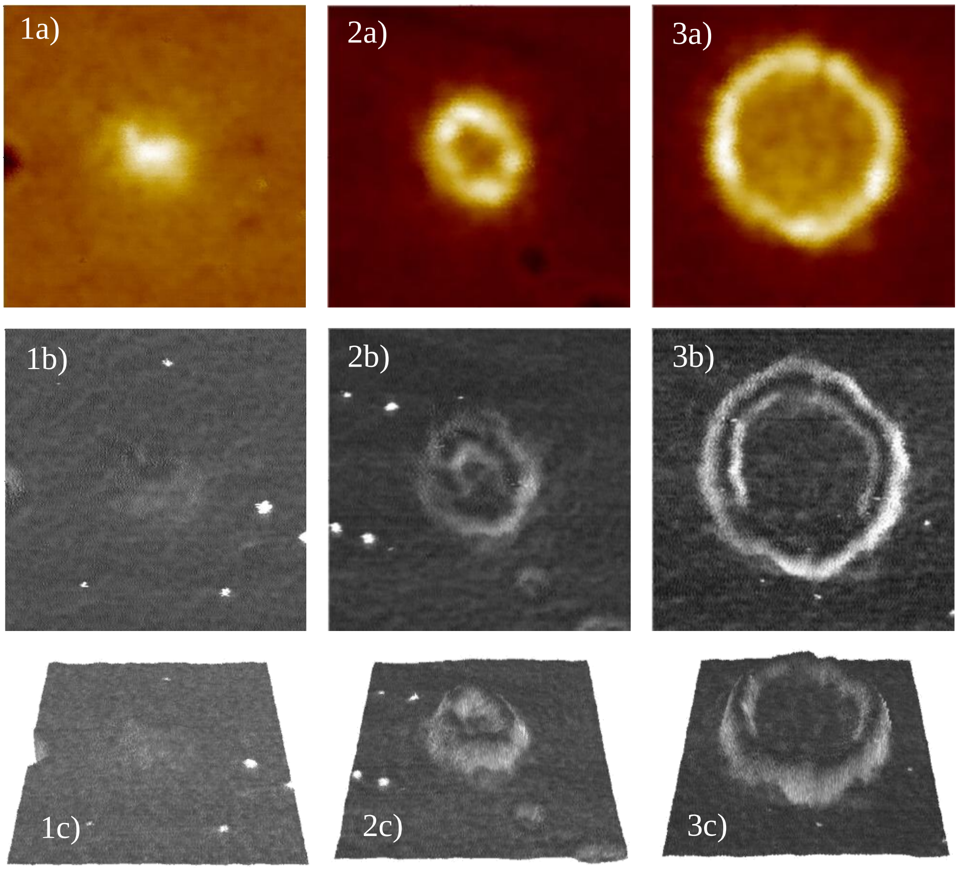

Figure 4.11: 500 × 500 nm tapping-mode AFM images showing a) topography (vertical range 25nm), b) phase (±20° range) and c) overlaid phase on topography of the 1) 5 ms, 2) 25 ms and 3) 95 ms dots presented in Figure 4.9. Note that the phase ring(s) track the steepest topographic gradients.

It can be seen from the progression in Figure 4.10 that an alternative interpretation of the ridges is as regions of optimal exposure, inside of which the material has been partially resolubilised and removed during development. Cotton *et al* modelled the resolubilisation processes by considering reaction rates of individual pathways and fitting the resulting model to retention data recorded after exposing a bulk film to uniform dose of UV radiation. The results give a good prediction for the retention fraction of a thin film under air, ranging from partial exposure, via optimal dose, to overexposure resulting in the eventual breakdown of the material.

While this model strictly applies to bulk films, it gives a useful starting point for modelling the detailed response of a thin film to local exposure such as that generated by the near-field probes. The detailed structure of the resulting features, after development and post-process baking, can be understood by examining the behaviour of the precursor material during conversion, combined with the field shape predicted by the Bethe-Bouwkamp calculations described previously. The approximation is made that the local solubility of a small region within the film will be related to total exposure dose according to the empirical data published by Cotton.

Under the assumption that light incident on the aperture is polarised horizontally with respect to the images below, the parallel and perpendicularly polarised components of the near-field in the aperture (reproduced in Figure 4.12a,b) are combined to generate a 2D field intensity map at the aperture (Figure 4.12c). Each component is then propagated down to the sample to obtain an intensity profile at the surface (Figure 4.12d). Finally, as described in section 2.6, the field is propagated through the sample and 2D intensity slices are obtained. Figure 4.13 shows examples of such intensity slices for a 20 nm film, plotted on a logarithmic scale to enhance the fine structure of the field.

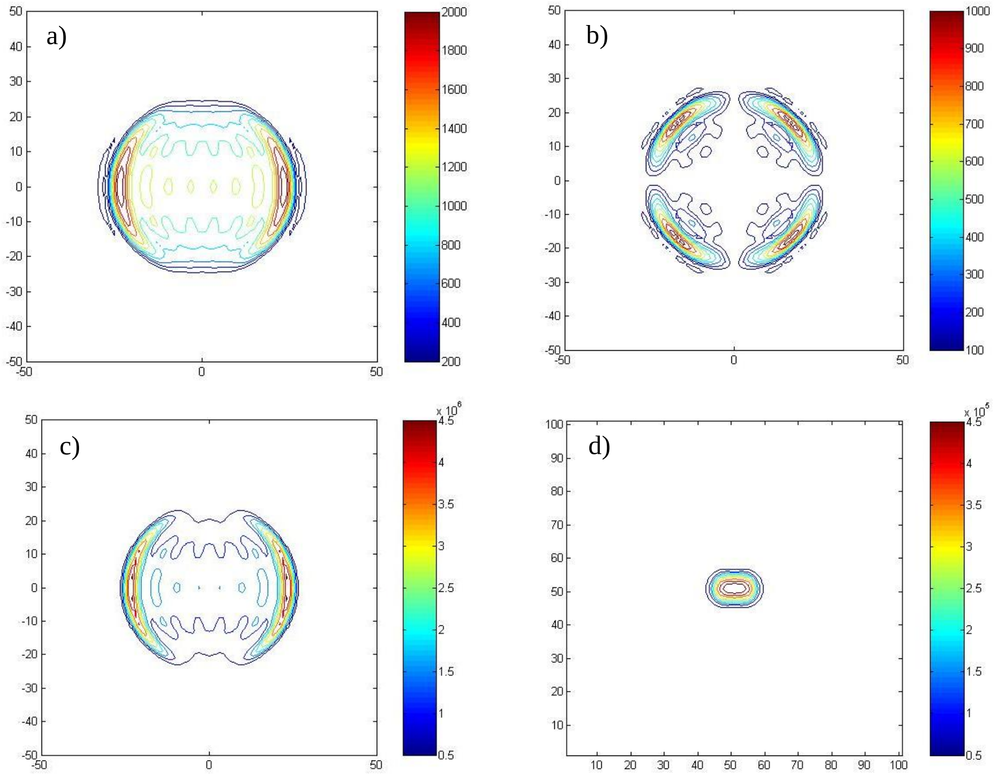

Figure 4.12: Field amplitude within a 50 nm probe aperture calculated using the Bethe-Bouwkamp model with transmitted polarisation a) parallel and b) perpendicular to the incident polarisation. Also shown are total field *intensities* c) within the aperture plane and d) at the sample surface.

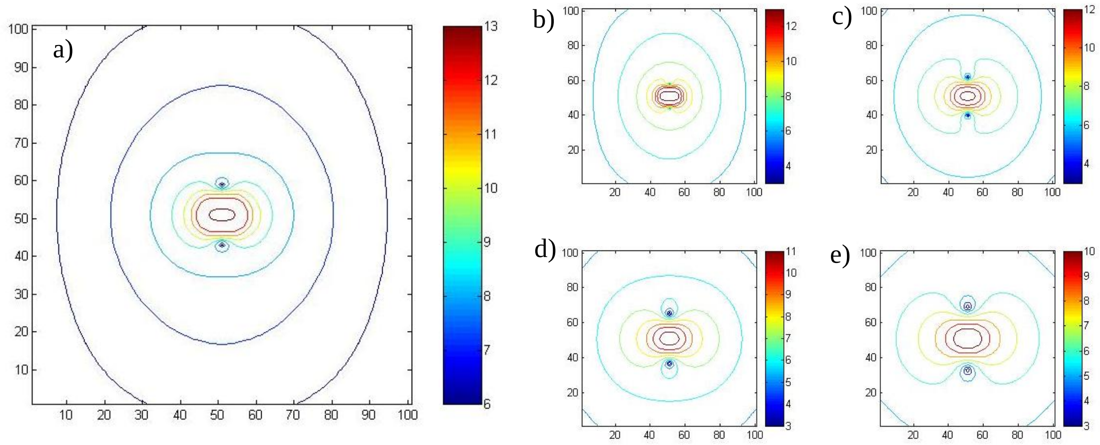

Figure 4.13: Logarithm of field intensity calculated over a 100 × 100 nm area of 20 nm thick film. Depths are a) 0 nm (surface), b) 1nm, c) 6nm, d) 10 nm and e) 14 nm.

Combining these slices gives a three-dimensional mesh of intensity values spread over a simulated film volume. A suitable constant scaling factor was chosen to represent illumination intensity, and the intensity profile multiplied by exposure time to obtain a total dose per point. For the purpose of simplifying this model, the anchoring concept implicit in the critical core approach is ignored, since it cannot in any case predict the sub-critical features observed at low exposure. Instead it is assumed that the retained film thickness above a point on the substrate can be regarded as a vertical sum of the film retention fraction at all heights above this point. The film retention fraction is calculated at each point by assuming a functional form of retention fraction versus exposure dose identical to the experimental trend reported by Cotton *et al* for PPV films in air.

Figure 4.14 presents a set of simulated features for a logarithmically distributed series of exposure times generated in a 400 × 400 nm area of a 20 nm thick PXT/PPV film. Due to the unknown field intensity, exposure times have been scaled such that the simulated and measured feature shapes at 66 ms exposure roughly correspond. The results of this modelling reproduce the ridge structure seen in the real data very closely, and confirm the structure shape as being the result of an interaction between insolubilisation and resolubilisation processes. The detailed structures of the real shapes are further determined by the factors outlined in section 4.1.4, as is any subsequent shrinkage.

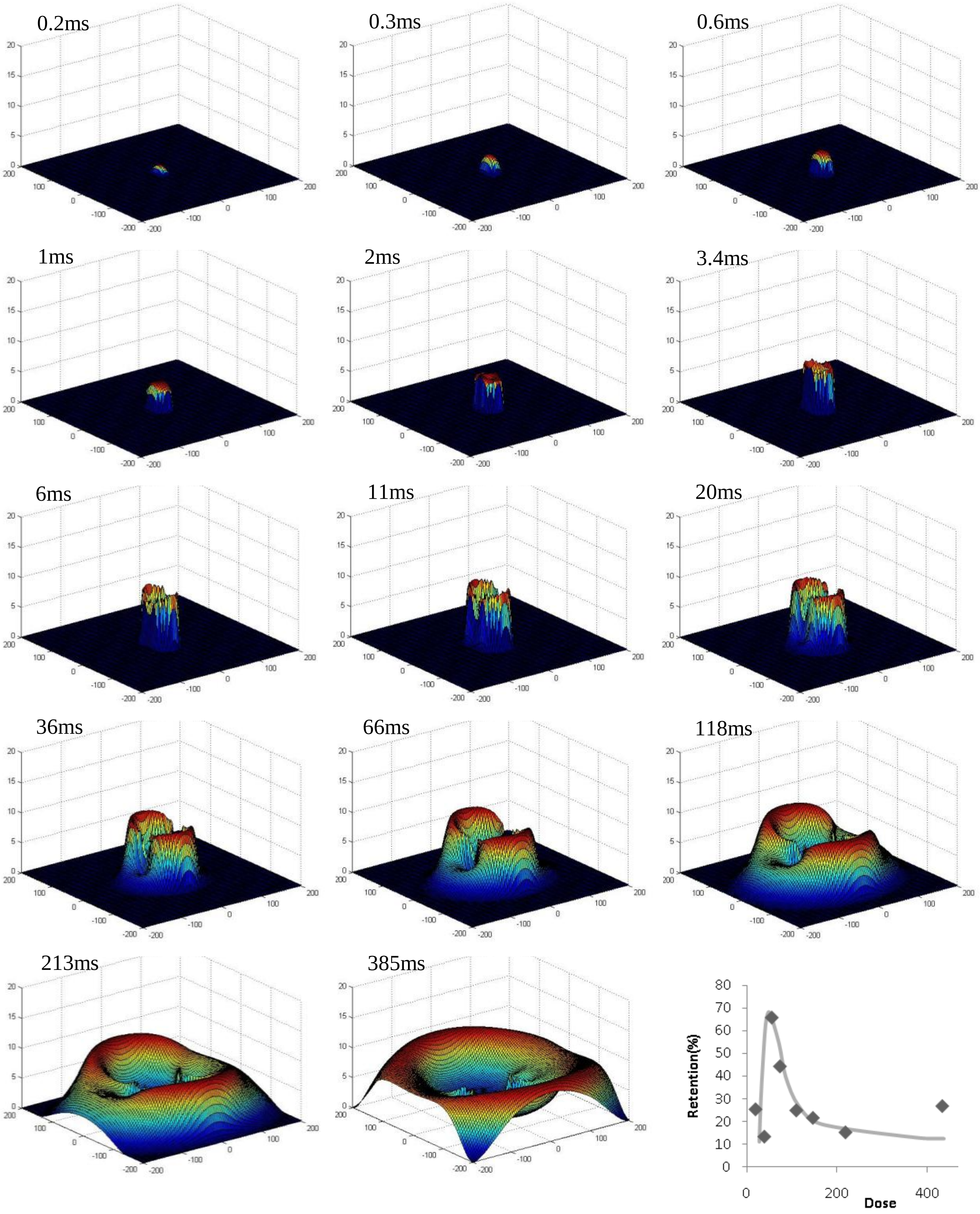

Figure 4.14: Simulated structures formed in a 20 nm thick PXT film, assuming a perfect near-field profile and the retention function reproduced bottom right. Exposure times are shown, and referenced to 66 ms exposure. All scales are in nm.

It is interesting to note that despite these caveats, and the fact that in general a mixed polarisation will be incident on the aperture, dips in film retention at the low-field nodes predicted by the Bethe-Bouwkamp model are present in many of the real features. The minimum feature sizes observed for structures in PPV, and also the evolution of feature shape with exposure dose, can therefore be explained. It can also be concluded that large features in thick PPV films will not be achievable using this technique under ambient conditions, due to the resolubilisation processes seen at high excitation doses. Finally, it is implicit in the modelling, and reflected in the data, that the field near to the aperture is dominated by evanescent components, with the weak far-field background not influencing structure formation.

4.1.6. Role of substrate reflections on field profile

The modelling of the near-field presented previously offers a good explanation for the resolution limits encountered when patterning materials on a transparent substrate. Implicit in this explanation is the assumption that, due to the close matching of refractive indices between the typical polymers/precursors encountered above and the standard quartz substrates used (the refractive index of PXT is approximately 1.73+0.067i at 325nm, whereas that of fused quartz is approximately 1.48), reflections at the substrate/organic interface are unimportant.

Modelling work undertaken by Dr Oliver Fenwick at UCL [110] to quantify this effect considered a representation of the near-field as outlined in previous sections, then allowed further propagation back and forth between the organic/substrate interface and the organic/air interface. The reflections were cut off after 10 propagations and the total field strength summed over all reflected components. Reflections from the back of the substrate were neglected, and no far-field leakage through the probe was considered. By varying the substrate refractive index, the effects of altering the substrate material could be quantified. Given that the organic layer is typically chosen to be a functional material, and therefore envisioned to form part of a device architecture, insulating substrates (Spectrosil quartz, refractive index as previously), conducting substrates (Aluminium, $n_{Al}\big|_{\lambda=325nm} = 0.326 + 3.95i$ [107]) and semiconducting substrates (Silicon, $n_{Si}\big|_{\lambda=325nm} = 5.052 + 3.211i$) [107]) were considered.

From this modelling, the following results may be extracted. By considering the on-axis field intensity as a function of depth in a 20 nm organic film (assumed here to be PXT), it can be seen in Figure 4.15a that the effect of reflections is negligible for fused quartz as compared to the field with no reflections added. This confirms the validity of the assumption made previously. However, the addition of a highly reflective substrate

(Al/Si) has a dramatic effect on the field intensity, reducing it by 30% at the top interface, and reducing it to almost zero at the organic:Al/Si interface due to low penetration of the field into the attenuating medium. The effect of the reflections is also to cause the field shape to alter above the reflective surface. By considering the effect of the modified field shape on the diameter of the critical insoluble core, Dr Fenwick was able to estimate the change in feature size resulting from the change in substrate, as a function of film thickness. Figure 4.15b reproduces this data, again showing that while the addition of reflections from Spectrosil has a negligible effect, reflections from the Aluminium and Silicon act to significantly broaden the core size, with the effect increasing with film thickness. Crucially, the effect of altering the substrate reflectivity is significantly larger than the effect of increasing the film thickness (for the thin films modelled here).

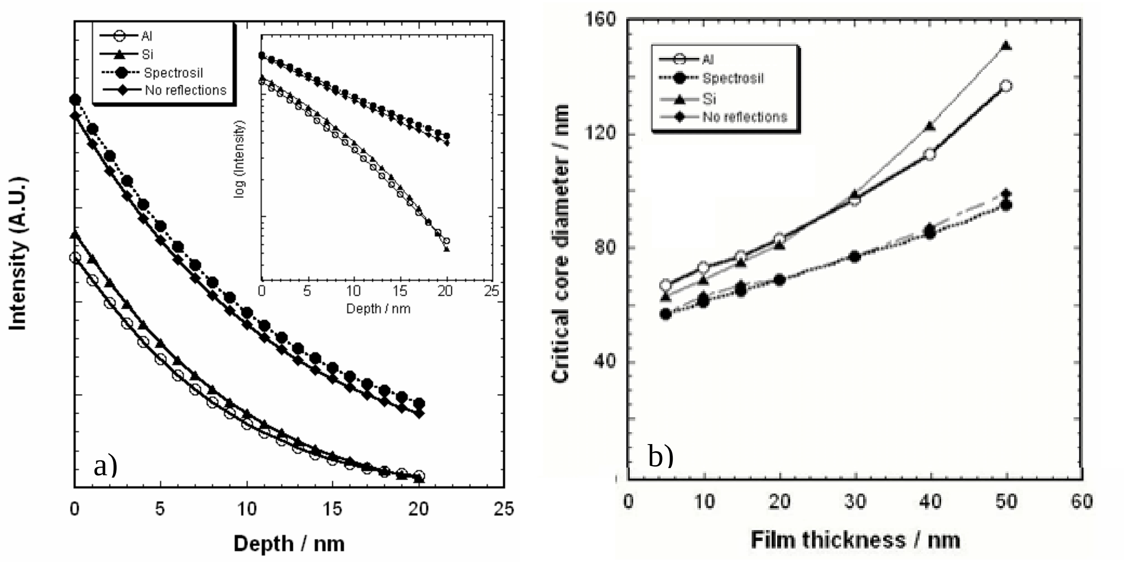

Figure 4.15: a) On-axis intensity profile as a function of depth simulated through a 20 nm film on various substrates. Inset shows same data plotted on a logarithmic scale. b) Estimation of critical-core diameter as a function of film thickness for various substrates. Reproduced from [110].

To test the validity of this modelling, pre-prepared transistor substrates were obtained from the University of Cambridge, consisting of a thick (300nm) layer of thermally grown silicon dioxide on top of a base of doped silicon. Gold electrodes, with a separation of 5 µm and thickness 50nm, had been evaporated on top in an interdigitated configuration. Silicon dioxide is expected in this situation to behave very similarly to quartz, since the rapid decay of the near-field intensity precludes interactions with the underlying doped silicon. Gold is expected to behave similarly to aluminium, as both are good reflectors. Because of the differences between the film/substrates described in the initial modelling, and the films/substrates described below, quantitative comparisons are not possible, but qualitative relationships are still expected to hold.

PXT precursor (as previously described) was spun at 3000rpm for three minutes to form a film approximately 100 nm thick above the electrodes and in excess of 200 nm between them – the solution appeared to pool preferentially on the silicon dioxide rather than the gold. This may reduce the relative importance of reflections in the silica region, but the effect is expected to be marginal given the already weak reflections that silica provides. Arrays of 18 µm lines bridging the electrodes were illuminated using the SNOL probe operating with 325 nm illumination, supplied as previously, through an OD1 filter to reduce beam intensity. Alignment of the lines relative to the gaps between the electrodes was achieved using the AFM functionality of the SNOL system to locate the appropriate areas. After developing in methanol and de-ionised water, and baking under vacuum, the resulting structures were imaged using a conventional AFM, and are shown in Figure 4.16, Figure 4.17 and Figure 4.18 along with representative cross-sections. Key observations on these results are summarised in Table 1 below.

It is clear that the evidence supports the predictions made by Dr Fenwick’s model, indicating that consideration of reflections is an important contributing factor to the achievable resolution of SNOL, and that substrate behaviour plays a larger role than film thickness in determining both lithographic resolution and field structure.

Given the convenient layout of the substrates used, measurement of the conductivity of the resulting polymer microwires was attempted. However, the measurement system used was not sufficiently sensitive to resolve the very low currents involved. As a result it cannot be confirmed whether these wires remained electrically functional after deposition.

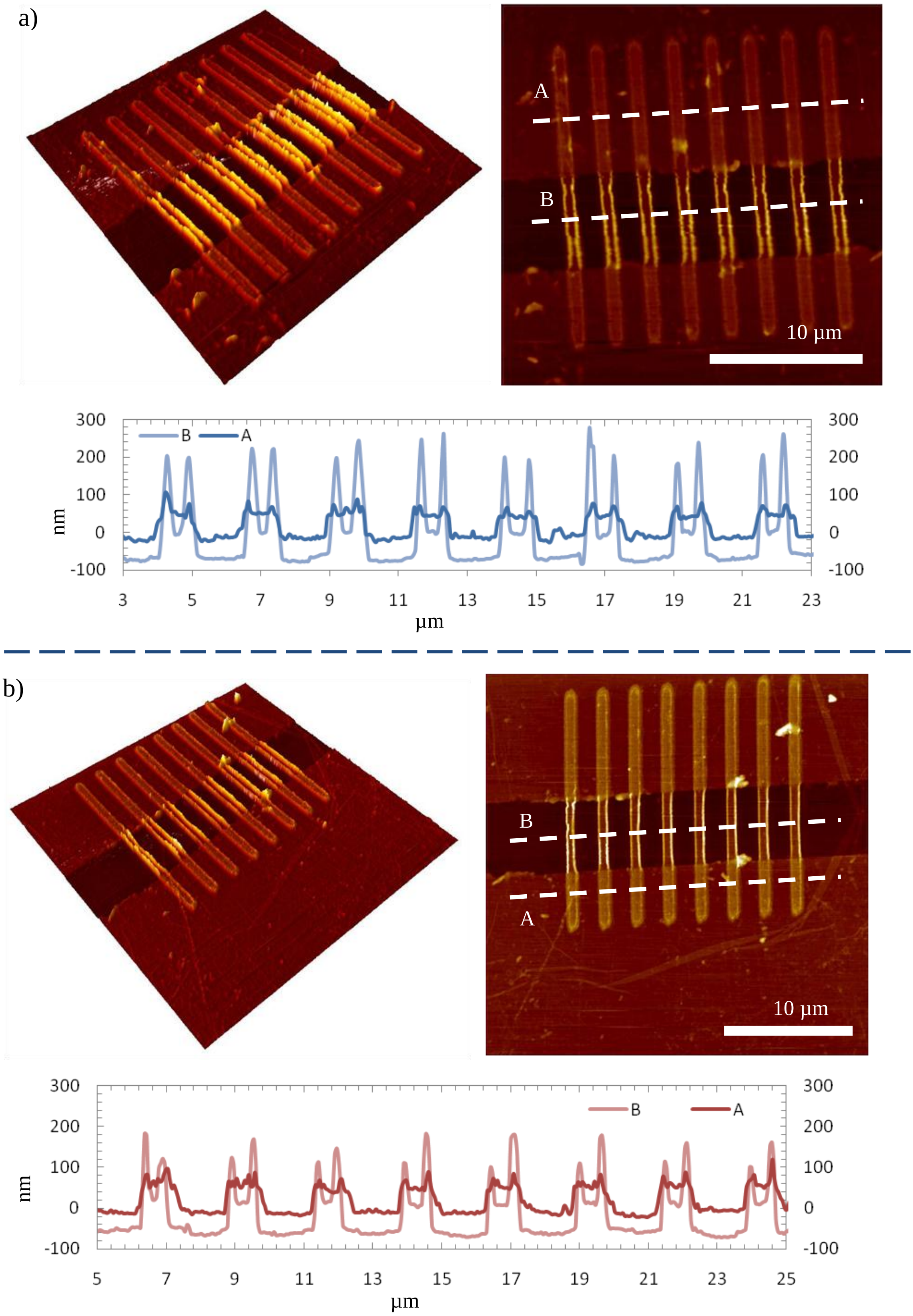

Figure 4.16: Tapping-mode AFM images of lithographically defined wires at different electrode gap positions. Image processing has been restricted to linewise levelling and removal of large debris. Vertical ranges are a) 394nm, b) 420 nm. Cross-sections through the wires are illustrated on the images, and plotted below them.

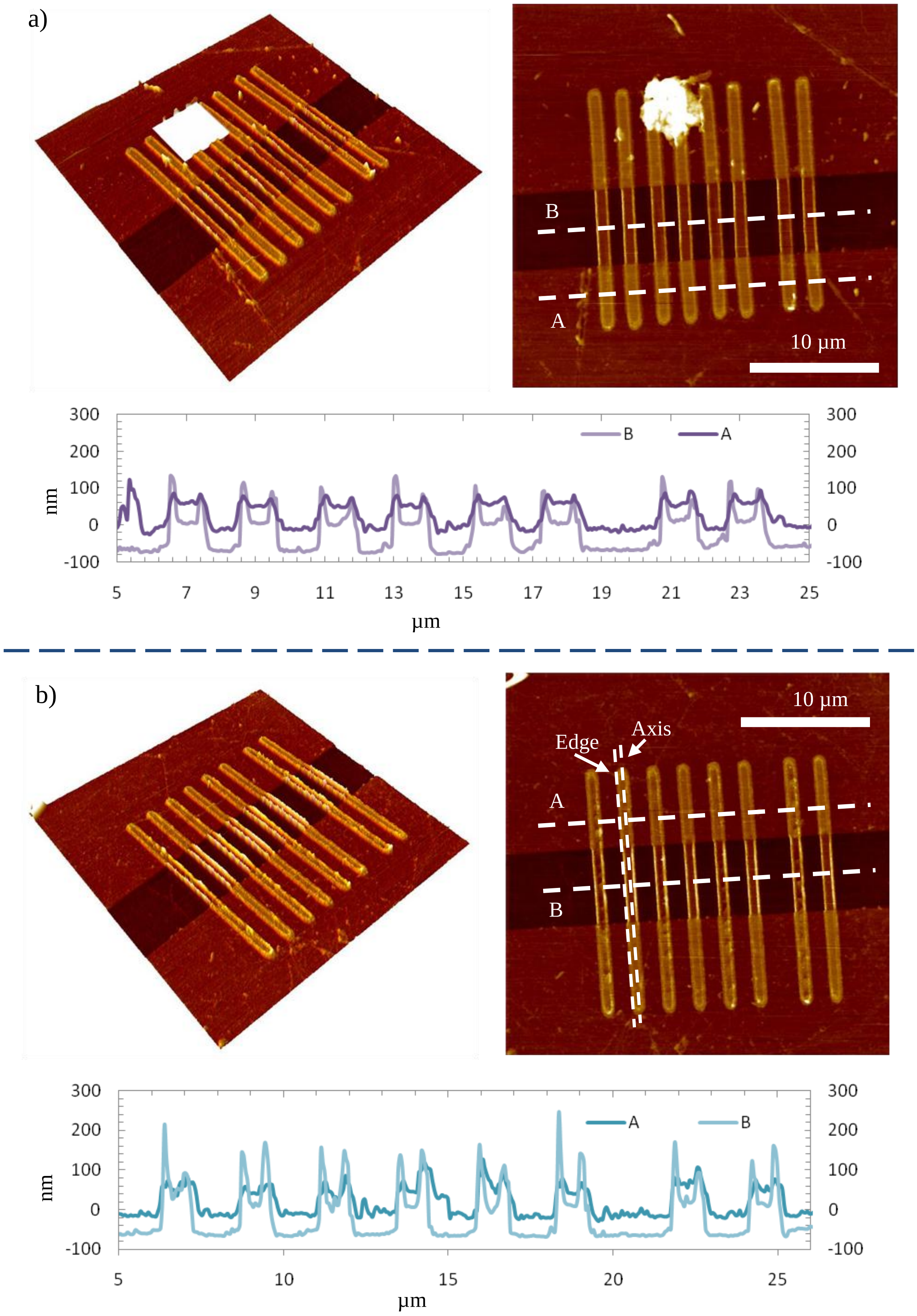

Figure 4.17: Tapping-mode AFM images of lithographically defined wires at different electrode gap positions. Image processing has been restricted to linewise levelling and removal of large debris. Vertical ranges are a) 333 nm and b) 440 nm. Cross-sections through the wires are illustrated on the images, and plotted below them. Edge and axis cross-sections refer to those presented in Figure 4.18 below.

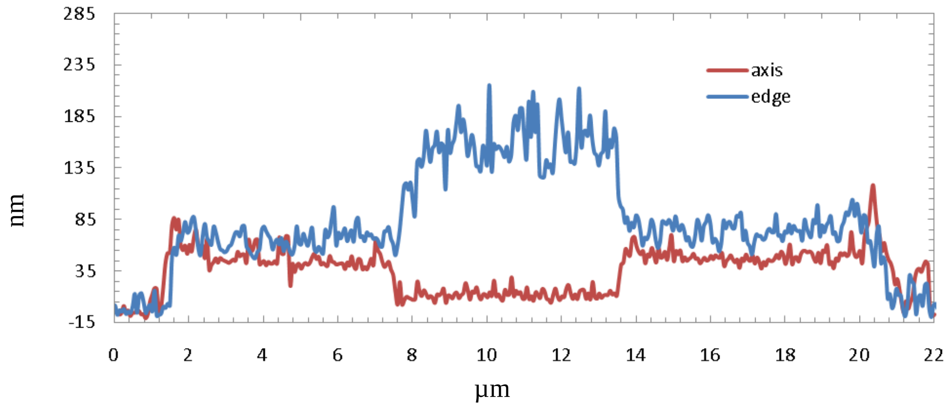

Figure 4.18: On-axis cross-sections through Figure 4.17b on equally scaled axes, offset so that the electrode levels align. The edge:axis height ratio is considerably higher within the gap than on the electrodes.

Table 1: Summary of predictions from reflection model and experimental observations

Reflection model prediction	**Prediction if reflections unimportant**
Field intensity above non-reflective substrate higher than field intensity above reflective substrate	Field intensity dependent only on film thickness. Intensity gradient decreases with film thickness
Experimental Evidence	
Edge-to-axis aspect ratio in range 2-4 for lines above silica, indicating highly inhomogeneous illumination. Aspect ratio in range 1.1-1.3 for lines above gold, indicating relatively homogeneous illumination. Relative mass loss at centre of lines above silica is significantly higher than that above gold (Figure 4.18, on-axis section). These observations indicate that both higher field intensity and larger field gradients are present above silica, despite the apparently thicker precursor film.	
Reflection model prediction	**Prediction if reflections unimportant**
Field shape broader above reflective substrate than above non-reflective substrate	Field shape constant, field broadens with depth. Feature width increases with film depth
Experimental Evidence	
FWHM of main body of lines above silica (ignoring edge spikes) are less than or equal to FWHM of lines above gold. This is consistent with the field profile above gold being broader than that above silica, despite the thinner precursor film.	

4.1.7. Complex patterning at high resolution

While dot patterns are useful both for photonic structures and for characterising the techniques used, it is important to test whether such a high resolution can be maintained over larger and more complex structures, and hence whether the technique is applicable over a variety of length-scales - a requirement outlined previously. To demonstrate this, a large (20 x 20 μm) structure was drawn in PPV, generated from ~65,000 individual pixels, with a variety of feature sizes ranging from microns down to tens of nanometres. In this case, the logo of my institution, the London Centre for Nanotechnology, was used, although more functional patterns are clearly possible. Figure 4.19 shows a tapping-mode AFM image of the final structure. The insets examine some of the smaller scale features of the image demonstrating a typical feature size of 60-70 nm. Thus, length-scales of patterning covering more than two orders of magnitude have been demonstrated, whilst preserving the integrity of the aperture. It should be noted however that due to the necessarily low throughput of the SNOL system, creating patterns such as these requires several hours.

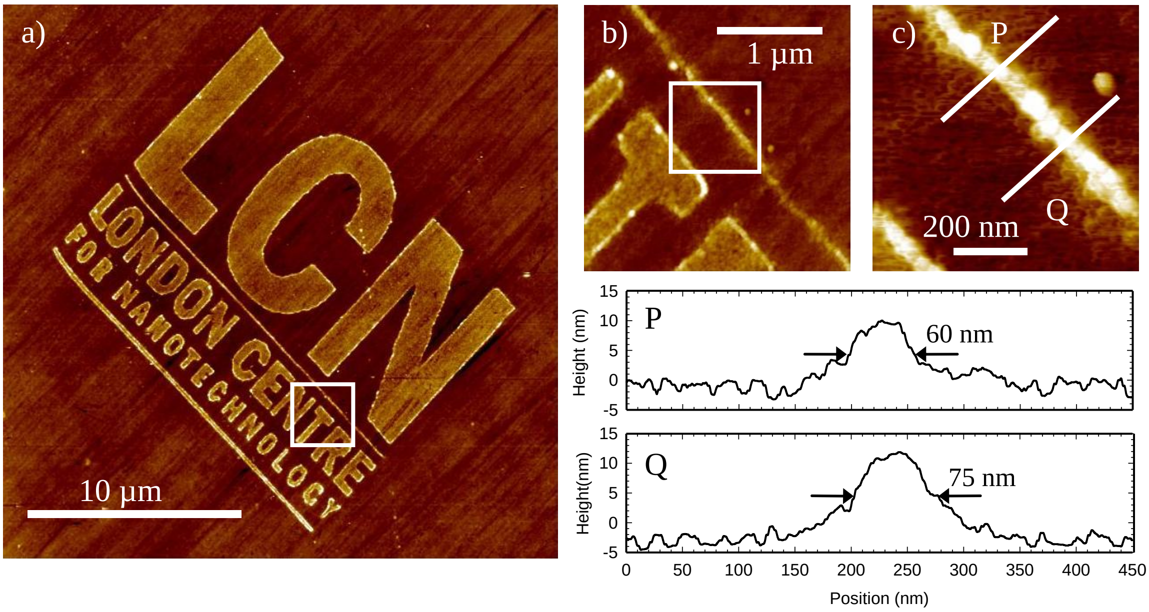

Figure 4.19: a) Tapping-mode AFM scan of my institution's logo drawn by SNOL as a large array of overlapping dots in PPV. Precursor film thickness was ~15 nm, exposure was through a 50 nm aperture with λ = 325 nm. Striated background features are interpreted as polishing marks on the quartz substrate. b) Tapping-mode AFM scan of the area highlighted in the top image. c) Tapping-mode AFM image zoomed-in to highlight the smallest features of the design, with two representative cross-sections defined. The cross-sections P and Q show typical feature size of around 60-70 nm. Adapted from [111].

4.2. Lithography of F8Ox

F8Ox is based on the common luminescent polymer poly(9,9’-dioctylfluorene), F8. The insolubilisation method differs significantly from that used for PPV, in that the F8 is functionalised with long side chains with oxetane end groups [33], In the presence of a photoacid initiator, these can cross-link to form an insoluble reticulated network (r-F8Ox) [112]. Previously reported examples of blue-emitting cross-linkable polymers also include non-conjugated polymethacrylates bearing distyryl benzene and cinnamoyl groups [113].

The insolubility of the polymer network after processing has previously led to r-F8Ox being used in the fabrication of multilayer LEDs, negating the need to use orthogonal solvents between layers. A similar technique has been demonstrated for the cross-linking of a PEDOT:PSS interlayer in an LED device, potentially allowing the use of water-soluble active layers which would otherwise re-dissolve the PEDOT:PSS [114]. Two effects of including an r-F8Ox interlayer have been noted. When used as a 25 nm interlayer between PEDOT:PSS and a polyfluorene (PFO) active layer, the r-F8Ox significantly increased device efficiency as compared to PFO alone, both by acting as a second emissive layer and by improving charge balance in the device. An efficiency increase has also been demonstrated upon insertion of a similar r-F8Ox layer for LEDs based on F8BT [115]. The increase of the electroluminescence (EL) efficiency was attributed to r-F8Ox acting as an electron blocking layer because of a mismatch between electron affinity (EA) values (2.15 eV, versus 2.42 eV for F8BT). A similar effect also seen using MEH-PPV as the primary active layer [116].

To illustrate the applicability of the SNOL technique to materials using a variety of insolubilisation routes, regular, reproducible, periodic structures drawn in r-F8Ox are demonstrated. r-F8Ox structures were fabricated by blending the F8Ox polymer with the cationic photoacid initiator [4-[(2-hydroxytetradecyl)oxyl]-phenyl]phenyliodonium hexafluorantimonate, with 10% photoinitiator by weight. Films of this mixture were spun from a Tetrahydrofuran (THF) solution onto fused silica substrates. Under exposure to UV light, the initiator triggers development of the cross-linked network (Figure 4.20). Polymer that had not reacted was removed by rinsing in THF, following which the samples were annealed in the dark at 100°C for five minutes to allow the cross-linked network to fully develop. A detailed description of the synthesis and full characterisation of r-F8Ox and of the reticulation process has been given by Charas *et al* [112].

The films used with this material were thick (~240 nm), compared to those used in the conversion of PXT to PPV, in order to demonstrate patterning of higher material thicknesses sufficient for optoelectronic applications. Unlike PXT in air, re-solubilisation at high exposures is not observed, allowing much taller structures to be fabricated without the appearance of the semi-hollow cores described in section 4.1.5. It seems likely that this difference arises from the two-step insolubilisation process, in that only the photoacid becomes reactive upon UV exposure, not the polymer backbone. As such, excessive exposure may potentially damage the photoacid but is unlikely to lead to the development of reactive sites, or cleaves, along the main chain. Figure 4.20 presents a grid of pillar structures drawn in r-F8Ox with a periodicity of 1.3 µm, a lateral feature size of ~600 nm and aspect ratio of ~0.2 for the best resolved structures, array B.

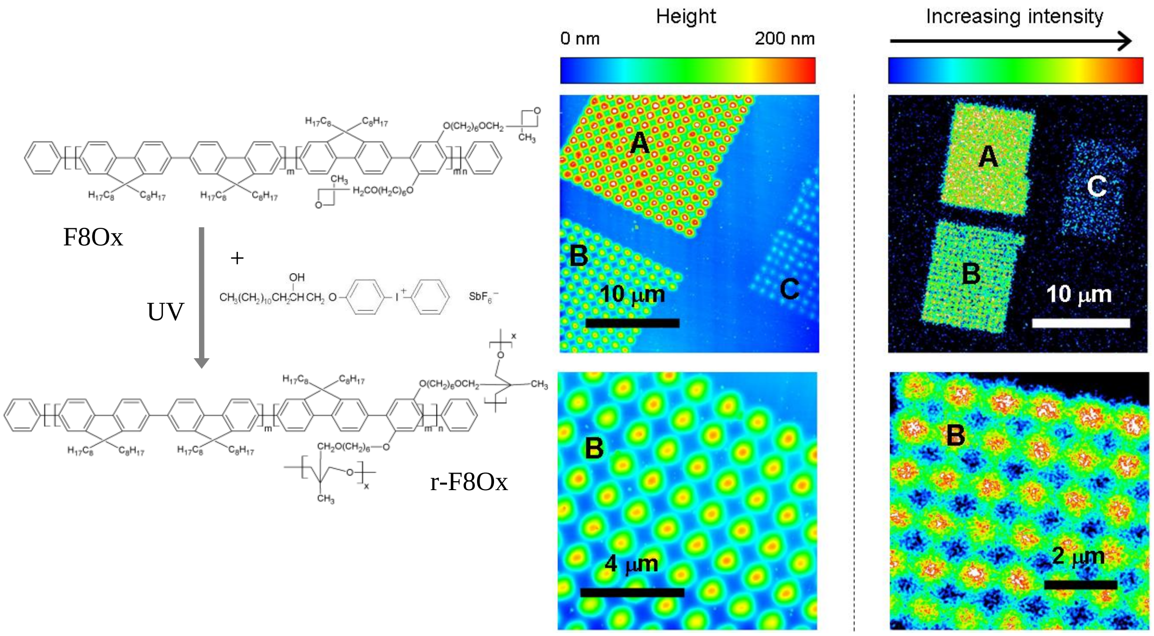

Figure 4.20: (left) schematic of the cross-linking reaction which occurs between the oxetane side-groups of F8Ox generating insoluble r-F8Ox under exposure to UV light. (middle) Tapping-mode AFM scans of several arrays of pillars defined in r-F8Ox from a ~200 nm film using a 60 nm probe aperture. Exposure decreases from A (200 ms) to B (50 ms) to C (20 ms) per point. (right) Confocal photoluminescence images of the same areas, with arbitrary intensity scale. The photoluminescence can be seen to originate from the r-F8Ox pillars, with the relative intensity correlated with pillar volume. Figure adapted from [111].

As expected, using thicker films limits the achievable resolution due to the larger illuminated volume which results from the increased tip-to-substrate distance. However, extrapolating from the previous modelling of feature formation in PPV (section 4.1), the dramatic increase in feature width seen would not necessarily be predicted. However, while the aperture, skin depth and refractive index are comparable between PXT and F8Ox samples, the simple linear relationship between field spread and film thickness is likely to be lost for such thick films. Furthermore, the conversion process for F8Ox also relies on mobile ions and side-chain diffusion to initiate cross linking, which allows the reticulated network to develop away from the initial excitation site. It has previously been shown that careful sequestering of the diffusing species is necessary to achieve high resolution using initiator-based insolubilisation [117].

To demonstrate that r-F8Ox remains functional after conversion, confocal photoluminescence measurements were taken of the resulting r-F8Ox structures by Dr Klaus Suhling at Kings College London. The system used to obtain fluorescence images consisted of an inverted microscope confocal system (Leica DM IRE2) with a x40 water immersion lens. The excitation source was a Ti:Sapphire laser at 760 nm. This is well outside the absorption band of r-F8Ox (405 nm is the upper limit), indicating that the fluorescence was excited by two-photon absorption. The corresponding images are presented in Figure 4.20, and show that all structures exhibit photoluminescence intensity correlated with the retention fraction of the film, as expected if the material is undamaged.

The next aim of this investigation was to establish whether a photoinitiator-driven insolubilisation process could achieve similar resolution to that of the on-chain insolubilisation seen in PXT-PPV. Figure 4.21 shows much smaller features in F8Ox, which have yet to be optimally developed. The exposure time of each 3 × 3 dot array has been varied from 30 to 300 ms across the sample. The core of converted material appears to be surrounded by streamers of (initially) unconverted material and an array of smaller droplets, either due to incomplete removal of unconverted material or diffusion of the photoinitiator. It is therefore hard to gauge the potential for higher resolution from these data, but taking the ‘core’ region as an estimate, around 80-100 nm FWHM has been achieved. This is in reasonable agreement with a shrinkage-free adapted critical core model presented previously, though in this case I have not investigated whether any significant shrinkage occurs.

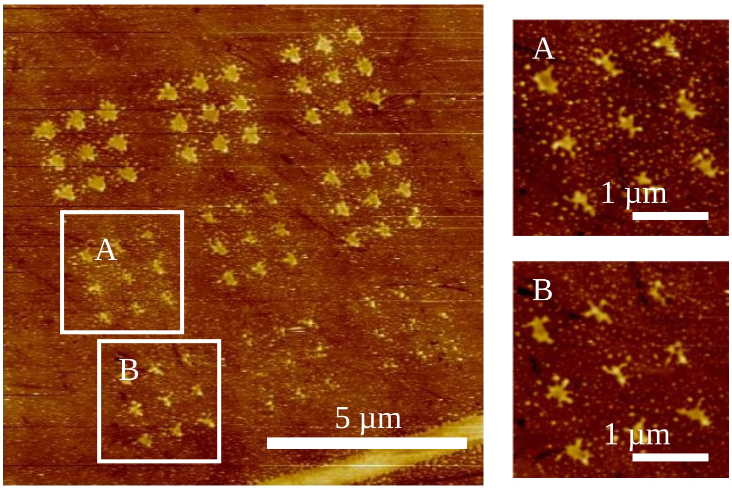

Figure 4.21: Tapping-mode AFM images of features drawn in r-F8Ox in clusters of 9, with each cluster corresponding to a different exposure time (300, 250, 210, 180, 150, 120, 90, 60, 30 ms bottom right to top left in a figure “2”) drawn with an OD2.0 filter placed in the beam path. Features are of order 10-15 nm high. Vertical range 30 nm.

These data demonstrate that the method of photoacid-initiated structure formation does not lead to mass loss upon overexposure. Figure 4.22 below shows a set of overexposed structures in r-F8Ox (drawn identically to those above except for a threefold increase in laser intensity). The topographic image shows no evidence of hollowing or resolubilisation at the centre of the overexposed features, which simply increase in size in step with the exposure dose. In addition, while there is significant phase contrast between the r-F8Ox and the underlying substrate, indicating a change in material properties, the phase is constant across the features themselves, indicating that there is little variation in composition.

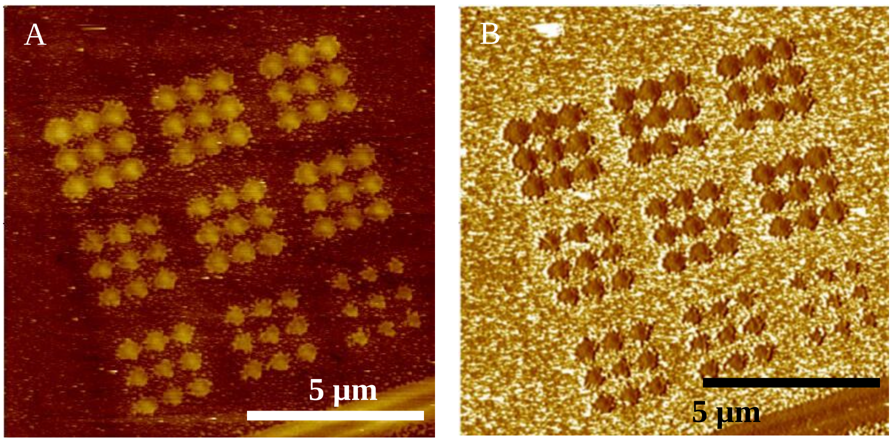

Figure 4.22: Tapping-mode AFM topography (A) and phase (B) images of features drawn in r-F8Ox, each 3 × 3 cluster corresponding to a different exposure time ((times as in Figure 4.21) with an OD1.5 filter placed in the beam path. Initial film thickness was approximately 20nm, and the resulting features are of order 10-15 nm high. Phase range ±20°. Vertical range 30 nm.

4.3. Lithography of BTOx

Continuing from the work of the previous section, lithographic patterning of a second oxetane-functionalised polymer BTOx has been investigated. This material is based around the green-emitting copolymer poly(9,9'-dioctylfluorene-co-benzothiadiazole), F8BT, commonly used in polymer LEDs [118]. Single-layer BTOx LEDs have been demonstrated previously, with EL efficiencies of 0.18cd/A [112]

As with F8Ox, the polymer backbone of BTOx is functionalised with long oxetane side chains which, in the presence of a photoacid initiator, can cross-link to form an insoluble reticulated network (r-BTOx) [119]. r-BTOx structures were fabricated by mixing the BTOx copolymer with the cationic photoacid initiator described previously, using 10% photoinitiator by weight. Films of this mixture were spun from a THF solution onto fused silica substrates. Under exposure to UV light, the initiator triggers development of the cross-linked network (Figure 4.23). Un-reacted polymer was removed by rinsing in THF, following which the samples were annealed in the dark at 100°C for 5 minutes to allow the cross-linked network to fully develop.

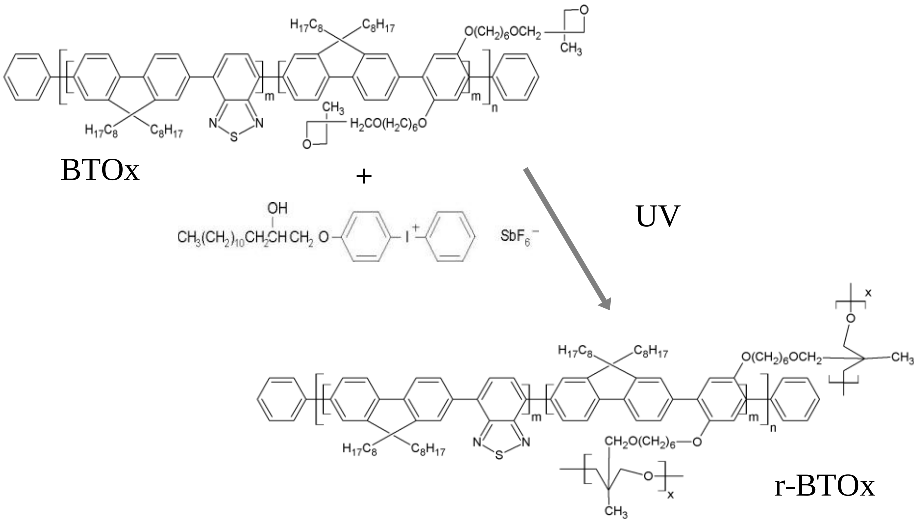

Figure 4.23: Reaction between BTOx and the photoinitiator, creating the reticulated r-BTOx network. In this investigation, m = n.

Figure 4.24 presents large (~200 nm high) structures drawn in r-BTOx with a periodicity of 1.2 µm and a lateral feature size of ~500nm, demonstrating the same ability as F8Ox to form large structures without photo-induced degradation. These structures are comparatively large due both to the thickness of the BTOx film and also possible diffusion of the photoinitiator, as above. It is also not anticipated that these features are optimally exposed. It may therefore be concluded that by an appropriate choice of insolubilisation system, in this case using a secondary sacrificial material to absorb the excitation, the photo-induced degradation observed for PXT/PPV can be avoided.

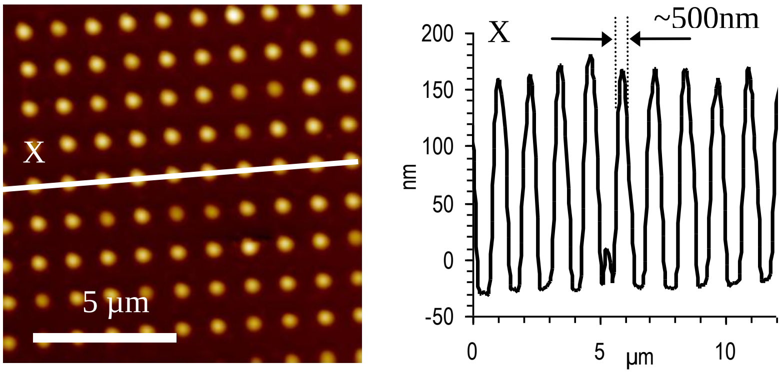

Figure 4.24: (left) Tapping-mode AFM scan of an array of pillars defined in r-BTOx from a 200 nm film using a 60 nm probe aperture, demonstrating the reproducibility achievable. (Right) Cross-section through the pillars, demonstrating typical feature size of around 500 nm FWHM.

4.4. Lithography HBC-acrylate

Thus far, I have investigated near-field lithography of conjugated polymers, because of their wide ranging application in optoelectronic devices (outlined in section 1.6.) However, aromatic π-electron systems are not limited to polymers, with significant work particularly in the last decade focussed on graphitic molecules and crystals. Examples include the two-dimensional planar material Graphene, described in detail by Geim and co-workers [120, 121] which shows significant promise as a high-mobility complement to, or substitute for, nano-scale Silicon transistors [122], as well as a basis for non-volatile memory using ferroelectric gating [123]. The more established nanotube graphitic phase has also been used in a variety of device applications, beginning with the first example of a single carbon nanotubes transistor operating at room temperature [124] and now expanding into a huge variety of electronics applications, particularly as a highly conductive transparent electrode for plastic electronics [125].

Highly aromatic and nano-graphitic small molecules based on polycyclic aromatic hydrocarbons, such as the acenes, coronenes and perylenes potentially offer some of the benefits of the highly-delocalised electron systems present in the graphitic family of materials while allowing for chemical modification of the material. Such modifications can include the introduction of solubilising groups, chromophores, cross linkable groups and other functionalising moieties. In particular, strong π-π interactions between molecules can lead to self-assembly of supramolecular structures, some examples of which are shown in section 6.1.2.

One such nano-graphitic molecule is hexa-*peri*-hexabenzocoronene (HBC), typically with apical functional groups, which can be used as a scaffold for so-called "click chemistry" [126]. In particular, the strong tendency of certain HBC derivatives to self assemble into large-scale tubular and whisker structures has been utilised to form high aspect-ratio graphitic nanofibres [127] and to allow the formation of radially di-block nanotubes with a graphitic conducting sheath, reproduced in Figure 4.25 [128].

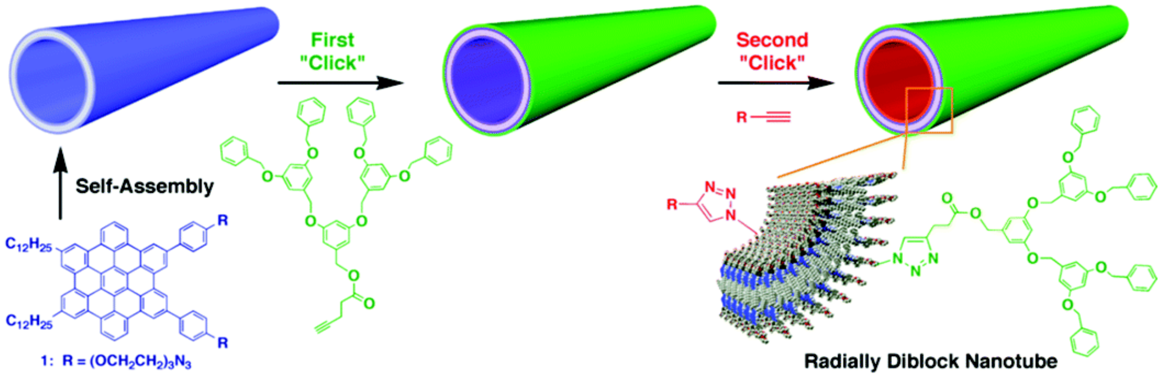

Figure 4.25: Reproduced from [128]. An amphiphilic HBC derivative self-assembles from a THF solution to form supramolecular nanotubes with dissimilar inner and outer surfaces. Click-functionalisation with a bulky macromolecule (green) takes place selectively on the outer surface, leaving the inner surface available for further click-functionalisation with a less bulky group (red) producing a radially di-block material.

While the self-assembling behaviour of HBC-derivatives is impressive, I am primarily concerned in this chapter with top-down assembly of pre-determined structures. A number of routes have been explored for selectively patterning HBC. Thermal polymerisation of HBC derivatives, functionalised with alkyl spacers containing acryloyl or methacryloyl moieties on the chain tips, has been demonstrated as a way of fixing a liquid-crystalline structure into a HBC film, over a range of temperatures at which it would normally be unstable [129]. A related approach demonstrated by Müllen and co-workers involves the functionalisation of HBC with acrylate units at the end of the alkyl spacers [130]. The polymerisation of these acrylate moieties can be initiated either thermally, as above, or via direct photoactivation. Using a mesoporous inorganic template, 200nm-wide tubules can be formed via *in-situ* thermal treatment. In addition, focussed synchrotron radiation directly on to the film allows micrometre-scale columnar structures to be defined after processing to remove unexposed material. These results suggest that it may be possible to pattern this material at higher resolution using a near-field light source. To investigate whether the previously achieved resolution could be improved using SNOL, films of HBC-acrylate (material provided by Dr Wojciech Pisula and Prof Klaus Müllen[*]) were spin-cast from THF at 2000rpm onto 15mm Spectrosil. The film thicknesses were not measured, but from the data below they appear to be 30-50 nm. The film was noted to be quite non-uniform when spun.

Photo-polymerisation was achieved using 325 nm illumination through the SNOL probe with ~50 nm aperture. Exposure doses were varied using neutral density filters inserted into the laser path, and by varying the exposure time per point using the electronic shutter. After exposure, the un-polymerised material was removed by rinsing the substrate in THF for 10 seconds. Preliminary observations under an optical microscope revealed that large numbers of particulates remained on the substrate, in addition to the intended structures, so a further 10 second rinse was used. This did not appear to have any effect on the particulates, some of which could be seen in the later AFM images. Optimal exposure was found to occur at high doses, consistent with the requirement for high-brilliance synchrotron exposure described in previous work. The best results were obtained using an unfiltered beam-path. Figure 4.26 gives an overview of the critically exposed region, where a transition from overexposure to underexposure is seen as exposure time is varied.

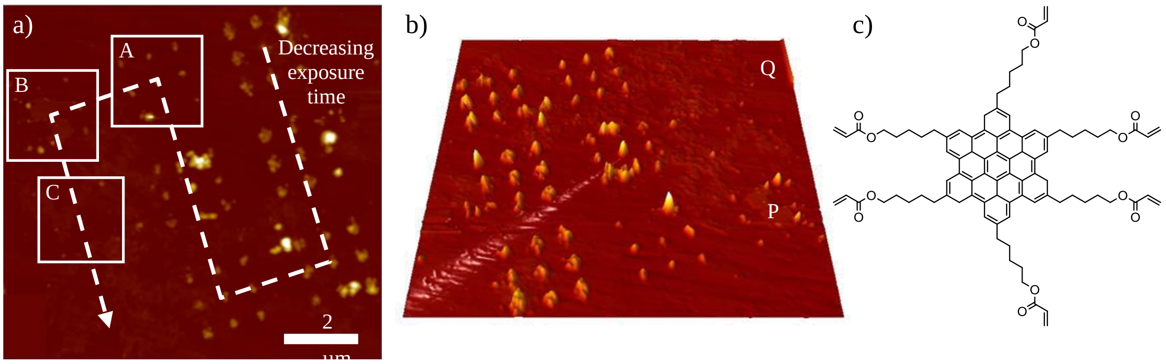

Figure 4.26: a) 10.4 µm tapping-mode AFM scan of the best resolved HBC structures obtained using no ND filters. The largest of the debris (>200 nm height) have been digitally removed. Vertical range is 180 nm. Regions A, B and C were exposed for 120 ms, 90 ms and 60 ms per point, respectively. b) 3D plot of the same region highlighting region P, where the largest debris was present (400 nm high) and region Q where a reference structure has been similarly removed. c) Structure of HBC-acrylate.

---

[*] Max Planck Institute for Polymer Research, Mainz, Germany

Figure 4.27, Figure 4.28 and Figure 4.29 show zoomed-in regions from this image and cross-sections through typical features. As expected, the typical feature size drops with exposure time, and here a minimum repeatable resolution of ~95 nm FWHM is achieved, with some poorly developed features in Figure 4.28 and Figure 4.29 somewhat smaller than this (60-70nm). Unfortunately, it cannot be established on the basis of these measurements which crystal phase of HBC has been generated in the structures, or whether the HBC molecules remain functional after the UV treatment, which would be a logical extension of this work. Nevertheless, the < 100 nm minimum feature size is a significant improvement of that demonstrated previously, and is again consistent with a shrinkage-free critical-core interpretation of feature formation. However, the smaller features observed again illustrate one of the limitations of this approach, in that sub-critical features which nevertheless anchor to the substrate are hard to describe quantitatively.

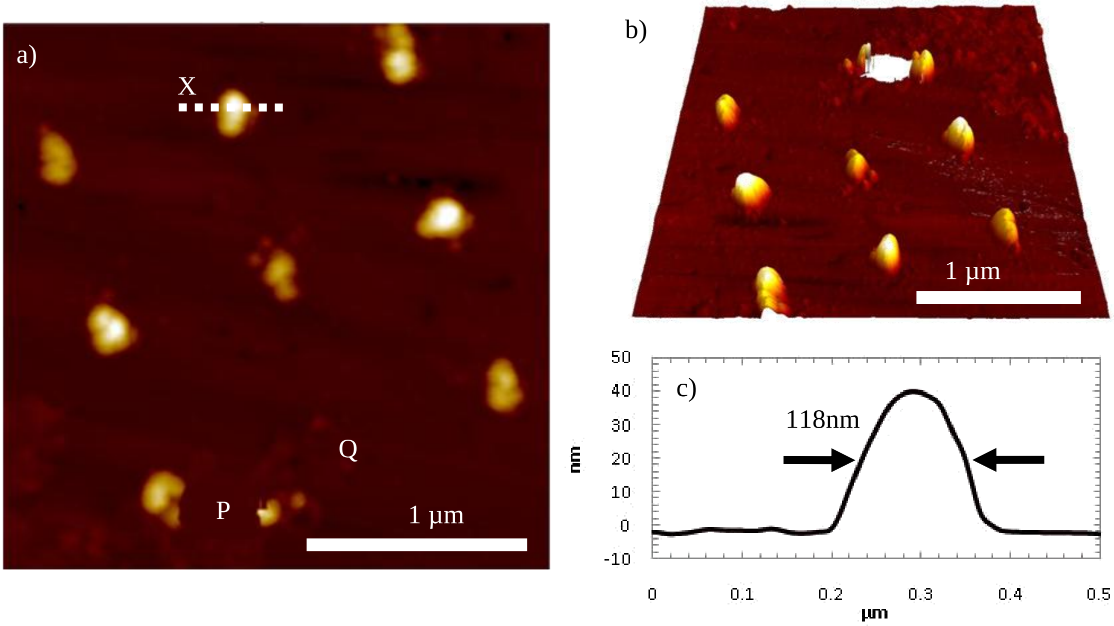

Figure 4.27: a) 2.5 µm scan of region A in Figure 4.26 (120 ms). Vertical range is 45 nm. A large ~120 nm high particle has been digitally removed from point P, which appears to have destroyed the structure expected at point Q. b) 3D representation of the same region highlighting residual material on surface. Cross-section X c) shows typical feature size of ~120 nm FWHM.

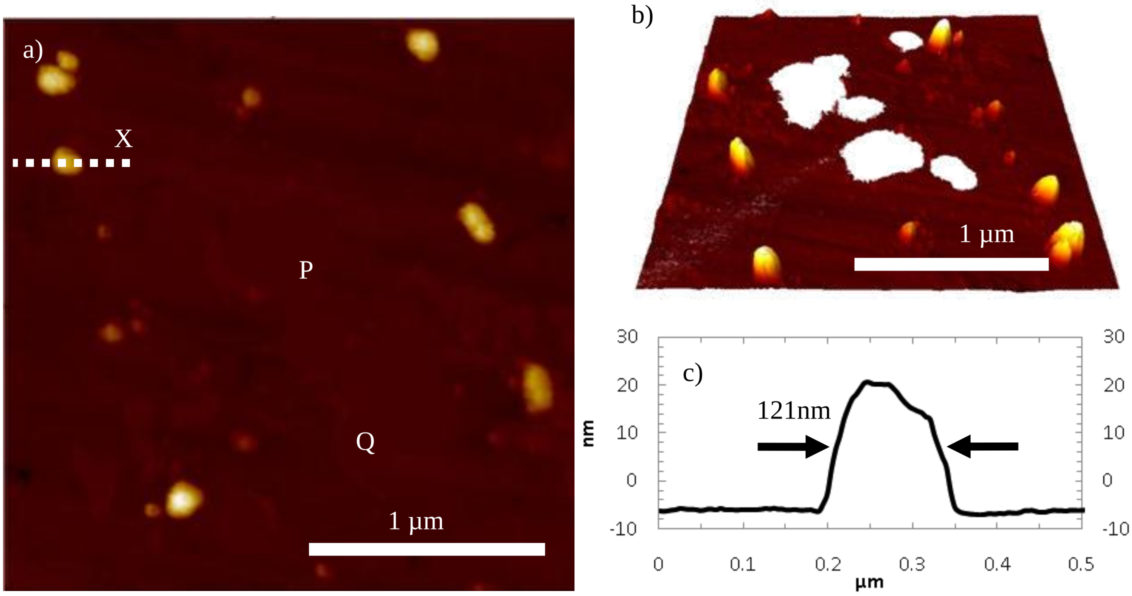

Figure 4.28: a) 2.48 µm scan of region B in Figure 4.26 (90 ms). Vertical range is 42 nm. A collection of large debris particles (>200 nm high) have been digitally removed from the image, which obscure the intended structures at P and Q. b) 3D representation of the same region highlighting residual material on surface. Cross-section X c) shows typical feature size of ~120 nm FWHM.

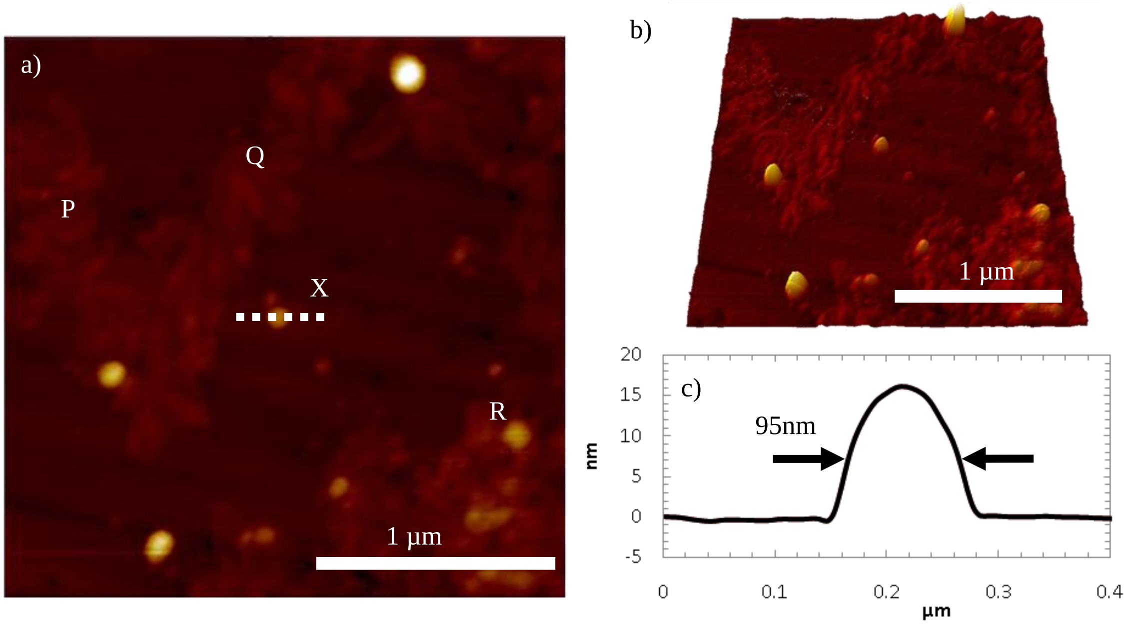

Figure 4.29: 2.36 µm scan of region C in Figure 4.26 (60 ms). Vertical range is 40 nm. Intended structures at points P and Q appear to be missing. The region has areas of residual debris, but it is unclear if this debris can explain the failed attachment of the structures given that structure R, within the debris, is retained. b) 3D representation of the same region highlighting residual material on surface. Cross-section X c) shows minimum feature size of 95 nm FWHM.

4.5. *In-situ* lithography of PMMA-azobenzene

While the physical dimensions of the near-field probe and aperture may be learned using SEM, or similar, and far-field observations of the throughput are useful for gauging aperture quality, direct measurement of the extent of near-field confinement near to the tip compared to far-field effects is itself inherently a near-field experiment. In principle therefore, it is possible to infer the field shape by observing the resulting lithographic patterns it produces. However, all of the lithography presented thus far has required a development step, whereby the sample must be taken out of the SNOL system for the removal of soluble portions of the film. As has been demonstrated in earlier sections, this adds unwanted noise and complexity which cannot be easily corrected for. To address this particular problem, one route is to identify a system which reacts upon exposure to the near field source in such a way that changes in the morphology or chemistry of the sample are identifiable *in-situ*, either through an optical or topographic probe.

It was demonstrated in 1972 that the isomerisation of azobenzene sub-units attached to the backbone of a wide variety of common polymers could be studied in the solid state. This sub-unit has three isomerisation processes – an optical transition from trans to cis, a related optical transition from cis to trans, and a thermal relaxation from cis to trans because of the inherently higher stability of the trans state due to steric interactions between the benzene groups [131]. Schematics of these transitions for a particular poly(methyl methacrylate) (PMMA) backbone and azobenzene sub-unit are shown in Figure 4.30.

The absorption of the cis isomers is altered slightly with respect to the trans, but the overlap between the two is sufficient that a single-wavelength source can be used excite both. Under continuous illumination, the motion of the azobenzene chromophores leads to apparent photo-fluidic behaviour in the host polymer [132]. The migration and rearrangement of the host polymer chain is believed to occur by reptation, but the exact mechanism is not fully understood. Reports have previously shown both photo-induced diffusional motion well below the material’s glass transition temperature in the presence of plane-polarised light [133], and a lack of such motion under similar conditions in amorphous films under circular polarisation.

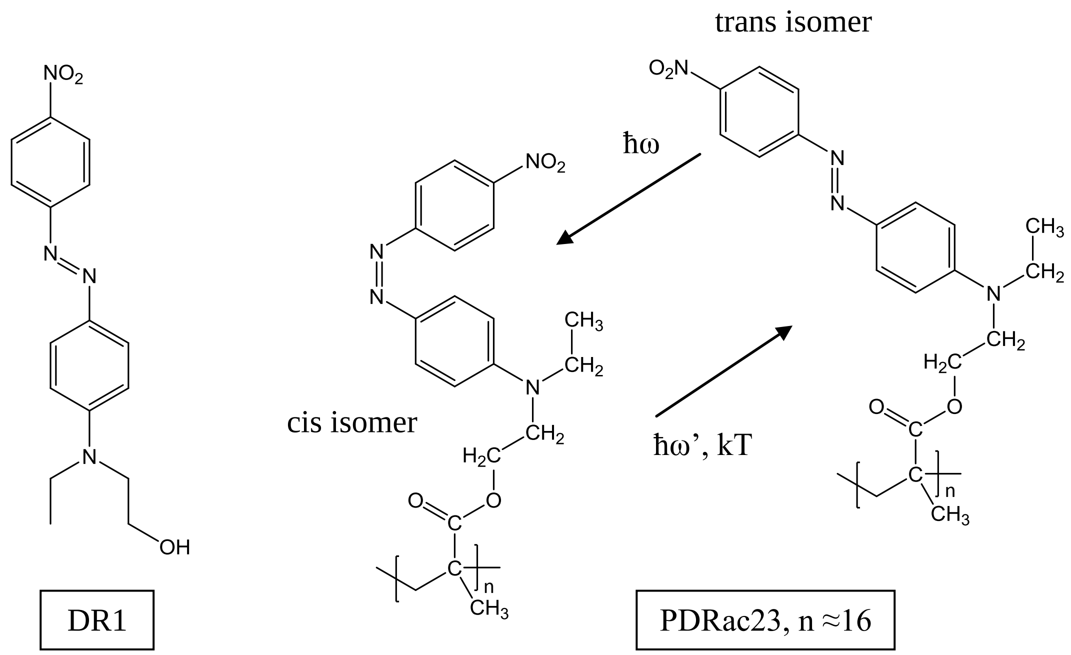

Figure 4.30: Schematic of the stable trans and metastable cis isomers of DR1 azobenzene chromophores decorating the PMMA backbone of PDRac23.

It is likely however that excitation of the alternating cis-trans isomerisation generates simultaneous softening of the host material, reported in several instances, and localised stresses within the matrix which can lead to deformation and, in some cases, plasticisation and flow. When using polarised light, the resulting film is birefringent, since a preferred chain orientation is induced as chromophores realign until perpendicular to the polarisation vector. The particularly high strength of this effect for the azobenzene system was first demonstrated for the azo-dye methyl orange in a PVA matrix [134], and later studies have investigated similar behaviour in other chromophores [135]. Changes in structure induced by the isomerisation are typically reversible - holding the host material above its glass transition temperature, or exposing the material to unpolarised or circularly-polarised light has been shown to return samples to their original amorphous state, with relaxation times ranging from seconds [136] to many hours [95, 133], depending on the nature of the backbone material and the technique applied.

Selective illumination has been shown to lead to micro-scale topographic patterning of the film, on the micro-scale in the case of holographically induced surface relief gratings in PMMA-azobenzene [133, 137] and azo-silica gels [138], for example.

Illumination can also lead to local changes in material behaviour, such as changes in surface potential [139], without necessarily greatly altering topography.

Investigations of the effect of nano-scale illumination are widespread, with many focussed on polymers decorated with the Disperse-Red-1 (DR1) azobenzene chromophore (Figure 4.30). Near-field patterning of azobenzene-functionalised thin films has demonstrated sensitivity to field shape and strength, with both positive and negative structures achievable depending on illumination intensity [94, 140]. Other have specifically investigated the use of this development-free lithography to characterise both the near-field and far-field near to hollow [141] and apertureless [93] tips, again showing strong polarisation- and intensity-dependence, particularly for apertureless configurations.

One outcome of these investigations is that azobenzene-functionalised films have been considered as candidates for high-density, persistent digital memory using variously electrical [142], optical [143] and topographical [95] methods to write to the film. Information densities of 0.4 Gb/cm^2 have been demonstrated, though typically long erase times may restrict this approach to use in write-once technologies analogous to CDs and DVDs.

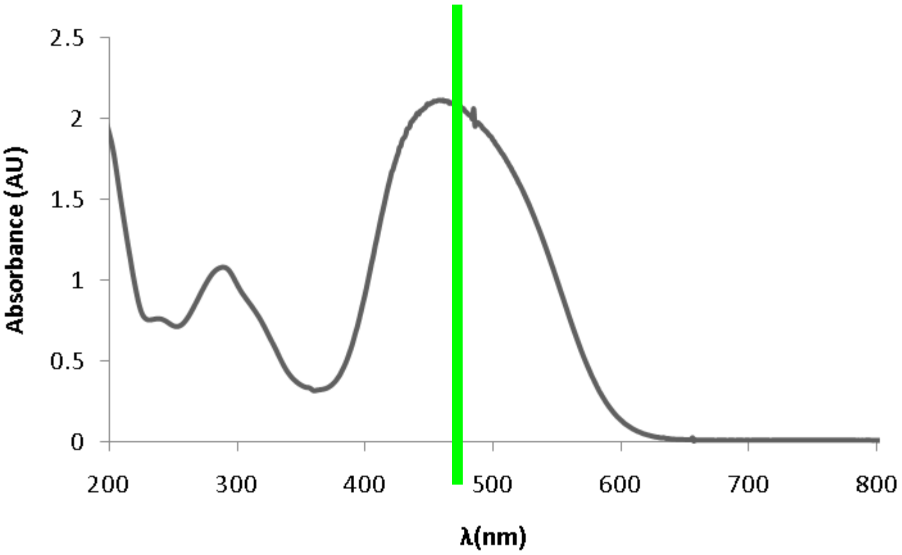

Figure 4.31: Absorbance of PMMA-Azobenzene thin film, demonstrating broad peak corresponding to cis-trans transition. Green line shows position of laser excitation at 488 nm.

In this investigation, the use of an azobenzene functionalised polymer as a means of characterising the shape of field around the near-field probe was examined. The examples presented here utilise thin films of the low molecular weight (~6600g/mol)

PMMA-Azobenzene PDRac23, supplied by Dr Burkhard Schulz[*] prepared by spin-casting from a 2% by weight chlorobenzene solution onto quartz substrates. For this material, the trans-cis transition exhibits a broad peak around 450-500nm, shown in Figure 4.31, which was excited using an Argon-ion laser operating at 488 nm. To establish if this material would respond to optical excitation in a similar way to other azobenzene-functionalised polymers, an *in-situ* patterning test was conducted by first imaging a 2 µm strip of the film using the SNOL system in topographic mode (as a shear-force AFM). It can be seen both that the area is flat, with a typical variation in height of order 1nm. This is likely due to a combination of noise in the measurement system and the true surface roughness. It can also be seen that repeated scans over the surface do not show any damage being caused to the film or to the tip. 488 nm laser illumination was introduced via the SNOL tip, and a single vertical pass across the sample was conducted. After completion of the pass, a second topographic scan of the same area was taken, with the laser off. The resulting images are shown in Figure 4.32.

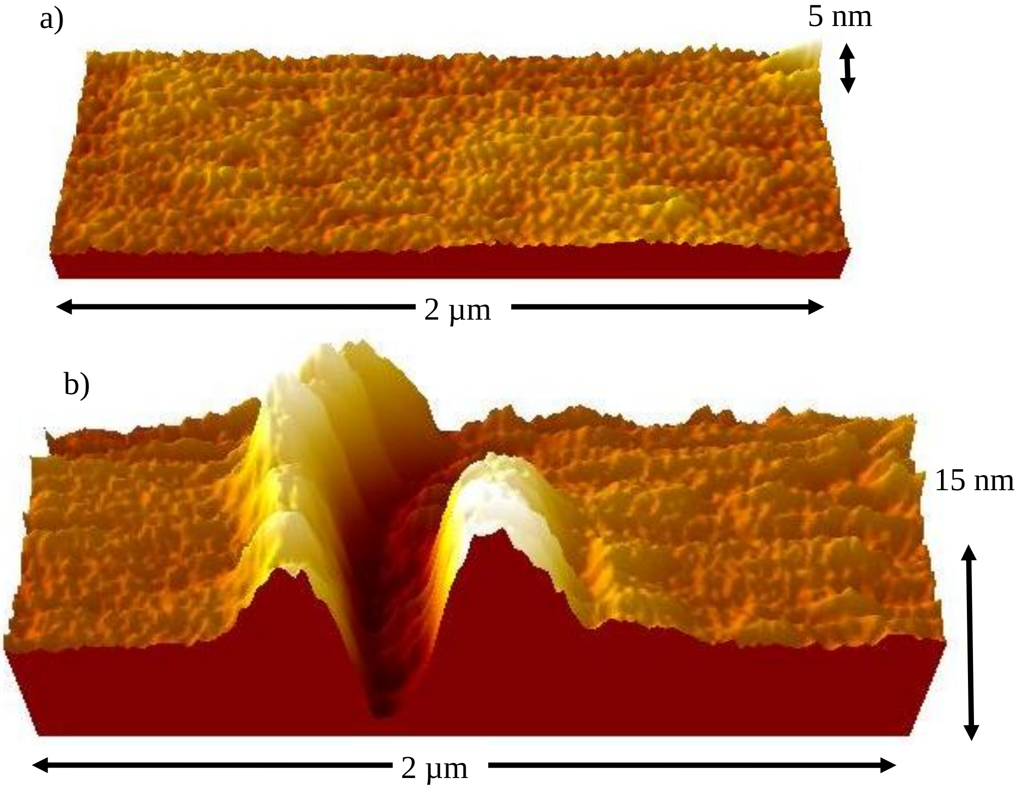

Figure 4.32: a) Shear-force AFM image of the region of film to be patterned. b) Shear-force AFM image of the region after patterning with a single vertical line. The start of the line exhibits a slight curvature, which is likely due to a small amount of drift in the piezoelectric positioning system as it begins to scan.

---

[*] Institute of Physics, University of Potsdam, Potsdam, Germany

It can be seen that the illumination caused apparent transport and deformation within the polymer film, confirming that direct patterning and topographic read-back are possible for this material. The trench feature drawn here has a depth of approximately 5 nm and a width of 150 nm, with approximately 200 nm wide, 5 nm high ridges formed on either side. The nature of the structure tentatively suggests that mass transport under these conditions occurs by photo-induced diffusion of material away from a region of high field intensity, but is by no means conclusive, particularly since neither the laser polarisation nor the integrity of the probe are known. Previous reports have demonstrated the somewhat contradictory findings that illumination can cause the host material to migrate either down or up a local field gradient. There has also been the suggestion that the local softening of the material caused by the high field strength at a near-field tip can be sufficient to allow the tip to pick up and deform parts of the film as if it were fluid. Nevertheless, these images also illustrate the particular versatility of the SNOL system for conducting this kind of *in-situ* optical and topographic measurement.

To eliminate the possibility that this structure was caused by mechanical scratching between the probe and the sample, a series of experiments were conducted holding the SNOL probe stationary while illuminating the sample, then scanning the resulting topography with the laser turned off. Thin films of PDRac23 polymer were spun from chlorobenzene as before. Using tapping-mode AFM the film thickness was measured as approximately 70 nm.

The SNOL tip was held at a series of pre-programmed points in a 3x3 grid, in close contact with the film, with each point receiving illumination at 488 nm for a specific time with an OD0.5 filter inserted into the beam path. Illumination time was varied exponentially from point to point. While the polarisation orientation of the laser before launching into the optical fibre leading to the probe is known, the final polarisation depends on the length and shape of the fibre and varies between experiments. After illumination, the laser was turned off and the SNOL probe used to measure the topography. Figure 4.33 presents the resulting images after illumination through both a new, undamaged, probe and an old, damaged probe. The nature of damage suffered by near field probes under prolonged scanning and illumination has been investigated by Ambrosio and co-workers, who observed a degradation of the metal cladding around the aperture [144]. While they did not find this correlated with a loss of field confinement during their investigations, after prolonged usage it seems likely that such a loss of confinement will eventually occur.

From the figures below, a number of observations may be made. The undamaged probe generates a highly structured pattern, with a strong orientation preserved from point to point. A central, high, feature is produced, which is associated with the expected position of the near-field. This is surrounded by two sunken lobes and edge-ridges, which grow slowly with exposure time. The damaged probe produces a much larger, more symmetric pattern with no central feature. In addition, low-amplitude interference fringes can be seen around the main features (period approximately 400nm). Both of these observations imply that a strong near-field component is no longer present for the damaged probe, or that it is comparable in strength to the far-field. In both cases, large-scale deformation can be seen, consistent with the migration of polymer chains within the illuminated region rather than mechanical deformation.

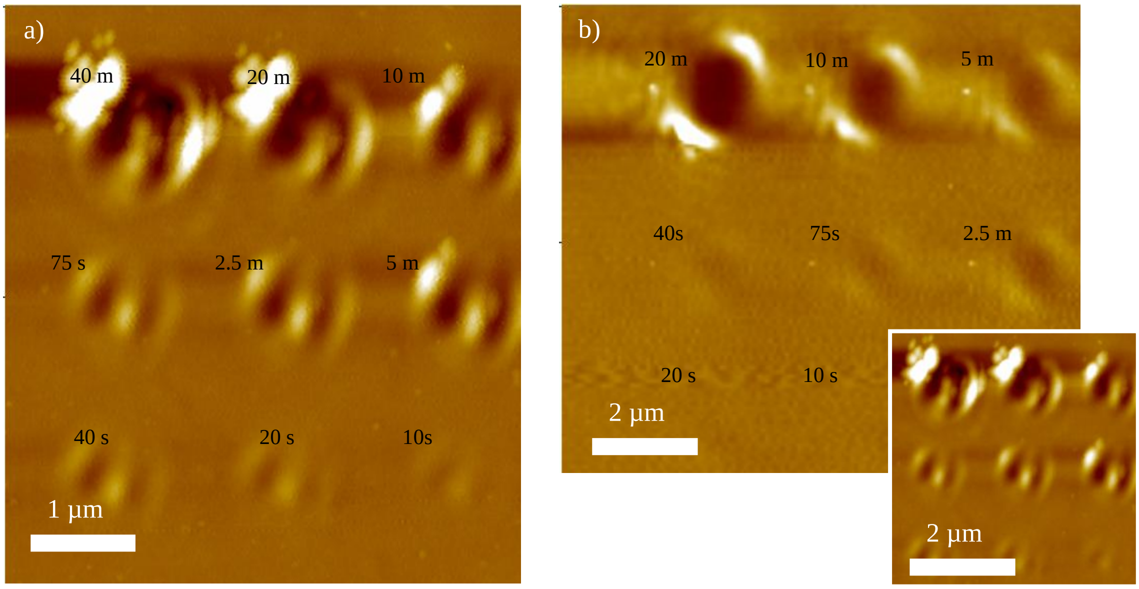

Figure 4.33: Shear-force AFM images of PMMA-azobenzene films measured after 3 × 3 point-wise illumination at 488 nm with a OD0.5 filter placed in the beam path for the times (in minutes/seconds) shown. a) 5 × 5 µm image using a new probe, vertical range 65 nm. b) 10 × 10 µm image using an old, damaged probe, vertical range 65 nm. Inset shows image a) drawn to the same scale as image b).

To establish whether structure formation is an intensity dependent process, or simply dosage dependent, point-wise illumination of a PMMA-azobenzene film was conducted during which intensity varied while total exposure dose was kept constant by changing the exposure time per point. The probe in this case was newly mounted. The resulting structures are shown in Figure 4.34a). The depth and extent of the structures, particularly the central feature, scales both with total illumination dose and also with intensity at fixed dose, indicating that the migration of the polymer chains is a non-linear process and occurs disproportionately quickly in the presence of stronger field gradients. As in Figure 4.33a), the features are highly structured.

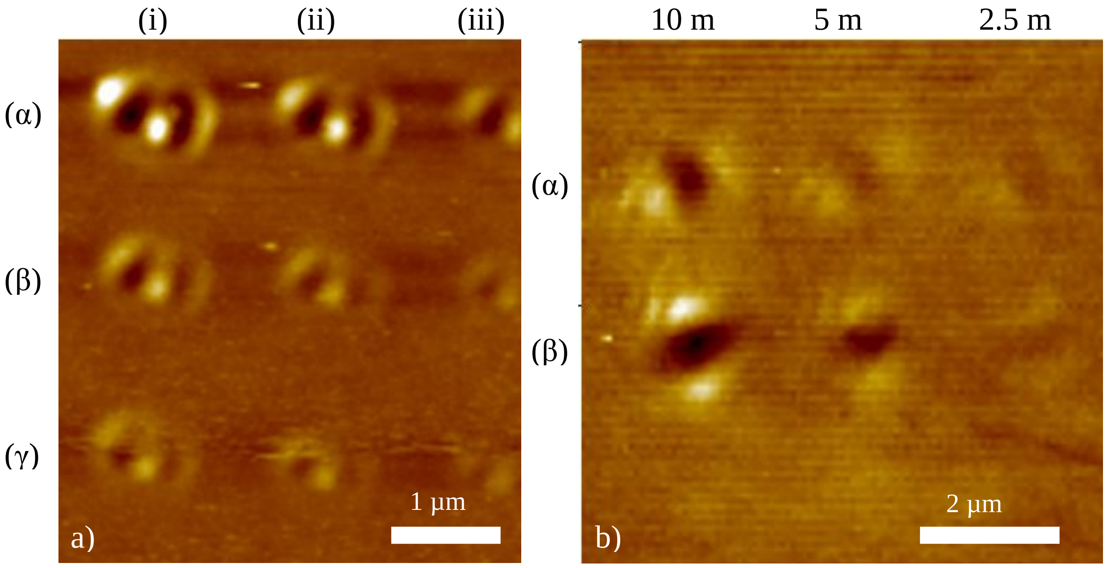

Figure 4.34: Shear-force AFM images of PMMA-azobenzene films after a) point-wise illumination at 488 nm. Intensities as a fraction of unfiltered intensity are (α) 30%, (β) 10%, (γ) 3%. Total illumination dose per point (arbitrary scale) is (i) 100%, (ii) 50%, (iii) 25%, vertical range 30 nm. b) Point-wise illumination at 488 nm for the times shown, with polarisation rotated by 90° between rows (α) and (β), vertical range 15 nm.

In making the various assertions above, the structure motifs are assumed to be determined primarily by the field profile generated by polarised light incident on the probe tip and near-field aperture. By doing so, it is implicitly required both that the detailed structure of the probe tip and aperture has only a secondary effect on the field profile, and that the incident light is indeed polarised. That this latter point is correct is not necessarily obvious, since the optical fibres used were not specifically designed to be polarisation maintaining, and it is known that probe structure can impose a dominant polarisation on the transmitted field [145].

To establish whether the structures observed are controlled by laser polarisation or by aperture/probe asymmetry, two lines of points were illuminated sequentially at 488 nm though a partially worn probe. Between lines, a half-wave plate and secondary polariser were used to rotate the launch polarisation by 90°. Relative intensity was maintained by choosing two polarisations at ±45° to the original laser polarisation. The results of this scan are shown in Figure 4.34b) It can be seen that while the relative illumination intensity changes slightly between lines, perhaps indicating preferential transmission by the probe or optics, the entire structure motif rotates by 90°. This is consistent with polarisation being largely maintained through to the aperture, and with the structure asymmetry being determined by polarisation, rather than probe/aperture asymmetry.

From the above observations, the response of the azobenzene-functionalised host chain to the presence of the field may be understood. Where the field is low in intensity, as is the case for the rapid (line) scan shown in Figure 4.32, the broken/worn probe images in Figure 4.33b) and Figure 4.34b), and the regions away from the central peak in Figure 4.33a) and Figure 4.34a) the polymer migrates down the field gradient, with strong polarisation-driven asymmetry. This in turn leaves depressions in the film and ridges of accumulated material at the edges. The central peak only forms where a tight near-field component of the field exists, with very high intensity and high gradient. An identical transition from low to high intensity/gradient is seen by Davy *et al* [141]. Similar positive topography is seen by H'Dhili *et al* in the region of enhanced field under an apertureless probe, transitioning to a far-field interference regime consistent with positive topography being associated with regions of destructive interference [93]. Importantly, the latter study rules out the possibility that the central topographic peak forms as a result of either mechanical contact or heating of the sample.

It is therefore clear that distinctly different behaviours are encountered when moving from high field to low field. While much of the modelling literature regarding azobenzene-functionalised polymers deals primarily with the formation of surface relief gratings, where fields strengths are typically low, a number of studies have extended to point-like or Gaussian illumination. In particular, Bublitz *et al* successfully predict the trend seen above [146], which is reproduced below (Figure 4.35). They calculate the motion of an initially isotropic population of chromophores attached to their host chains when exposed to a Gaussian-profile beam of linearly polarised light. The final topography arises by considering the combined effects of film elasticity, chain migration and chain realignment (which eventually turns off motion). Their low intensity Gaussian-beam simulation accurately reproduces the features observed in all images, barring the central peak, and explains the reorientation of the structures upon a change in polarisation direction. The simulations also suggest that the dominant polarisation orientations in each of the images above are perpendicular to the line bisecting the two main edge-features. Finally, a central peak is reproduced for high intensity illumination due to a saturation of the chain out-migration at high field intensity which leads to net back-migration from the low intensity regions to the high intensity core. While the physical origin of this saturation effect is not clear, in these simulations it arises from interplay between 1) decreasing motion in the high field region as side-chains align with the local field vector and 2) increased motion near to this region leading to a net migration inwards.

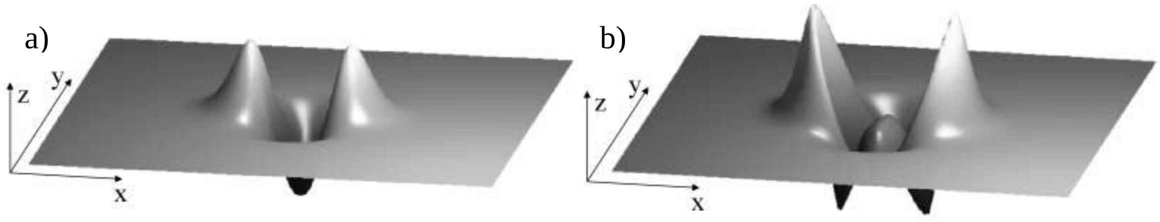

Figure 4.35: Reproduced from [146]. Calculated surface deformations caused by exposure to a single beam linearly polarized in the *y*-direction and with a Gaussian intensity distribution. The intensity of b) is 10 times higher that of a).

Since the laser power launched into the probe is comparable for all the images above (except where explicitly varied), the formation of the central peak cannot be attributed to significant changes in average field intensity. Instead, since the high central feature is present only when relatively new and undamaged probes are used, it may be concluded that this feature is a manifestation of a high-field region which only results from a good quality sub-wavelength aperture. It may therefore be surmised that the typical field profile originating from the SNOM probes, as captured by the PMMA-azobenzene films, consists of two parts. The first is a polarised, low-intensity, far-field spot of a similar size to the probe tip (~1 µm) which likely arises from light leakage through the probe coating. The second is the (likely-polarised) near-field from the probe aperture, the confinement and intensity of which depend on the quality of the aperture. For a good quality aperture, the intensity is sufficient to initiate back-migration to the central region, whereas for a damaged aperture the effect is only to supplement the slow out-migration caused by the far-field illumination. The superposition of the two leads to the structures seen. If this interpretation is correct, it in turn provides a method for *in-situ* testing of aperture quality without retrospectively measuring the physical profile of the probe - a necessarily destructive technique. The probe quality can be determined by considering the relative size and contrast of the central saturation-induced peak, as compared to the surrounding far-field structuring.

Furthermore, the qualitative observation may be made that the intensity close to a good-quality sub-wavelength aperture, as indicated by the presence of the central peak, is significantly greater than the far field component incident on the surrounding film. This is consistent with the lithography results shown in previous sections, in that for near-field doses sufficient to insolubilise the structures presented, no significant far-field contribution to the patterning process is observed.

What has not been achieved in this study is a detailed mapping of the near-field itself, to test the field shape predicted from the Bethe-Bouwkamp model. For this to be achieved, significantly higher topographic resolution is needed, which requires the transfer of samples to a higher-resolution microscope. The lack of optical contrast, and small dimensions, of the PMMA-azobenzene structures meant that attempts to locate them using a high-resolution AFM were not successful in this investigation.

4.6. Conclusions

In summary, I have demonstrated how SNOL can be used to pattern functional polymers with high resolution, limited primarily by the aperture size, and reproduced over length-scales of many microns to arbitrarily complex designs. In addition, a large improvement in resolution and complexity over previous work has been demonstrated for the important and widely used polymer PPV, insolubilised using a precursor route. Structures have also been demonstrated using a variety of insolubilisation routes in the electroluminescent polymers F8Ox and BTOx, and the small molecule HBC-acrylate.

This opens the route for the development of active nano-scale devices fabricated using this technique, with the reproducibility and complexity demonstrated offering the prospect of application to nano-electro-mechanical systems, nano-optical switches, and more generally nano-photonics and possibly plasmonic applications. In combination with parallelised near-field instruments, such as the so-called SNOMIPEDE at the University of Sheffield (UK) [147], this technology may become of significant interest for a number of applications and not only as a prototyping tool.

Significant progress has also been made in understanding the fundamental processes determining the formation of structures using this precursor route, and demonstrating experimentally the effects of polymer degradation, film thickness and substrate material. Progress has also been made in understanding the nature of the wider-scale field profile around the SNOL probe, and how relative strength of the near-field changes as probes age. Finally, to further demonstrate the versatility of the SNOL system, not to mention a little light relief, see Figure 4.36.

Figure 4.36: Sample ppvD67, possibly the smallest Mona Lisa in the world! Fabricated from PPV, the detail is missing due to overexposure and the fast shutter switching burned out the shutter controller at point A discouraging further attempts, but the smile is still there. Inset shows the monochrome bitmap used for the patterning.

5. Scanning thermal lithography

As outlined in section 1.7, a wide variety of techniques for patterning conjugated polymers have been explored. The focus of patterning techniques has primarily been directed towards direct radiative patterning (optical far- or near-field, electron beam), or indirect patterning via a soft lithography technique (though the original patterning of the template is often radiative). Direct patterning (either topographic or chemical) using a thermal source is an example of a direct, non-radiative technique which has been described by a number of authors [59, 148-151]. Two general methods may be employed to achieve thermally-activated lithography of a material. The first is to use a heated stamp to convert a film of material in a pre-defined pattern, in a manner analogous to “parallel” contact printing/contact mask techniques, and using similar technology. The second is to use a local probe, heated to an appropriate temperature, to scan over and serially convert selected regions of a sample, analogous to the scanning near-field lithography described in the last section. It is this latter route which will be considered further.

As a possible advantage in taking the approach of a local thermal probe, many of the photo-patternable materials described in section 4 (particularly PXT) and many commercial photoresists can also be patterned thermally [152], without necessarily encountering the complications of near-field patterning described in sections 4.1 and 4.5. In fact, for nano-scale patterning, the fundamental limit to how small an area can be heated is given by the sharpness of the probe tip: no thermal equivalent to the diffraction limit exists. Despite these promising attributes, thermal and thermochemical lithography has received relatively little attention compared to other approaches to nanolithography. This is likely due to the contacting nature of the technique, which for large-scale production may lead to issues of probe (or template) contamination. However, as has already been outlined, improving the resolution of non-destructive patterning techniques to the length-scales required for modern nano-electronics increasingly requires that close or intimate contact be made with the sample to be patterned. Creating a system capable of undertaking local thermal lithography is relatively straightforward; in the same way that a near-field microscope can be modified to conduct optical lithography, so scanning-thermal microscopes [153] can be used to conduct local thermochemical manipulation, which is the approach taken below. To do so, I return to the well-studied PXT/PPV system. In all cases, samples were prepared by spin-coating of the PXT precursor polymer solution (0.25% by weight in water) on to fused silica substrates before local thermal conversion. Samples were developed by rinsing in methanol for 10–15 s to remove the unheated precursor. Full conversion to conjugated PPV was achieved by baking in a vacuum oven at 220 °C for 3-5 hours.

5.1. Lithography using a micro-thermal probe

5.1.1. Instrumentation

Initial investigations of the patterning potential of thermal lithography were conducted using a Wollaston Wire probe, typically used for microthermal analysis [154]. The Wollaston wire comprises a 75 µm-diameter silver wire surrounding a 5 µm-diameter platinum–rhodium core. A 50 µm section of the core of the wire is exposed and bent into a “V”, the tip of which forms the probe. When a current is passed through the wire this narrow exposed section provides a resistive barrier, such that power is dissipated preferentially at the probe tip, causing it to heat. A schematic of the probe setup is shown in Figure 5.1.

A mirror attached to the shaped Wollaston wire allows the probe to be mounted on a standard AFM with laser feedback. In this case, a Veeco Explorer AFM operating in contact mode was used to scan over the sample surface. The probe was maintained at a constant temperature (200-600°C) using an attached Microthermal Analysis Unit (TA Instruments). Local thermal analysis measurements indicate that a probe temperature above 180°C was needed to initiate conversion of the PXT, with a maximum probe temperature determined by the scanning rate and the acceptable level of viscous deformation of the sample. Deformation under a static probe occurred above approximately 415°C, whereas deformation under a rapidly moving probe (100 µms^{-1} in this case) can be limited to a few nm even at 600°C. The force between the probe and the sample was kept at the minimum necessary to maintain contact with the sample, to reduce contact area (see section 5.1.3). A full report of the lithography achieved using this microthermal probe is given in [52], from which the figures below have been adapted.

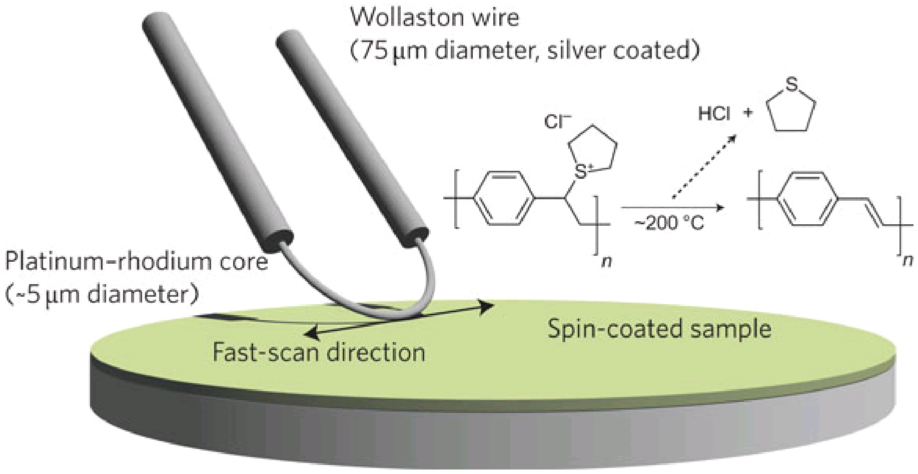

Figure 5.1: Schematic of the Wollaston wire probe, reproduced from [52], showing the orientation of the exposed core with respect to the sample. The mirror used for laser feedback is mounted above the first section of silver coating shown her. Inset shows the thermal conversion route of the precursor polymer PXT to insoluble PPV, an equivalent process to that described in section 4.1 using UV exposure.

5.1.2. Lithography

Using the above setup, a variety of structures were patterned in PPV thin films, including regular grids and isolated lines. Confocal photoluminescence images obtained of the structures drawn show that the PPV remains emissive after conversion. By fixing the probe temperature and optimising the scanning speed of the probe, features ranging in size from several hundred nanometres down to a minimum of 28 nm were fabricated; examples are shown in Figure 5.2. The width of the lines was found to decreases rapidly with increasing scan speed, varying from heavily over-exposed at slow scan speeds to optimum resolutions at higher speeds. The faster scan speeds produced features lower in height, owing to reduced conversion ratios. Of particular note is the fact that both fine features and large areas (100 × 100 μm^2) could be patterned quickly and reproducibly using this technique, a task which has been shown to be feasible, but very time consuming, using SNOL (section 4.1.7).

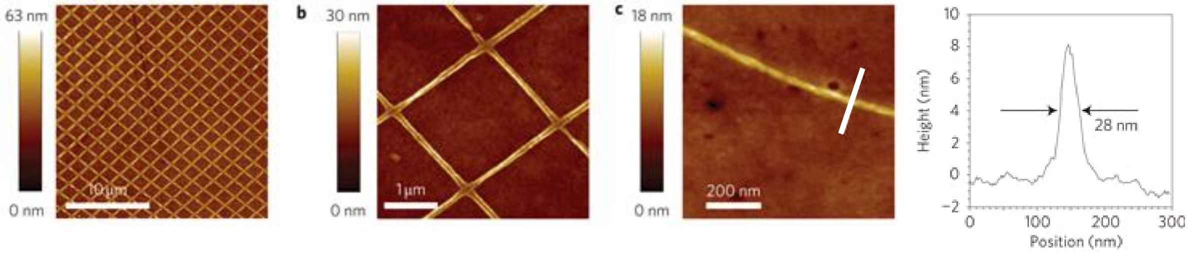

Figure 5.2: Adapted from [52] a) AFM image of a square grid of PPV structures with line spacing of 2 µm produced by scanning the probe in two perpendicular directions at 230°C and 10 μms^{-1} (all lines consist of both trace and retrace), b) a similar set of structures drawn at 5 μms^{-1} and 250°C, c) an isolated, single-scanned line drawn at a temperature of 250°C and a scan speed of 5 μms^{-1} on a 15 nm-thick film. The cross-section (right) shows the FWHM of the line to be 28 nm.

5.1.3. Achievable resolution

The latter result of a 28 nm feature is somewhat surprising, given that the radius of the Wollaston wire probe is two orders of magnitude larger. To understand the apparent discrepancy between these two length scales, Dr Fenwick conducted a series of modelling studies using finite element analysis of heat transfer through a two-dimensional slice of the probe, polymer film and substrate system. Both conductive and radiative processes were considered, however it was found that conduction was by far the dominant mechanism at temperatures relevant to this study, in line with previous observations [155].

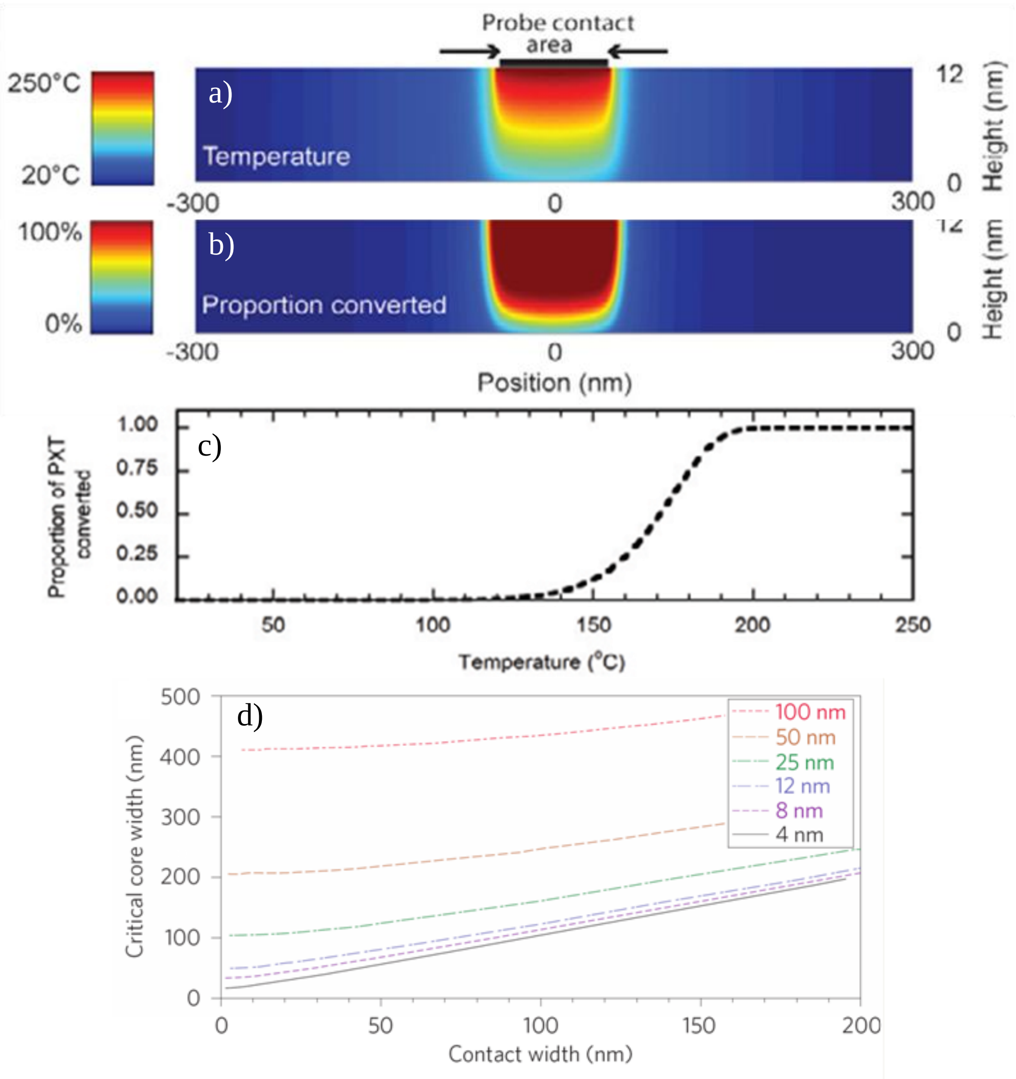

Figure 5.3: Adapted from [52] a) the predicted steady-state temperature profile inside a 12 nm polymer film for a probe temperature of 250°C and a probe-sample contact area of 95nm, chosen to correspond to the indentation width observed in undeveloped films, b) conversion profile at 4.8 ms, calculated using the temperature profile from a) and the conversion ratio of PXT as a function of temperature c) computed using the Arrhenius equation. d) Predicted relationship between critical core widths and contact width, calculated by as for optically defined features, as a function of film thickness (colour scale).

By considering conduction alone, a map of the temperature profile throughout the system could be generated. Once again utilising the critical-core model of structure formation as a qualitative guide, the relationship between contact area, film thickness and feature size could be calculated using this profile. A summary of these results is shown in Figure 5.3.

The key observations here are twofold. The first is that high resolution lithography can be expected if the contact width of the probe with the sample is kept low – so that a large probe can indeed define extremely small features if the film and probe are sufficiently hard and smooth and the probe scans quickly enough not to deform, and sink into, the film. The second is that if the contact area of the probe can be reduced, then even smaller lithographic features should be possible, significantly smaller than those possible using SNOL (for which the aperture size dictates a lower limit). In fact, it appears from this work that structures significantly *smaller* than the contact area can be drawn. Since the patterned material is PPV, this will be partly due to the precursor shrinkage described in section 4.1.4. It may also be an example of a relaxation of the requirements for full anchoring implicit in the critical core model – for these extended linear structures, only partial or intermittent attachment to the substrate is required for features to be retained after development, which will be illustrated further in section 5.2.2.

5.2. Lithography using a nano-thermal probe

Based on the modelling conducted by Dr Fenwick, and summarised in section 5.1.3, two primary limits exist on the resolution of structures patterned using a micro-thermal probe. The first is film thickness, due to lateral conduction of heat away from the probe through the film. In this case, film quality limits the minimum thickness to around 15nm, as with previous optical lithography. The second is probe size, specifically probe contact area, which may be minimised by switching to a nano- rather than micro-scale probe. It is this modification which is investigated below.

5.2.1. Instrumentation

The probes used for nano-thermal lithography consist of a dual-armed silicon cantilever with a sharp AFM tip at its apex. The typical contact area of such a probe is expected to be less than 20 nm. The arms of the cantilever are highly doped, while the tip is left undoped and resistive, a similar approach to that used by the Wollaston wire probes described above. Passing a current between the arms therefore leads to power being dissipated preferentially in the section of cantilever in contact with the tip, heating it. When used as a nano-thermal analysis tool, variations in heat flux from the tip to the sample are recorded as it scans over the surface [156]. To initiate thermochemical reactions, the tip is held at constant temperature (by monitoring its resistance) and scanned over the surface. The method is largely identical to that described in section 5.1.1, and the PXT/PPV system is again used. An SEM image of an Anasys nano-thermal probe of the type used in this study is shown in Figure 5.4. Examples of nano-thermal lithography using this kind of probe exist in the literature. For example, Wang *et al* defined 70 nm-wide trenches in PXT by conversion to PPV using a hot cantilever probe [151]. However, isolated features have not to my knowledge been previously fabricated in this way.

The system used to conduct the thermal lithography was based around a modified Explorer AFM operating in contact mode, on to which an Anasys probe had been mounted. The standard AFM software was used to control scanning and feedback, with probe temperature being controlled by a separate unit, as previously.

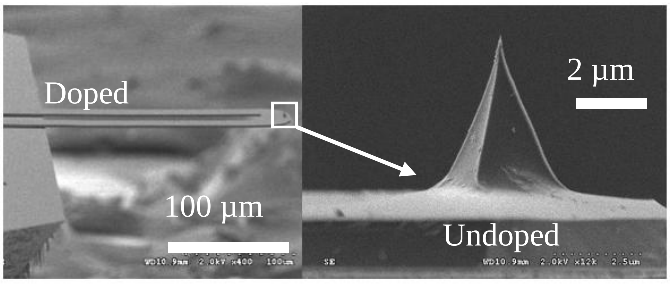

Figure 5.4: SEM images of an Anasys doped-silicon nano-thermal probe. Tip curvature is ~20 nm. Images provided by Anasys Instruments.

5.2.2. Lithography

Due to the nature of the scanning system, for this investigation the most convenient patterns to draw were raster-scanned lines, each line being scanned twice by the probe. By rotating the scan ±45°, grids of scan lines were also demonstrated. It was in principle possible to draw individual dots by holding the tip in contact and heating the probe, but defining sufficient numbers of these structures to be found again using an AFM after development was not possible. Figure 5.5 presents examples of the line and grid structures drawn.

Using these structures as a basis, strength of contact, probe temperature and scan speed were systematically investigated to attempt to optimise the lithographic resolution. Probe temperature was set by fixing the supply voltage to the probe, and calibrated by conducting local thermal analyses of two standard plastic samples PET (melting onset 250°C) and PCL (melting onset 60°C). The dependence of temperature on supply voltage was assumed to be linear within this range. Probe temperatures in the range 170-190°C were found to generate well defined structures, with very little correlation between temperature and quality of structure. The majority of structures shown below were obtained at 170°C.

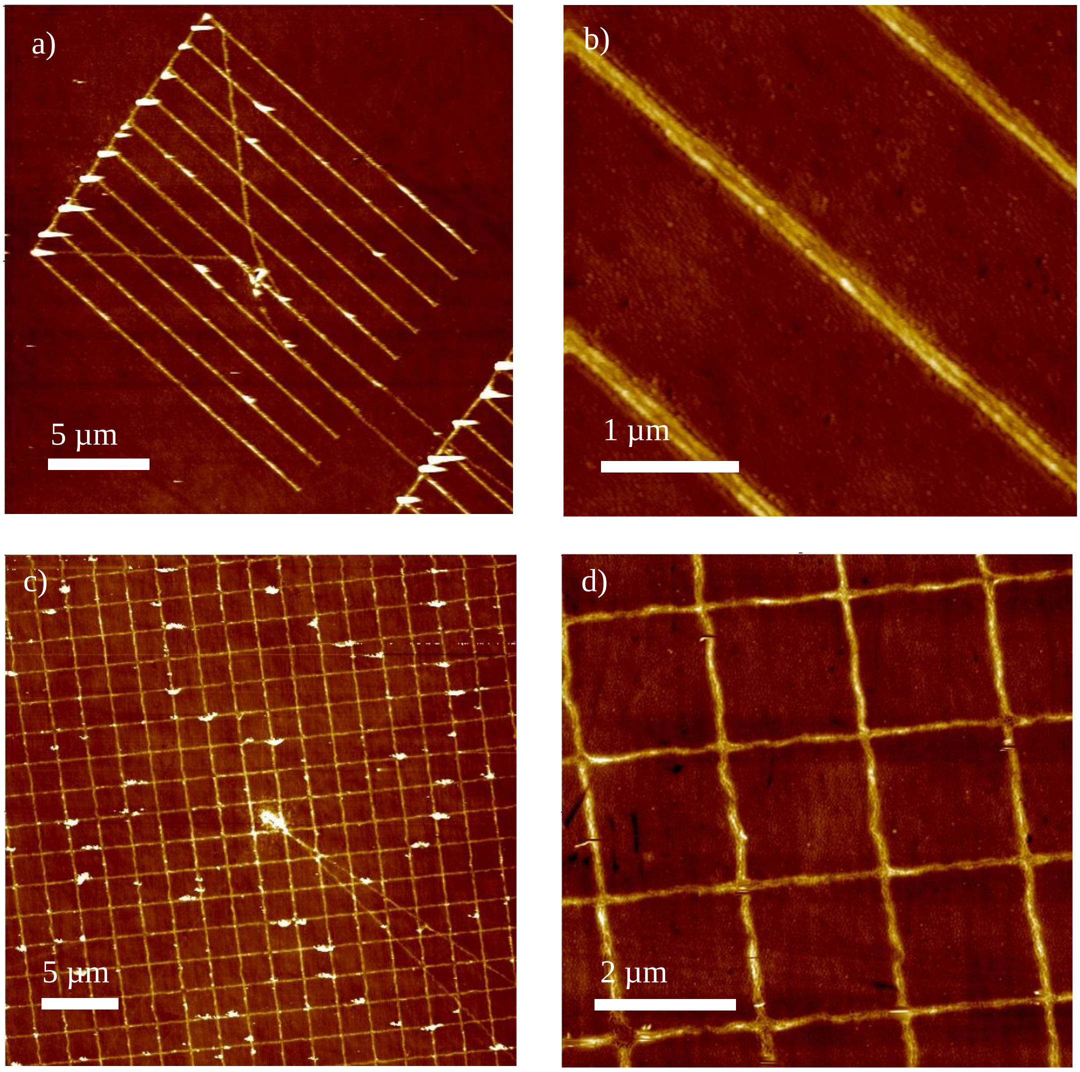

Figure 5.5: a) 26.1 µm tapping-mode AFM image of a 10-line single raster scan at 10 µms^{-1} using a 0.5 nA set-point offset. Vertical range capped at 40 nm. Note the regular piles of debris near to the scan lines, leading to topographical artefacts. b) 3.79 µm zoom of same image – note the double lines present. Vertical range 25 nm. c) 33.3 µm AFM image of a dual 25-line raster scan at 40 µms^{-1} using a 0.5 nA set-point offset . The central structure and lines where the hot probe has travelled to start the grid can be seen. Vertical range 20 nm. d) 7.16 µm zoom of the same image. 15 nm vertical range.

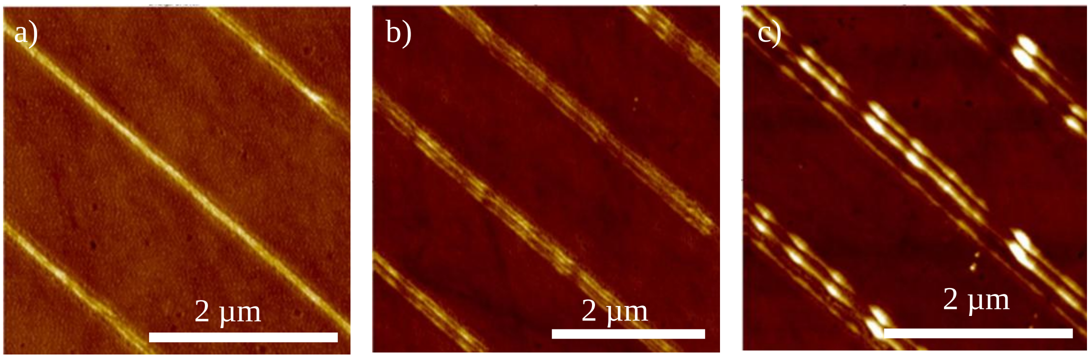

Figure 5.6: Zoomed tapping-mode AFM images of 10-line raster scans at 20 μms^{-1} and probe temperature 170°C. Set-point offsets are a) 0.5 nA, b) 1 nA and c) 2 nA. Vertical range 28, 23, 40 nm.

The quantitative contact strength was not known, but could be varied qualitatively by altering the set-point offset. The minimum set-point increment for this system was 0.5 nA. Therefore, a drop of 0.5 nA (the difference between the free space signal of the feedback system and the operating point) was the smallest signal that allowed contact to be maintained. Figure 5.6 compares the results of varying this set-point offset at fixed temperature and speed.

Two phenomena can be identified from this data. First, all scans appear to show double, treble or quadruple line structure. Combined with the debris seen in Figure 5.5, and other images, it appears that the probe sinks into and scratches the polymer precursor. Second, this scratching increases as the set-point is dropped. This is particularly evident from the 2 nA scan, where the triple peaks can be interpreted as the result of two misaligned scratches from the forward and reverse traces of the scan, the misalignment either due to drift, or an artefact of the scanning system. Even the 0.5 nA lines exhibit some internal structure, though the origin of this is less clear. Similar phenomena are seen for other temperatures and scan speeds not presented here. The best structures, as with the micro-scale investigation above, are obtained using the lowest set-point offset (0.5 nA here), since this involves the lightest contact with the surface and thus the least sinking/scratching and the smallest contact area.

Given the lower limit on contact force available for this investigation, and based on the findings of the micro-thermal patterning described above, the scanning speed of the system was varied to set the effective contact time and find an optimum. As expected, higher scan speeds lead to thinner, less well attached lines, shown in Figure 5.7. The optimum occurs when the lines are just attached to the surface, but have the smallest practical cross-section. In this case, the optimum was found to be at a scan speed of

20 µms^{-1}. Faster than this, the attachment of the sample to the surface is compromised and the lines can move during development, slower and the probe converts a larger area of material than necessary. These observations are qualitatively consistent with the predictions made by the critical core model of structure formation.

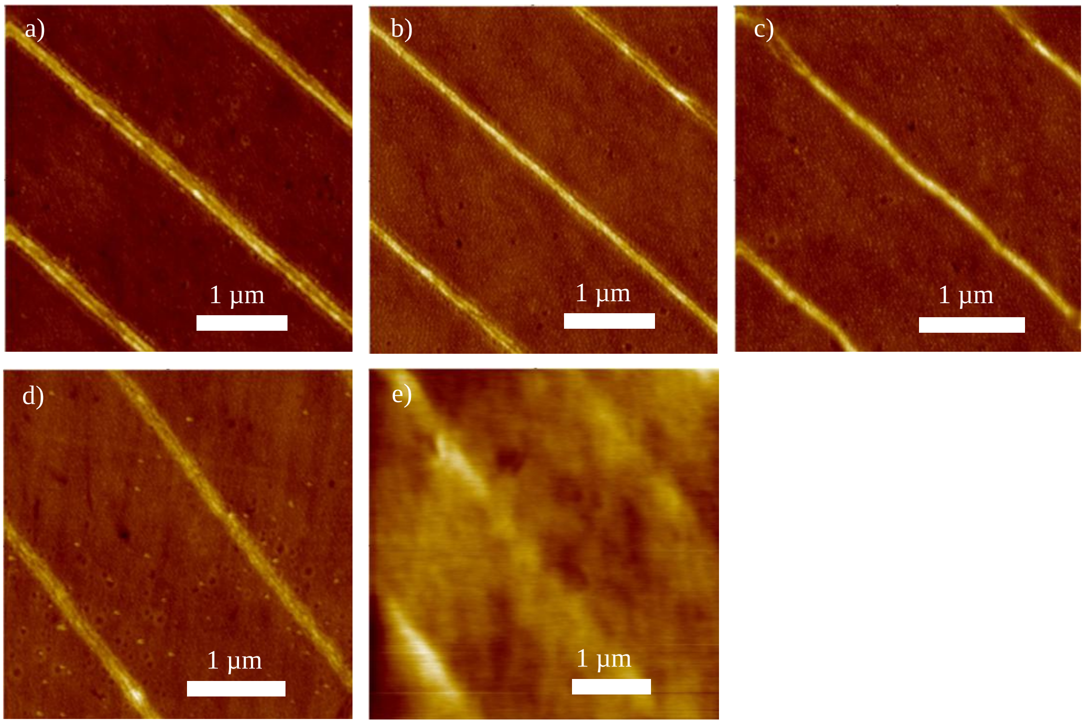

Figure 5.7: Tapping-mode AFM images of lines produced for a) to e) 10, 20, 40, 80 and 100 µms^{-1} scan speeds. The top three images (10, 20, 40 µms^{-1}) correspond to scans at 170°C , while the bottom (80 and 100 µms^{-1}) to scans at 190°C. Above the optimum, the faster the scan rate, the more patchy and poorly attached are the structures created, to a greater extent than visible in these zoomed-in images. Vertical ranges are 25, 28, 27, 27 and 7.5 nm respectively.

The highest resolution, well-defined structures created during this investigation were obtained using 0.5 nA set-point offset, scan speed of 20 µms^{-1} and probe temperature ~170°C. Figure 5.8 shows a zoomed-in AFM image of some of these lines. It is clear that these are generally double structures – either due to the forward/backward scan directions or sinking of the probe into the surface – and there is still considerable scraped-out debris present around them. However, where the double lines either overlap, or the probe scratches less, then the minimum feature width drops to around 60 nm FWHM (Figure 5.8 region A). This is equivalent to the resolution obtained over similar length-scales with the SNOL system, but still larger than that obtained using the Wollaston wire. However, if the features drawn are assumed to indeed comprise double lines, areas may be sought where the two lines separate, either due to incomplete attachment to the substrate or drift in the scanning stage. Such a region (B) exists in

Figure 5.8 where two distinct features can be seen, one of which is underexposed and has moved from its intended position. The well-attached feature left behind has FWHM of just over 30 nm.

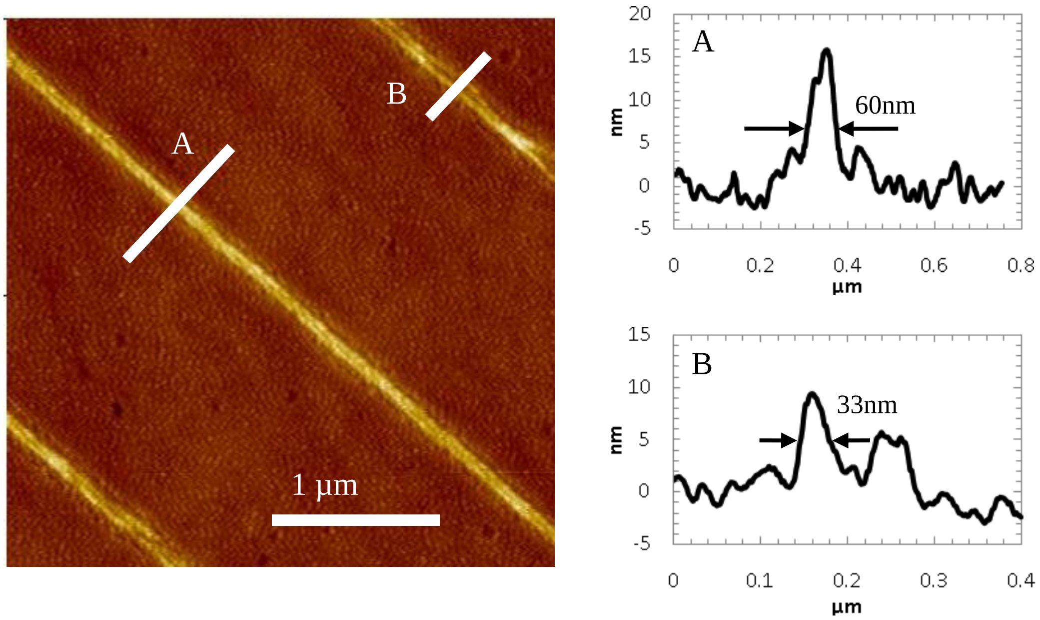

Figure 5.8: (main) 3.25µm tapping-mode AFM image of some of the best PPV structures drawn. Vertical range 30 nm. The double-line nature of the structures is clearly visible. (insets) Cross-sections through the central line at A demonstrating a feature width of ~60 nm full width at half-maximum, with an additional section at B showing the single-feature width or 33 nm.

5.3. Conclusions

It has been demonstrated here that lithography with an Anasys nano-thermal probes with lateral resolution down to 60 nm is achievable, and potentially as low as 30 nm if the above interpretation of double features is correct. However, the investigation into the effect of reducing the contact force of the scanning system demonstrates that this is unlikely to be an optimised figure, since the lower limit on contact force was dictated by the Explorer AFM system. It is not surprising that this limit has been encountered using the sharper nano-thermal probes, since these exert a greater pressure on the polymer surface than the Wollaston wire. The extent of the contact area of the wire would seem to have reduced the contact pressure sufficiently that an optimum could be reached within the range provided by the Explorer, but that this optimal pressure was not achievable using the nano-thermal probes. It is anticipated that replicating this system on an AFM which is capable of more delicately controlling the contact force should lead to a further improvement in resolution.

6. Near-field microscopy

So far, this thesis has primarily discussed the near-field microscope within the context of its use as as a lithographic tool, where it has been shown that such a tool provides a versatile non-destructive method for arbitrarily patterned micro- and nano-scale features in a variety of functional polymers and organic materials. However, the tool itself was initially envisaged as a method of microscopy which could break the diffraction limit (Section 2.5). Since the first true near-field optical microscopes were realised in 1984, the use of SNOM in the imaging of conjugated polymers has primarily focussed on the imaging of polymer blends. As these blends typically segregate on nanometre length scales, only near-field techniques are able to resolve their substructure with the selectivity unique to optical measurements, although on-axis measurements using a Stimulated Emission Depletion-4π microscope can yield equivalent resolution (~30nm) in the vertical direction by using pulsed excitation to selectively deplete fluorescence close to the focal plane of the excitation [157].

A number of groups have used SNOM to map the photoluminescence profile of blend films to draw relationships between topography and chemical composition [158-160]. In principle, sufficiently detailed maps of photoluminescence can reveal the regions of a sample where emission and quenching take place, though imaging such interface processes is difficult and will depend strongly on the exciton diffusion lengths within the absorbing materials. A number of investigations using the SNOM to measure local changes in photoluminescence intensity are described in the sections below.

Various extensions to this technique are possible in order to obtain more detailed information on the local properties of a sample. Standard emission spectroscopy can be extended to the near field, a technique demonstrated in 1994 to allow real time shifts in the spectra of single emissive molecules dispersed on PMMA to be monitored [161]. The faster-time (picoseconds-scale) dependence of fluorescence emission from organic materials can also be probed using SNOM as a near-field source for time-correlated single photon counting [162]. Similarly, the highly chemically-specific technique of Raman spectroscopy for measuring vibronic transitions within a material can be coupled with SNOM to explore the local chemical environment of a sample [163]. In particular, the use of a conducting apertureless SNOM probe has been shown to greatly increase the Raman signal from a surface [164, 165]. Returning to the original implementation of the near-field microscope as tool for infrared spectroscopy has also yielded useful results [166, 167].

The other primary microscopy application suitable for SNOM is the local mapping of blend devices, again due to the nano-scale phase separation and interface processes associated with their active layers. Device measurements of standard sandwich-structures are difficult to make, given that the region of interest is typically far from the SNOM probe tip. However, by utilising laterally (rather than vertically) separated electrodes, the active layer can be accessed directly. Measurements in this configuration include the mapping of electroluminescence from polymer blend LEDs by applying a bias to the near field probe and generating local electroluminescence [168] and the mapping of photocurrent generation in polymer photovoltaics [169, 170]. As shown by Riehn *et al*, and others, both photoluminescence and photocurrent measurements can in principle be measured simultaneously [171]. Additional uses have also been demonstrated, including the mapping of optical fields across compact or nanostructured objects such as photonic crystals [172]. All of the above techniques suffer from the main drawback of the serial nature of SNOM, in that data from each pixel must be acquired sequentially, which leads to prohibitively long acquisition times in the situations of large sample size, fine acquisition detail or low signal to noise ratio. A number of groups have investigated the possibility of improving the scanning speed of SNOM systems by using alternatives to mechanical feedback systems. For instance, an all-optical technique has been demonstrated which allows the strength of the near-field signal itself to be used as the reference parameter for the feedback system, achieving 10 ms acquisition times for a 20 × 20 μm scan [60]. The drawback of such a system however is that entirely flat samples must be used, and no topographic information is available.

It should also be emphasised that it is not generally the scanning speed of the stage which limits the image acquisition time for SNOM, but the time required to collect sufficient photons at each pixel (even at high incident laser power), due to the necessarily low illumination volume. This contrasts with the SNOL scans described in section 4. There, the incident laser power typically had to be reduced using neutral density filters, because the mechanically-limited lower bound of ~10 ms exposure time per point was found to overexpose the majority of samples when operated at full power.

Investigations implementing the near-field system previously described in section 3 as an apertured scanning near-field microscope are described below.

6.1. Transmission mode SNOM

6.1.1. Instrumentation

Transmission mode SNOM is an analogous technique to conventional backlit far-field microscopy, or more precisely transmission mode confocal microscopy. The near-field light source, comprising a sub-wavelength aperture illuminated by monochromatic light, is scanned at close range over the sample to be imaged. Light scattered, or emitted, by the sample and transmitted through the substrate is collected point by point in the far-field, using a lens and photodetector. Any far-field contribution to the signal will vary very slowly as the tip is scanned, and can be subtracted as background or removed using a lock-in technique. Due to the very limited extent of the near-field, and depending on the illumination wavelength, only the top few 10s of nanometres of the sample will be probed by the field (if the sample is flat). For this reason, and the necessity that the sample should not be too strongly absorbing, thin films of material deposited on transparent substrates are most successfully studied with this technique. Despite this limitation, the ability to place optics very close to the back of the sample allows for a large numerical aperture for collection (around 0.7), and consequently a high signal-to-noise ratio.

Pure absorption can be measured by monitoring the total transmitted light through the system. The illumination (and any fluorescence from the optics or substrate) can be filtered out to measure fluorescence from the sample. In all cases, photons were collected using a photomultiplier tube connected to an electronic discriminator. Total counts for each pixel were recorded alongside topography by the Adwin control electronics. A schematic of the system used to make the transmission-mode measurements is shown in Figure 6.1.

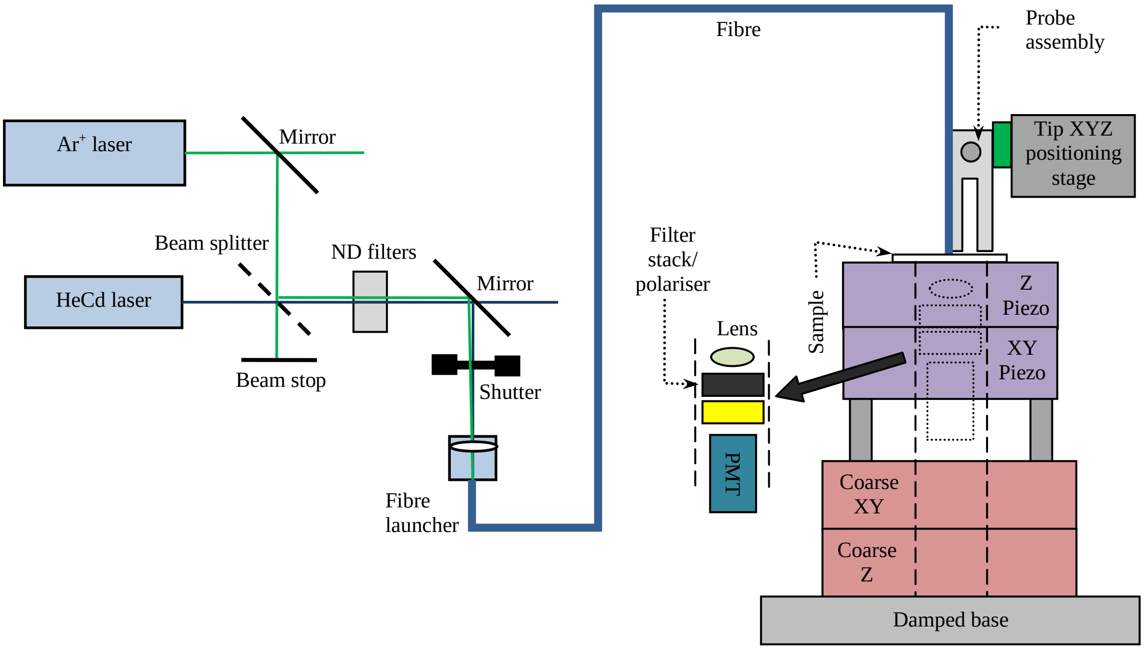

Figure 6.1: Schematic of the experimental arrangement specific to transmission-mode SNOM (electronics omitted).

6.1.2. Imaging of HBC-PDI whiskers

Many small molecules and polymers form, under appropriate conditions, aggregate phases in solution. The nature of the aggregate phase depends on the nature of the material and its environment. One common aggregate morphology is that of micro- or nano-whiskers, elongated crystalline phases which form under the general conditions that a preferential direction exists during crystal growth. For atomic crystals, this may represent a crystal plane with a higher surface energy. For organic molecular crystals, π-π stacking interactions between adjacent molecules may induce a similar effect. For this reason, planar molecules such as the hexa-*peri*-hexabenzocoronenes (HBCs) and perylene diimides (PDIs), where π-π interactions can dominate, have been shown to form extremely long molecular wires and complex self-assembled structures, outlined for HBC in section 4.4. The same can be achieved for certain conjugated polymers, where it is understood that individual chains may be induced to stack in relatively flat coils, again generating wires with extremely high aspect ratios. In organic electronic devices, it has long been understood that the relatively low polaron mobilities observed for most materials is due to inefficient transport from one disordered region to another via slow inter-molecular/inter-chain hopping. Intra-molecular transport through conjugated regions is considerably faster, but difficult to utilise in amorphous or semi-crystalline layers. Forming organic molecules into long, π-stacked whiskers is one method by which long-range mobility through the active layer can be increased. Such structures have been used as a controlled, high-mobility phase to improve the performance of organic devices, including organic solar cells [173, 174].

Methods for growing whisker aggregates from organic materials vary. Pre-forming in solution is one technique suitable for a wide range of organic polymers, where varying solubility levels (for example, by altering solution temperature or non-solvent fraction) may be used as a driving force to initiate aggregation. Another method used for encouraging small molecules to aggregate after deposition has been described by Samori and co-workers, and involves “annealing” a thin amorphous film of material in a saturated solvent-vapour atmosphere. The addition of the solvent vapour allows the molecules to explore more of their local energetic environment, and enables them to aggregate *in-situ* into lower-energy π-stacked structures, including whiskers. This in-film aggregation effect has been demonstrated for a range of materials, including the nano-graphitic electron donor HBC-C_{12} and variants of the planar electron acceptor PDI [175].

Using the solvent-vapour annealing (SVA) technique, mixed films of HBC-C_{12} and PDI2 were deposited by Dr Vincenzo Palermo[*] and colleagues onto glass substrates, then solvent-vapour annealed in a THF atmosphere. This resulted in the growth of networks of micron-scale whiskers radiating from nucleation sites across the film. An optical micrograph of one such sample, also provided by Dr Palermo, is shown in Figure 6.2. It appears from this image (and others) that the film comprises large clearly-resolved needle-like structures, surrounded by smaller fibres which are significantly more difficult to resolve optically. Given that HCB and PDI are both known to form whisker aggregates, it is not clear if this represents a two-phase system or a simple hierarchy.

In this investigation, the SNOM system was used to establish how the HBC and PDI components of the films distributed themselves within the whiskers, and in particular whether distinct n- and p-type structures were present or whether the whiskers formed from a mix of both molecules. It is clear from the size of the aggregates that either scenario is plausible, since their large dimensions show that they are not necessarily

---

[*] Istituto per la Sintesi Organica e la Fotoreattivita’, Consiglio Nazionale della Ricerche, Bologna, Italy

mono-crystalline and certainly not formed of single columns of identical molecules. The SNOM is an appropriate tool to answer this question, since the small size of some of the features present in the samples prevents them being observed easily through a conventional microscope.

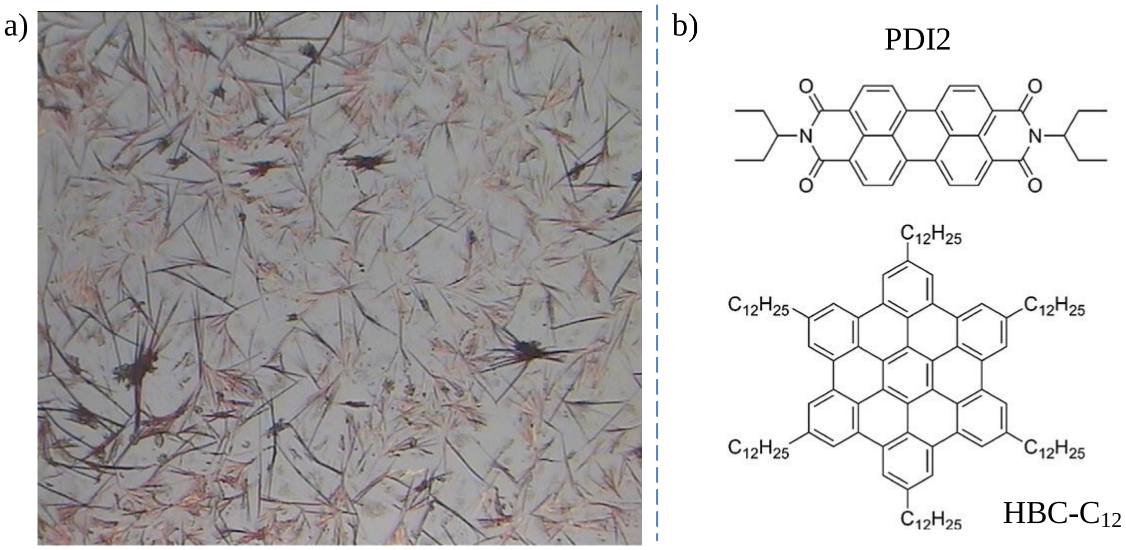

Figure 6.2: a) Optical image provided by Dr Palermo of a vapour-annealed HBC-C_{12}:PDI2 film spun from THF onto a glass substrate providing an overview of the fibre orientations. This particular film, and one other similar to it, were chosen for study using the SNOM due to their good fibre coverage. b) chemical structures of PDI2 and HBC-C_{12} molecules, used as building blocks for the organic micro-whiskers shown.

To map the position of the different species in the whisker networks, the different fluorescent properties of the two materials were utilised. Absorption spectra in solution for the two building-block materials are shown in

Figure 6.3.

HBC exhibits a narrow absorption around 365nm, PDI a broad absorption from 460-540 nm. When combined in a thin film on a glass substrate and solvent-vapour annealed, a mixed absorption profile is observed, with the HBC peak broadening and blue-shifting slightly to around 340nm, and the PDI peak similarly broadening and centred on 500 nm as shown in Figure 6.4.

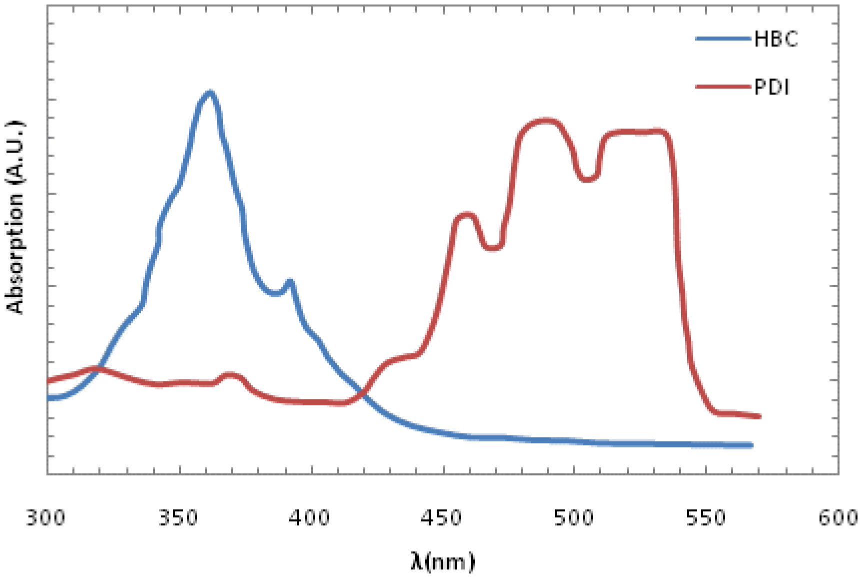

Figure 6.3: Absorption spectra of pure HBC-C_{12} and PDI2 in solution. The PDI absorption is saturated around 510-540 nm.

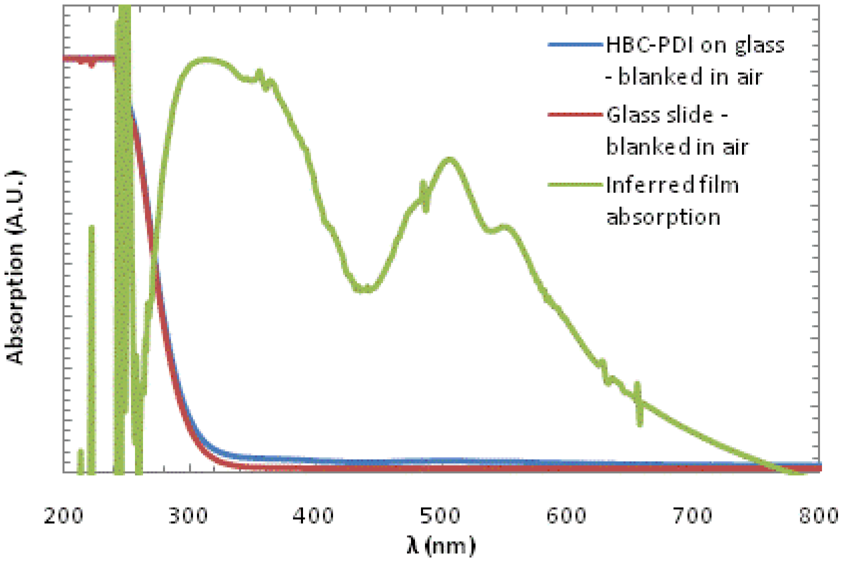

Figure 6.4: Absorption spectra of a mixed HBC-C_{12} and PDI2 thin solvent-annealed film. The profile has been obtained by manually subtracting absorption from a blank slide from the sample profile, due to the low density of material on the slide.

These data indicate that the HBC component of the film may be preferentially excited using light at 325nm, provided by a HeCd laser, and the PDI component excited using light at 514nm, provided by an Ar-ion laser. To verify this, the photoluminescence profile of the combined HBC-PDI whisker film was measured at these two excitation wavelengths, and is shown in Figure 6.5. It can be seen that while excitation at 514 nm produces a single photoluminescence response from PDI, centred at 615nm, excitation at 325 nm produces a double peaked profile corresponding to combined emission from both HBC and PDI. Single-component HBC-C_{12} photoluminescence solution spectra provided by Dr Palermo show no HBC emission beyond approximately 550 nm. This double peak may be understood by noting that the emission spectrum of HBC overlaps significantly with the absorption spectrum of PDI, suggesting a strong dipole-dipole interaction is possible between the chromophores which allows Förster resonant energy transfer to the PDI with subsequent emission. It may in addition be noted that given the low density of the whisker films under investigation, and given the relatively efficient, but incomplete, energy transfer observed, the HBC and PDI must be intimately mixed in at least some regions of the film, but possibly not in all regions.

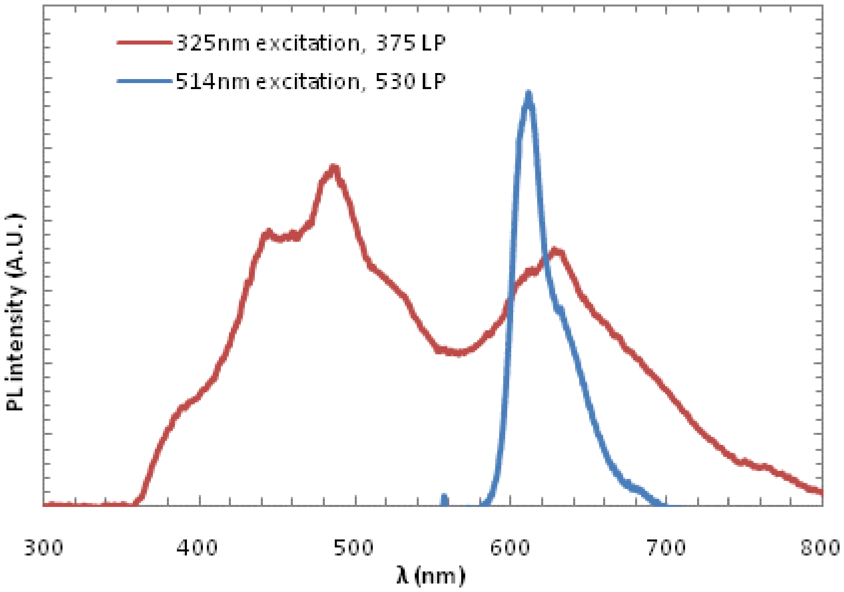

Figure 6.5: Photoluminescence spectra of a mixed HBC-C_{12} and PDI2 thin film using 325 nm illumination and a 375 nm long-pass filter, or 514 nm illumination and a 530 nm long-pass filter.

Based on the above observations, collections of fibres on the illustrated sample were investigated under the SNOM using either an Ar-ion laser operating at 514 nm or a HeCd laser operating at 325 nm for illumination.

Since the response of PDI at 514 nm gives the clearest compositional discrimination, initial measurements using illumination only this wavelength were taken. To exclude the laser signal, a combined stack of 590nm, 600 nm and 610 nm long-pass filters were inserted between the sample and the collection optics. Omitting these filters, clear absorption images of the fibres were obtained but no composition discrimination was possible. Figure 6.6 presents 20 × 20 µm topography and photoluminescence images of a cluster of small fibres taken using the SNOM system with 514 nm illumination through a 50 nm apertured probe. Exposure time for these images was 100ms per point.

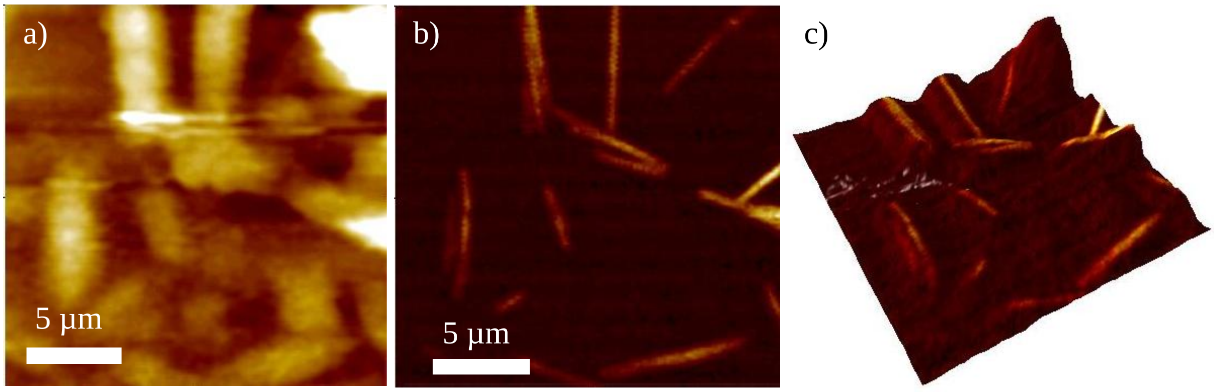

Figure 6.6: a) Topography image of a HBC-PDI fibre cluster, vertical range 540 nm. The image shows the effects of severe tip convolution. b) Simultaneous photoluminescence profile of the area using stacked filters as described. Colour range is 67 counts. c) 3D topography overlaid with photoluminescence profile demonstrating that the true fibre dimensions are likely far smaller than those measured directly.

The large feature at the top of the image appears to be translucent dirt, through which a faint photoluminescence signal can be seen. This is more clearly evident when the images are overlaid, as shown in Figure 6.6c). It can be concluded from these data that all of the smaller-scale whiskers contain PDI, since all topographic features are associated with PDI fluorescence.

Severe tip-convolution effects are visible in the topographic signal due to the large height of the whiskers compared to the tip size. While the probe aperture is of order 50 nm across, the aperture exists within a metallic plateau with diameter of order 1 µm as illustrated in Figure 3.3. In sections 4.5 and 6.2, shear-force topographic images with lateral resolutions considerably higher than this are nevertheless presented. This apparent discrepancy may be understood by noting that the surface of the plateau is typically rough, particularly after illumination has heated the probe [110, 144], with nanometre-scale metal protrusions. It is assumed that, if the plateau is aligned parallel to the sample surface, one of these protrusions will provide the first point of interaction and thus act as the topographic probe*. The active protrusion will therefore change from probe to probe and, most likely, from scan to scan. It has been observed that during operation, unintended hard contact or rapid scanning can lead to sudden, permanent shifts in feedback characteristics. This is interpreted as damage being caused to the

---

* By utilising a shear-force feedback system, direct contact between the probe and sample is usually avoided. "First point of interaction" is therefore intended to mean the region of the probe which first feels the short-range damping force from the sample.

current topographic probe (be it a protrusion or adhered debris), and subsequent shift to the next-largest protrusion as the active probe.

If the features of the sample are much larger (vertically) than the available protrusions, the rim of the probe plateau will itself act as the interaction surface and the recorded topography will be a convolution of the probe shape and the sample surface. The expected effect of this convolution both on topography and optical signal is illustrated for small hemispherical luminescent particles in Figure 6.7 [110]. By assuming the surface comprises a thin luminescent film, with luminescence intensity proportional to excitation density, and that a fixed fraction of the emitted photons are collected, the expected photoluminescence intensity when the probe is over a given point is modelled by summing the field density at all points on the surface. It can be seen that topographic convolution with the shape of the tip will be combined with topography-induced optical contrast, where in principle none should exist. Of most concern is the appearance of “shadow” zones either side of the high topography, from which no luminescence contrast will be visible in the final image. If instead a non-luminescent surface is assumed, on which hemispherical luminescent features are present, a distortion in the feature shape is expected as a result of the aperture leaving the surface.

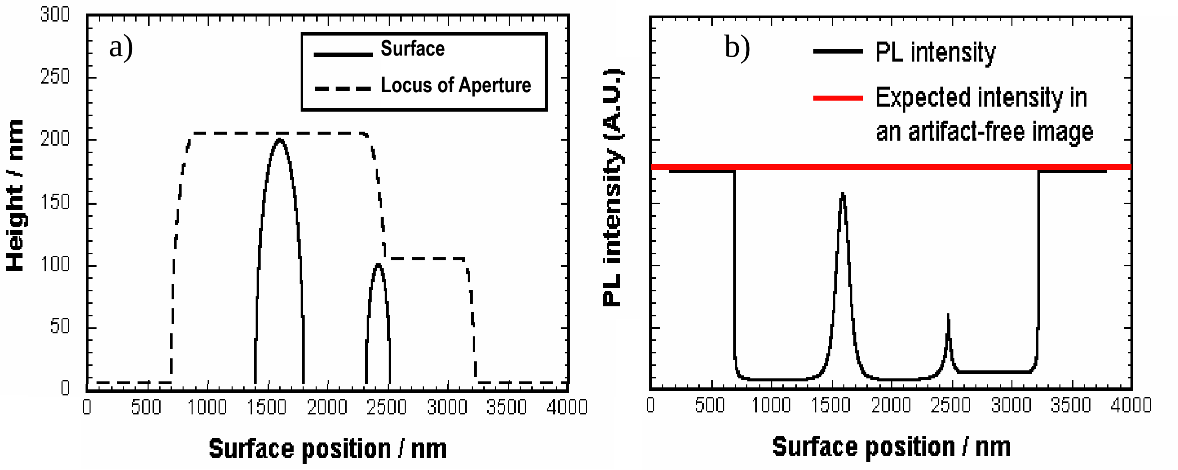

Figure 6.7: Reproduced from [110]: a) Simulated topographic line scan across a surface comprising two spherical features. Feature radii 200 nm and 100 nm, feature separation 850 nm, tip-sample separation 5nm, aperture radius 30 nm, probe diameter 1400 nm. b) Simulated simultaneous one-dimensional PL line scan calculated for the same surface, assuming that all points on the surface are equally luminescent.

A similar situation will occur in the case of the plateau being more than 2-3° away from parallel to the surface (the actual angle will be heavily dependent on exact probe structure), in which case one region of the plateau rim will act as the topographic probe. This is expected to manifest itself as a reduced topographic convolution effect coupled with both a horizontal offset between the topographic and optical signals and a loss of resolution in the optical signal due to the increase in aperture-surface separation. The full-probe convolution effect is more easily illustrated in Figure 6.8, which presents topography and photoluminescence data for a 20 × 20 µm area of film populated primarily by the larger needle-like aggregates. Illumination is once again at 514nm, and the same filter stack is used with 100 ms/point exposure time.

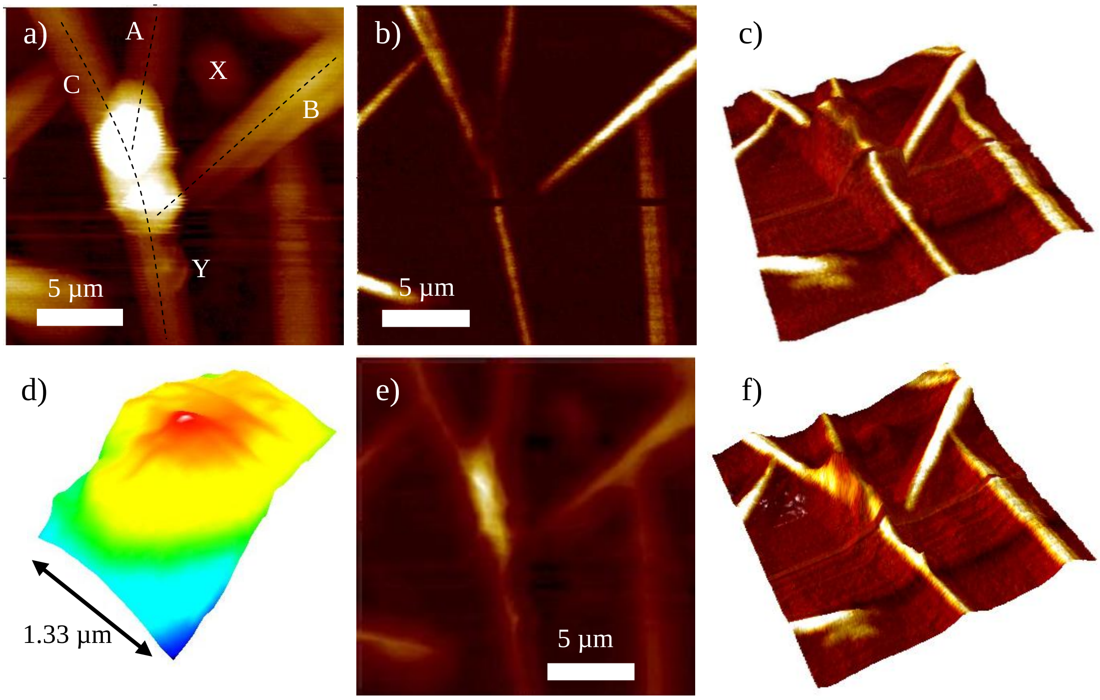

Figure 6.8: a) Topography image of a HBC-PDI fibre cluster, again with severe tip convolution, with various regions highlighted. Dotted lines are guides for the eye. Vertical range 500 nm. b) Photoluminescence image taken using 514 nm illumination of the same area. Colour range is 60 counts. c) Overlay of PL on 3D topography. d) 3D visualisation of the estimated tip profile calculated from image a) using a single 3 × 3 Gaussian smooth and discounting low-lying regions. Vertical range 300 nm. e) Deconvolution of image a) using tip profile d) to estimate the true topography. Vertical range 400 nm. f) Overlay of raw PL data with deconvoluted topography. The good alignment indicates that the PL signal originates near the centre of the topographic probe.

Examining the raw data, it can be seen that PDI photoluminescence is once again seen for all topographic features, except for a small protrusion in Figure 6.8a) marked X, suggesting that both micro-whisker phases may be compositionally similar. In addition, extensive and consistent tip convolution effects are seen since these structures range over 200-300 nm in height. In particular, where whiskers A and B intersect whisker C, two very large (> 400 nm high) circular features are observed, with a third circular feature present at point Y. The large features likely arise from the whiskers crossing, producing topography with double-height. This in turn produces a region in the PL image b) with greatly reduced intensity, as explained by Dr Fenwick’s work. While the large features have similar sizes and symmetry, they are not the result of convolutions with point-like protrusions. Intriguingly, the smaller feature (Y) does appear to be the result of a small point-like protrusion as there are no whisker intersections or obvious debris in the area, leading to a rather clear (inverted) snapshot of the probe itself. Assuming this interpretation is correct, the probe is inferred to be cylindrical, with a diameter of 1.2 µm. A 15 nm high protrusion at the centre of the probe is also inferred.

Given the topography shown, and the interpretation that this is due to a strong convolution effect, it is possible in principle to deconvolute the image to obtain the true topography. In practice, this requires an accurate model of the shape of the particular probe used to take these images. This is unfortunately not known, but an alternative method is to calculate a blind tip profile from the measured topography. Specifically, it is possible to iteratively calculate the "worst case" tip profile – that is, the tip profile which would just scan over the measured topography without any part of the tip penetrating the sample. The term "worst case" refers to the fact that, by this method, the extent and volume of the tip will always be overestimated. Nevertheless, such a calculation will provide a semi-realistic tip shape, which may in turn be used to provide a bound on the true topography after deconvolution. The image processing software Scanning Probe Image Processor (SPIP) by Image Metrology was used to calculate a worst-case tip profile, and use this profile to deconvolve the raw image, leaving an estimate of the true underlying topography. The results of this deconvolution are show in Figure 6.8d,e). While these images only approximate the true position of the whiskers, overlaying the topography and luminescence images (Figure 6.8f) demonstrates that these is little or no offset between the two signals, indicating that the interpretation of the tip being held parallel to the surface is likely to be correct.

To investigate the distribution of HBC within the micro-whiskers, sequential images using 514 nm and 325 nm illumination were taken over various regions of the sample. Due to the height of the fibres, tip convolution continued to be observed. However, in this instance it is the photoluminescence rather than the topography which is of interest, so further deconvoluted topography estimates are not given here. Figure 6.9 presents a series of 20 × 20 µm topographic and PL images obtained at both illumination wavelengths. Signals arising from illumination at 325 nm are interpreted as originating from absorption by HBC (though potentially with energy transfer to PDI), whereas signals arising from illumination at 514 nm are due entirely to PDI. Since near-simultaneous images of the same region were required, and due to the sensitivity of the system to motion, the same filter stack comprising combined 585 nm and 550 nm long-pass filters was used for both excitations. This necessarily cut out the peak of the HBC fluorescence, but the HBC peak is sufficiently broad that emission was still distinguishable alongside PDI re-radiation. These images are presented in Figure 6.9. Subsequent investigations (not presented here) of the fibres using only 325 nm illumination and combinations of long-pass and 360-500 nm band pass filters to specifically image at the HBC emission peak were unable to obtain optical contrast due to weak blue fluorescence excited in the glass substrate, swamping the peak signal.

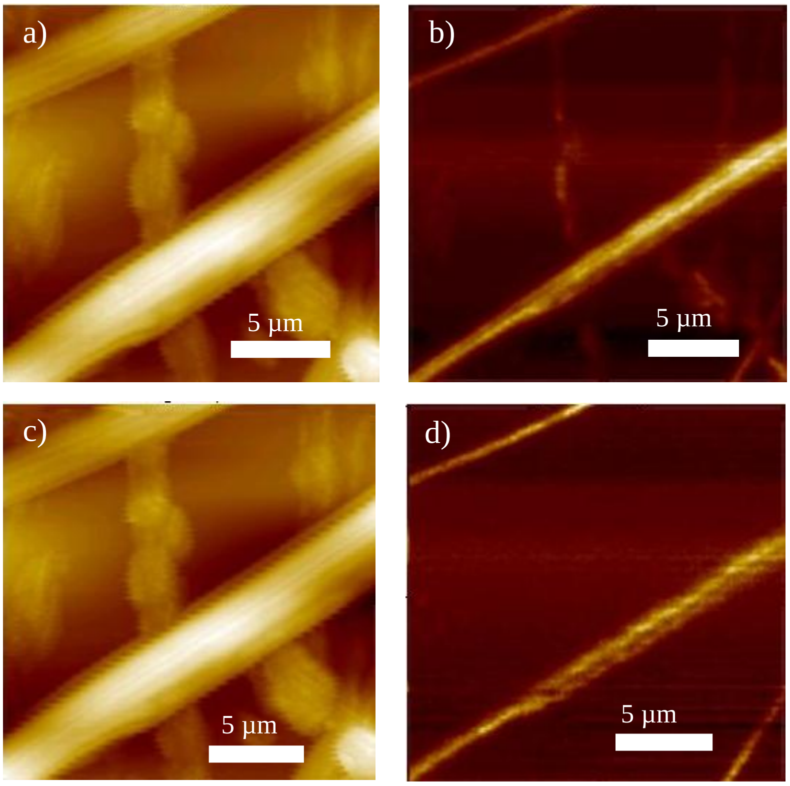

Figure 6.9: a,c) Topographic and b,d) luminescence images of a region of HBC-PDI fibres obtained sequentially with (a,b) 325 nm illumination and (c,d) 514 nm illumination. Colour scales are (a,c) 1.2 µm, b) 189 counts and d) 55 counts. Note the vertically oriented features seen in both topography images and image b), but not in image d).

Figure 6.9 shows that the primary needle-like nanowhisker phase contains both PDI (as previously seen) and also HBC. It is therefore concluded that the nanowhiskers are formed from a mixed HBC/PDI phase, which explains the origin of the efficient resonant energy transfer between the two. It also appears that some of the smaller (~100 nm high) linear features contain only HBC, and do not emit when excited at 514 nm. These form a fine, secondary whisker network, potentially representing regions of excess or leftover HBC which did not go on to form the main whiskers.

6.1.3. Polarisation SNOM of HBC-PDI fibres

Having determined the location of both HBC and PDI within the whisker networks observed, a final investigation of the orientation of emission from the whisker clusters was undertaken to understand whether the preferential growth direction of the whiskers leads in turn to a preferentially polarised emission. The emission polarisation was measured along two perpendicular directions by inserting a rotatable polariser below the filter stacks. Scattering within the sample and filters may increase the mixing between emitted polarisations, but it was anticipated that any strong contrast within the fibres should nevertheless be detectable. As shown in section 4.5, polarisation contrast is present in the illumination, but the polarisation is expected to be sufficiently well mixed that this initial polarisation will manifest only as an increase in intensity (but not overall contrast) along one polarisation direction. Figure 6.10 presents 20 × 20 μm topography and photoluminescence images (100 ms/point) taken of the same area of fibres using 514 nm illumination and a 600 nm long-pass filter stack, first with the polarizer aligned perpendicular to the fast-scan (horizontal) direction, then with the polariser aligned parallel to the fast-scan direction. Several differences are apparent between the two sets.

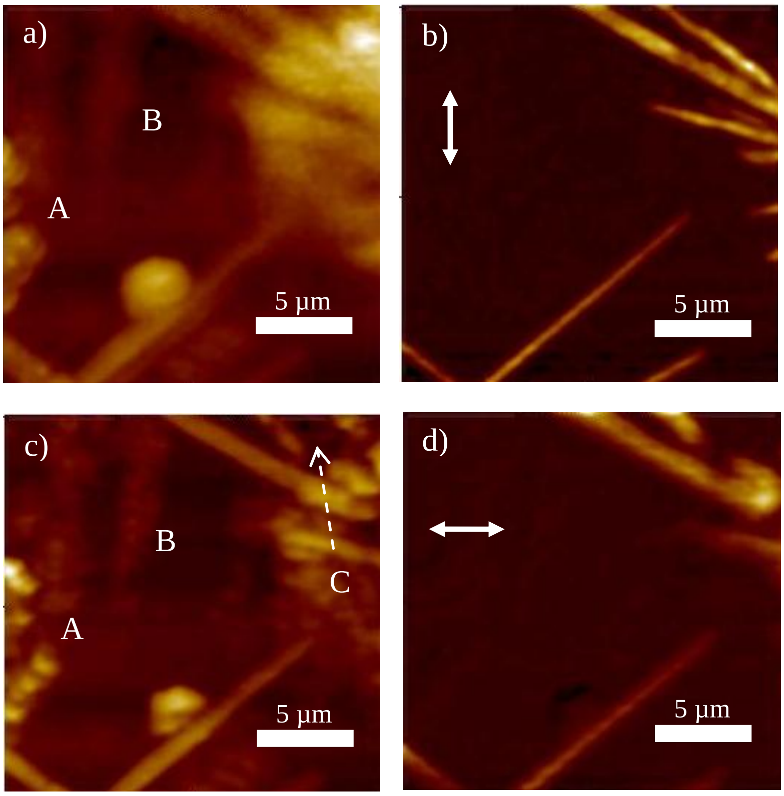

Figure 6.10: a,c) Topographic and b,d) polarised photoluminescence images of a region of HBC-PDI fibres taken sequentially with 514 nm illumination with various regions highlighted. In (a,b), polarisation is vertical and in (c,d) polarisation is horizontal with respect to the images. Colour scales are a) 230 nm, b) 75 counts, c) 235 nm, d) 130 counts.

The first images are characterised by poor topographic resolution, with features again reminiscent of point-like convolutions with the probe in region A, and good optical resolution showing comparable emission from all fibres irrespective of orientation. Emission is absent from the linear features in region B, which is interpreted as being primarily composed of HBC, by comparison with the similar features seen in Figure 6.9.

The second set of images was taken sequentially, but due to the long acquisition time was obtained approximately two hours after the first. They are characterised by a small drift in the imaged area of approximately 700 nm up and 700 nm to the left, improved topographic contrast with a very different convolution pattern in region A, reduced optical resolution and increased optical signal strength. There also appears to have been some damage to the structure at point C, reflected in both the topography and fluorescence images. These observations are consistent with damage occurring to the probe aperture arising from contact with the sample, likely occurring while the polarizer was rotated. Despite this damage, it can again be seen that emission is comparable between all fibres, so I may tentatively conclude that emission from these structures is not strongly polarised.

6.2. Reflection mode SNOM

6.2.1. Instrumentation

As compared to transmission-mode SNOM, reflection mode SNOM is an analogous technique to front-lit far-field microscopy, or reflection-mode confocal microscopy (where the main objective is used for both illumination and collection). The near-field light source is identical to that used in transmission-mode SNOM. Light scattered, or emitted upwards by the sample, or reflected from the substrate, is collected off-axis by a lens and photodetector. As with transmission mode, any far-field contribution to the signal will vary very slowly as the tip is scanned, and can be subtracted as background or removed using a lock-in technique. The necessity for a thin, transmitting sample is relaxed for this mode, allowing a wider variety of substrates and sample thicknesses to be used, though the volume probed by the near-field will be the same. One disadvantage of the technique is that the collection optics must generally be located at some distance from the sample, and at a very acute angle to the substrate to reduce shading of the emitting region by the SNOM probe. This limits the numerical aperture for collection significantly (to around 0.2).

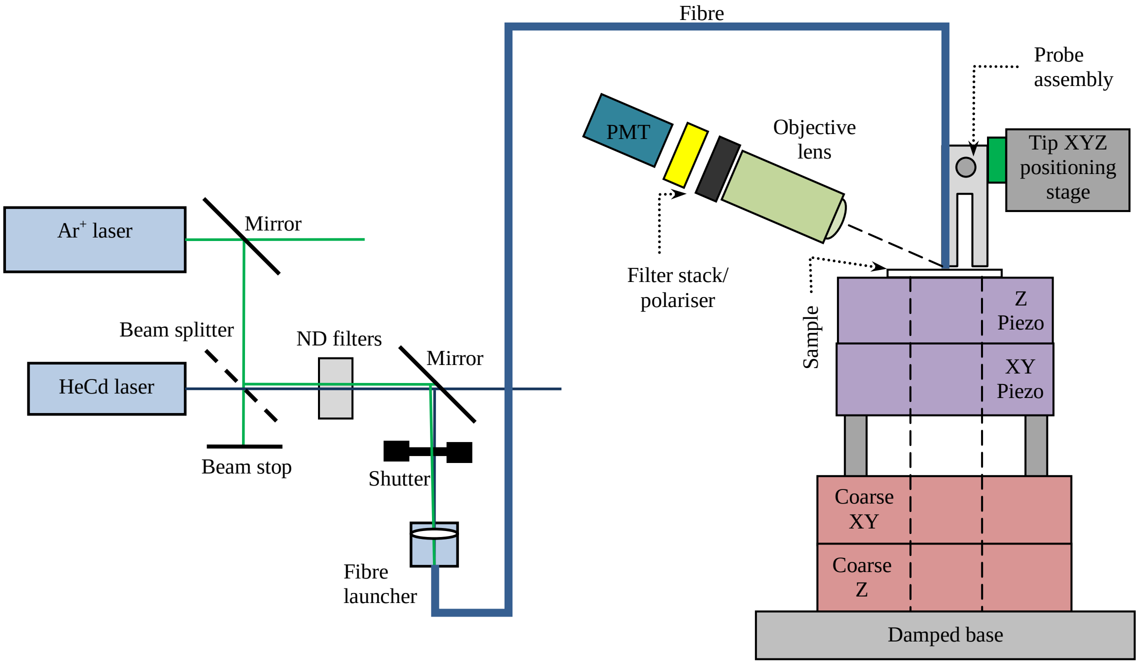

Figure 6.11: Schematic of the experimental arrangement specific to reflection-mode SNOM (electronics omitted).

Pure absorption is more difficult to measure using this technique than it is in transmission, but the off-axis collection makes it particularly suited to fluorescent imaging. Photons are collected using a photomultiplier tube mounted behind a microscope objective lens and connected to an electronic discriminator. Total counts for each pixel were recorded simultaneously with topography as before by the Adwin control electronics.

6.2.2. Photoluminescence imaging of polyrotaxane fibres

In previous sections, various routes for *in-situ* fabrication of nano- and micro-structure have been outlined. An alternative approach is to use supramolecular assembly either in situ or in solution, which has been demonstrated for a wide range of conjugated polymers to achieve controlled aggregates with beneficial architectures [44, 127, 173, 176, 177]. One system of materials which can be made to form rope-like supramolecular assemblies in solution are the polyrotaxanes.

Rotaxanated polymers consist of conjugated polymer chains partially encased by insulating cyclodextrin rings and capped by bulky end groups to prevent ring loss

(Figure 6.12). With sufficient cyclodextrin density along the polymer chain, a near-continuous coaxial molecule can be realised with a (semi-) conducting conjugated core inside an insulating cyclodextrin sheath. The clear similarity between this structure and macroscopic electrical cables has led to this class of molecules being referred to as ‘insulated molecular wires’.

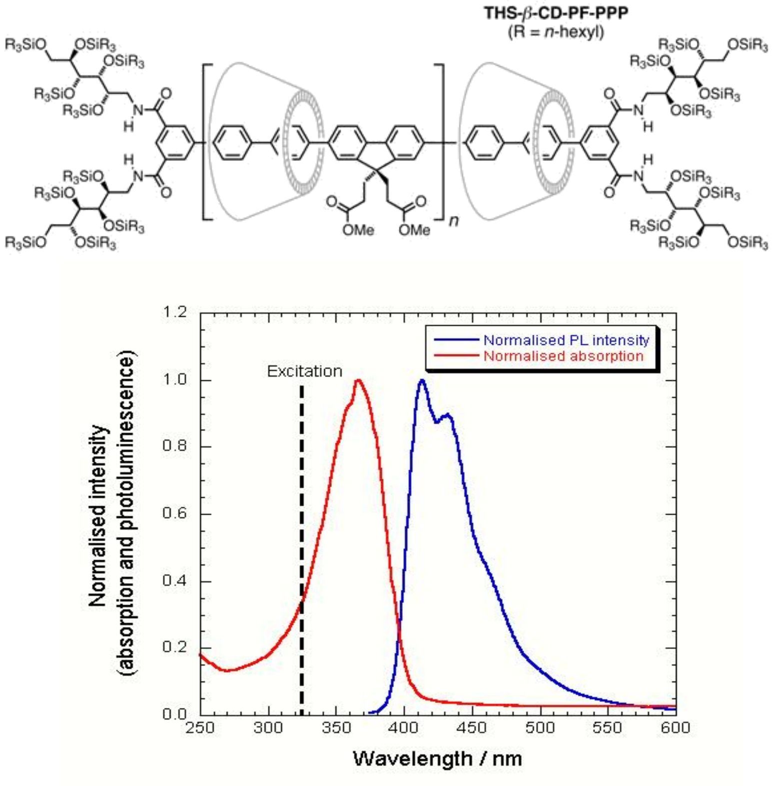

Figure 6.12: Chemical structure of the organic soluble polyrotaxane imaged (top) and its absorption and photoluminescence spectra (bottom). Absorption and photoluminescence data provided by Dr Joanne Wilson[*].

In solid films, the effect of this insulating layer is to inhibit parallel alignment of the polymer backbones by physically separating the chains [178]. Alignment of this kind has been shown to reduce luminescence yields compared to arrangements where the polymer chains are kept apart [179]. Preventing this kind of alignment should therefore improve the efficiency of polymer LED devices. The caveat here is that separating the polymer chains also reduces the ability of charges to hop between them, which limits charge injection. However, the cyclodextrin rings on a rotaxanated polymer are believed to be probabilistically, rather than uniformly, distributed leading to some sections of the backbone becoming exposed. These breaks in the insulation should allow the chains to

---

[*] Department of Physics, Cambridge University, Cambridge, UK

contact one another in a perpendicular configuration and allow charge transport, while still preventing parallel aggregation. Perpendicular intersection of this kind should not significantly decrease the luminescence yield [179].

To begin to understand whether charge transport is indeed efficient in supramolecular rotaxanated polymer networks, and if the material remains luminescent when forming these networks in a device-relevant orientation, the structure and luminescent properties of supramolecular fibres deposited between interdigitated electrodes has been investigated. Samples for this investigation were provided by Dr Vincenzo Palermo, who used an electric-field-assisted deposition technique to deposit rotaxanated polymers onto an oxide-capped silicon substrate patterned with 35 nm thick gold/titanium interdigitated electrodes with a 10 µm electrode spacing. The technique involved immersing the substrate in a chloroform/rotaxane solution for several hours while a voltage was applied between the electrodes. Varying substrate orientation, applied voltage and solution properties allowed supramolecular fibres to be deposited either on or between the electrodes, as shown in Figure 6.13. While it was not possible in this instance to align the fibres in such a way that they bridged the electrodes, the resulting fibre structures were nevertheless suitable for investigation under the SNOM.

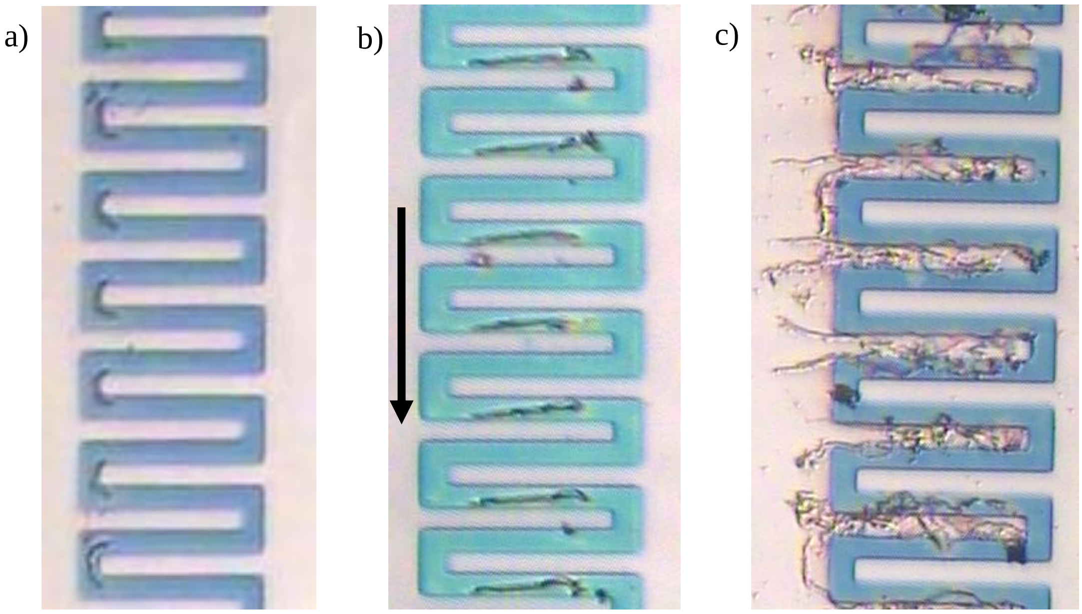

Figure 6.13: Optical micrographs provided by Dr Palermo of interdigitated gold electrodes on an oxide-capped silicon substrate coated in supramolecular assemblies of polyrotaxane fibres. Electrode separation is 10 µm. In all instances, the right hand electrode is held at 0V while the left hand electrode is held at a) 2V, b) 4V and c) 5V. In image b), substrate orientation was altered from flat such that gravity acted in the direction of the arrow.

The SNOM was used to map the photoluminescence of one such sample using excitation at 325 nm and collection in reflection mode through a 410 nm long-pass filter. Figure 6.14 presents simultaneous topographic and photoluminescence images obtained of a scan in the gap between two electrodes showing the detail of the fibre structure formed. The circular voids in the topography are believed to arise from bubbles developing on the silicon oxide surface during deposition, caused either by out-gassing of the solvent or, more likely, as a direct result of the electrodeposition causing hydrogen to be released at the surface [180].

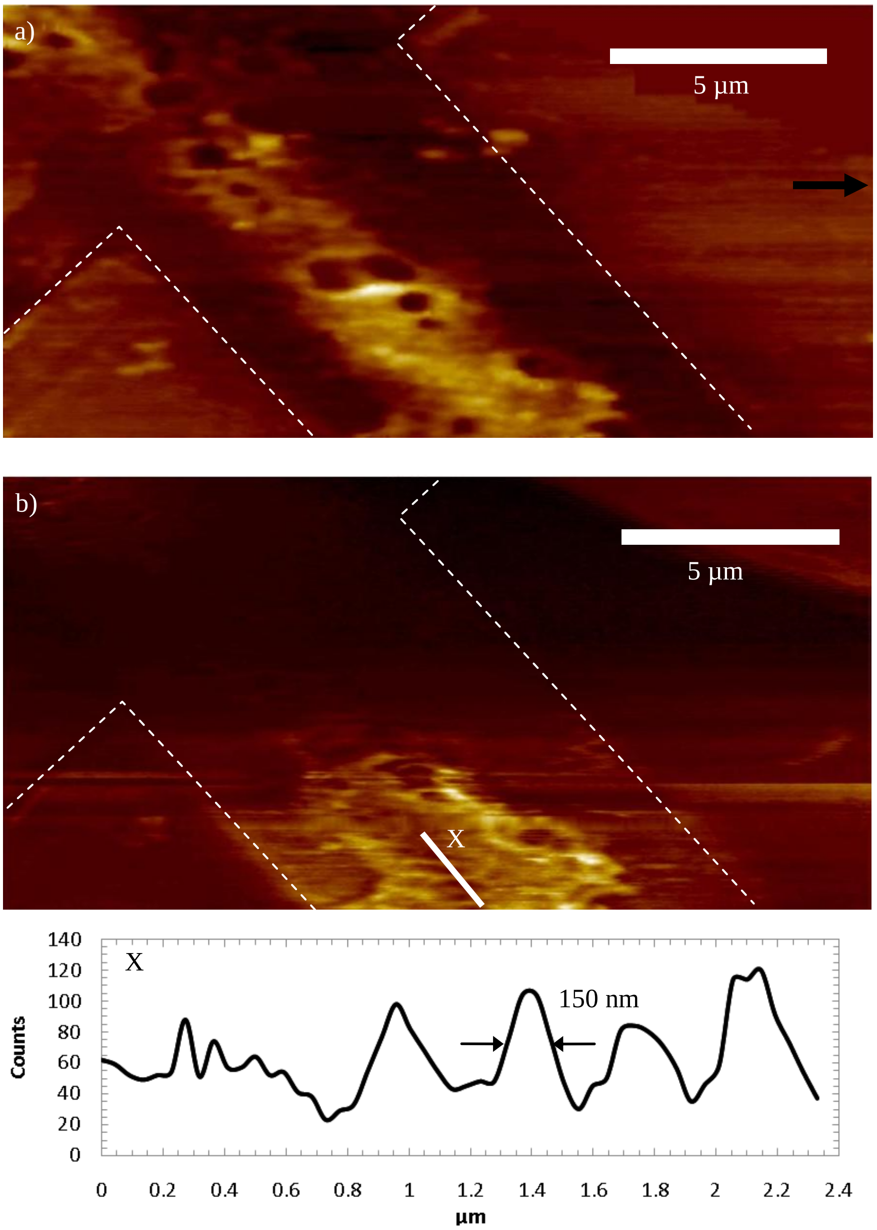

Figure 6.14: a) 20 µm x 10 µm topography, colour scale 125nm, and b) photoluminescence, colour scale 300 counts, obtained simultaneously. Dashed lines are a guide for the eye highlighting the electrodes. X presents a cross-section through the PL image indicating features with FWHM of ~150 nm are resolved.

The lower part of the photoluminescence image shows that the polymer fibres remain luminescent after deposition, with bright features highlighting not only the main fibre, but also outlying polymer fibrils on the electrode surface which appear only faintly in the topographic image. Importantly, these smaller features, and the lack of luminescent contrast seen from the electrodes, indicate that the luminescence signal is not simply a result of topographic convolution. Beginning close to the arrow shown in Figure 6.14a) a very large, ~700 nm high structure enters the topographic image (this has been digitally removed from the presented topography for clarity). Correlated with the appearance of this structure, the photoluminescence signal rapidly fades away. It is not clear whether damage to the probe aperture occurred at this point, or a gradual bleaching of the polymer fibre. In any case, no further PL imaging of this structure was possible.

6.2.3. Polarisation SNOM of supramolecular fibres

As has been shown in section 4.5, the near field from the SNOM is itself polarised. However, it is hoped, as in section 6.1.3, that this polarisation will be sufficiently well mixed that a range of polarised modes, if they exist, will be excited in the sample such that the initial polarisation asymmetry manifests itself only as a difference in overall intensity between orthogonal polarisation directions, and not a change in local contrast. In addition, contrast is expected to be reduced due to reflections from the sample surface contributing to the signal. A 10 × 20 μm area was imaged using the arrangement described previously and utilising a polariser in the collection optics, first with the polarizer aligned vertically (in the plane of the slow scan direction, y) the second with the polarizer aligned horizontally (in the plane of the fast scan direction, x). Due to the length of the acquisition, while these images were taken sequentially, they were obtained 6 hours apart. Figure 6.15 presents the simultaneous topographic and PL images taken in the two polarisation regimes. It can be seen by comparing the two topographic images and observing asymmetry in the (assumed circular) voids that gradual drift in the sample, likely thermal in origin, slightly skews a) and c). Images b) and d) do not exhibit significant drift; after continuous scanning (and possible disturbance following rotation of the polariser) the stage appears to have stabilised at a position slightly offset from the first acquisition. No clear sign of electrode orientation is evident in these images, though the presence in the central region of the images of a dark region of PL combined with flat topography is suggestive of the electrode location.

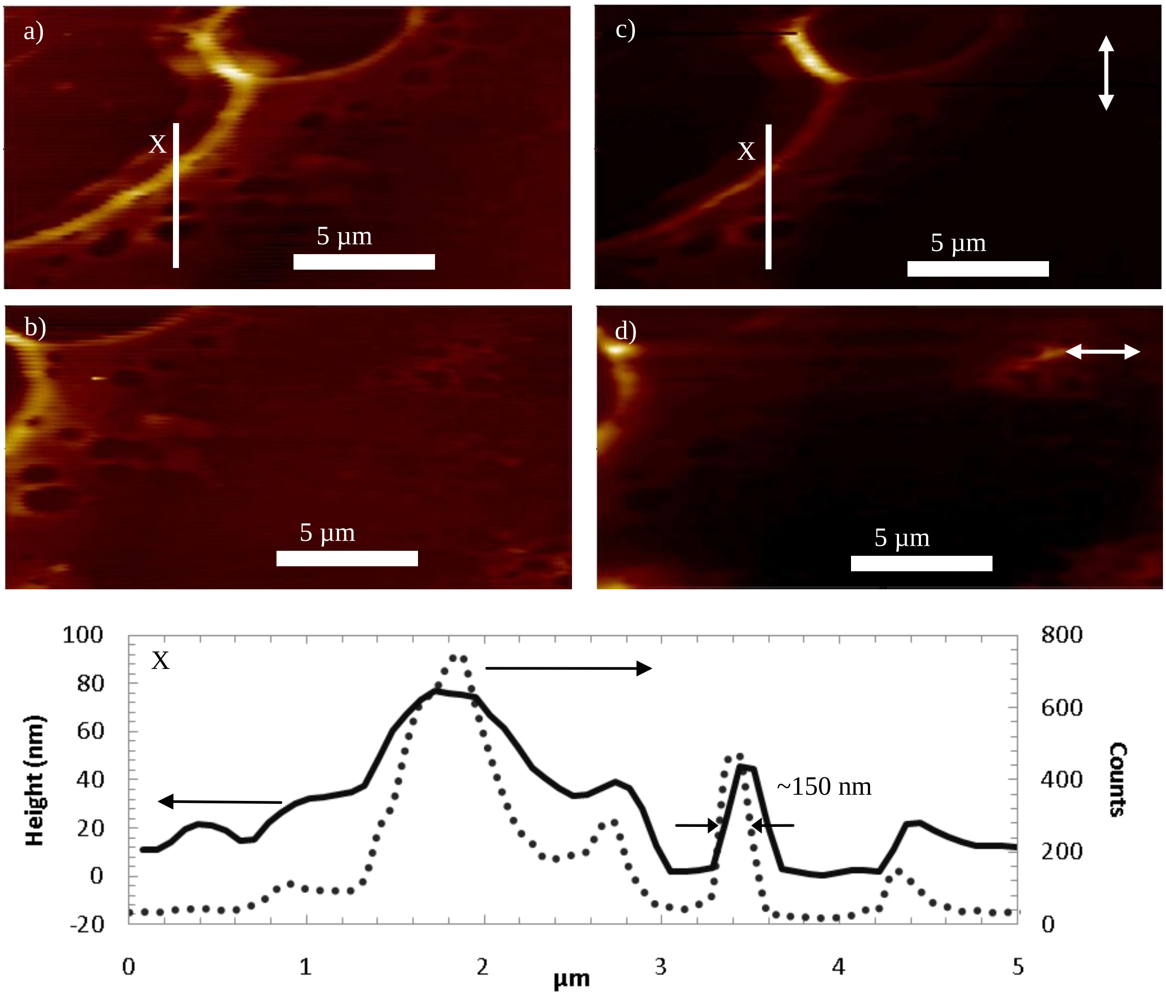

Figure 6.15: 20 × 10 µm images of nominally the same film region showing a, b) topography with vertical range 295 nm and 220 nm respectively, and c, d) photoluminescence with vertical range 1800 counts and 325 counts, respectively. Image c) shows collected light polarised in the vertical plane, d) shows polarised light collected in the horizontal plane. Cross-sections X show superimposed topography and PL for one of the more structured areas of the film, with ~150 nm features resolved in both. The slight offset between the two traces indicates the topographic and PL probes are not quite coaxial.

From the region of the fibre common to both images, no significant difference in contrast is observed, though 6 times more signal is collected in the case of the horizontally aligned polariser. This is likely due to the relative orientation of the illumination polarisation, but may also represent degradation of the aperture during scanning. As in the previous image, comparison of cross-sections X show that features with FWHM of order 150 nm can be resolved using the SNOM. Though topography-induced luminescence contrast cannot be ruled out in this case, by comparison with Figure 6.14 the polymer features seen are expected themselves to be luminescent.

6.3. Conclusions

It has been shown here that SNOM may be extended to the imaging of self-assembled nano- and micro-structures other than blends, while maintaining peak lateral resolution of order 150 nm. The ability to achieve material contrast has also been demonstrated, though in this instance it was not possible to identify any significant substructure within the features imaged. Polarisation contrast within the near-field images taken was not observed, indicating that only weak polarised emission exists in the physical structures. Nevertheless, it would be beneficial to identify a system where polarisation contrast is known to occur on sub-micron scales, and so ensure that this system is capable of discerning such contrast.

In addition to some of the benefits of the SNOM system for high resolution imaging, various limitations have been encountered and illustrated. In particular, the slow acquisition speed and delicacy of the scanning probe mean that repeat images of large areas is hard to achieve reproducibly, especially where physical contact with the system is required – e.g. to switch laser excitation or polariser orientation. Further automation if this particular instrument would be necessary if the kind of measurements described were to become more commonplace, and would also be needed to allow for mid-acquisition switching of collection filters.

Finally, both the versatility of the SNOM system for simultaneous measuring of topography, and the limitations this entails when large topography is encountered has been shown. Topographic artefacts, as illustrated, can significantly limit the usefulness of SNOM[181], creating luminescence “shadows” from which no signal can be obtained due to the increased distance between the surface and excitation source. The problem arises due to the relatively poor quality of the topographic probe compared to the optical probe, and compared to specialised topographic probes such as AFM tips – in essence, topography is measured only as an afterthought. To solve this, the tips would need to be redesigned to raise the importance and reliability of the topographic probe, for instance by specifically incorporating a sharp dielectric or conducting spike close to the aperture allowing the system to cope better with non-ideal samples and potentially locally enhance the near field.

7. Field-assisted alignment of supramolecular fibres

Molecular wires, consisting of either a single molecule [182-184] or supramolecular fibres [185] placed between a pair of electrodes, constitute the most basic component required for the growing field of molecular electronics. While extensive work on single molecule components has received considerable attention, the use of supramolecular architectures rather than single molecules can improve the resilience and electrical properties of devices made from them [186, 187]. One significant problem in studying the behaviour of individual wires, or networks of fibres, is successfully aligning the molecules between metallic electrodes for testing. Several techniques are commonly used to attach and measure molecular wires, including forming a temporary junction between a sample and the tip of a conductive AFM [188-190], or a mercury drop [191] and a substrate, break junctions [184] and lithographically tailored nanoelectrodes [192]. However, few of these are easily scaled up to allow large numbers of devices to be fabricated.

One scalable approach to controlling the alignment of functional molecules, if not necessarily their position, is the use of an electric field to manipulate and align suitable anisotropic objects. The technique has been successfully applied to structures including metal and semiconducting nanoparticles [192] and nanowires [193], DNA molecules [194], carbon nanotubes [195, 196], block copolymers [197], hybrid organic complexes [198] and dendron rod-coil ribbons [199]. Understanding how such a technique could be used to align supramolecular fibres between suitable electrodes is therefore of significant interest.

7.1. Fibre deposition

The gel-forming functionalized 1,3,5-triamide *cis,cis*-cyclohexane derivative (cyclohexane trisamide gelator, CTG, Figure 7.1) is known to self-assemble into supramolecular fibres in solution through the formation of hydrogen bonds [200, 201]. In the gel, the three intermolecular hydrogen bonds (highlighted in Figure 7.1) are parallel to one another and perpendicular to the plane of the cyclohexane ring, encouraging 1D self-assembly and potentially giving the resulting structure a strong dipole moment. Fibres of this material were deposited from 2 mg/ml 1-octanol solution onto pairs of gold electrodes separated by a 5 µm gap. The electrodes were fabricated by Focused Ion Beam (FIB) milling of a 20 nm thick gold layer deposited by sputter coating on an insulating silicon wafer bearing an 85 nm thick thermally grown layer of silicon dioxide. Electrodes were fabricated by Dr Laura Sardone and co-workers at ISIS and Bologna [44] and imaged using SEM and AFM at the same institutions. During deposition, a DC voltage was applied between the two electrodes while the system was cooled slowly to room temperature from 80°C, corresponding to its sol-gel transition temperature.

After drying, micron-scale CTG fibre bundles were observed to have deposited preferentially on the negatively charged electrode while the SiO_x/Si remained largely clear of material (Figure 7.1). This behaviour may be similar in origin to the preferential adsorption of carbon nanotubes on to positive electrodes observed in some systems, which has been previously assigned to the molecules becoming charged either due to defects in production or as part of the deposition process [196]

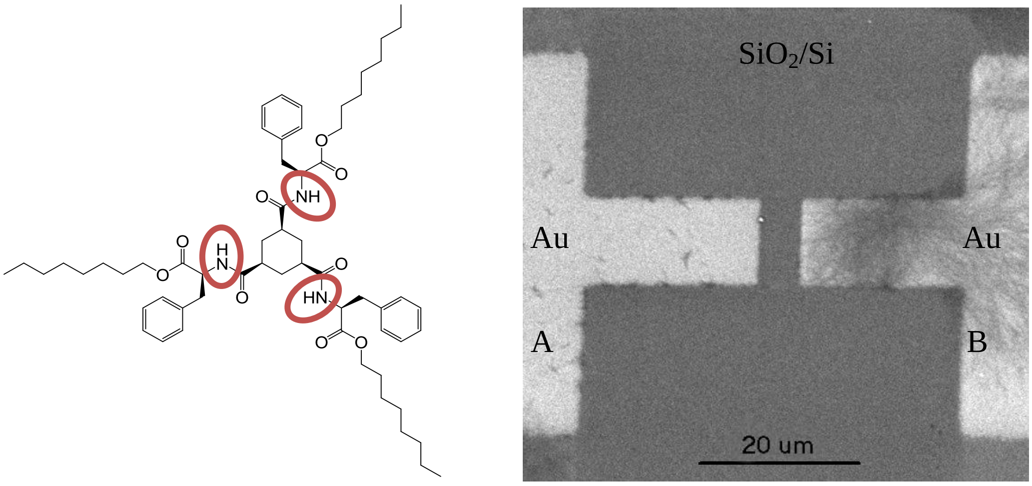

Figure 7.1: (left) Chemical structure of CTG, highlighting the NH groups thought to be responsible for hydrogen bonding. (right) Scanning Electron Microscopy image highlighting the selective adsorption on the negative electrode B of oriented fibres after applying a bias of 2V between the electrodes for 1 hour, while cooling the sample to room temperature. Reproduced from [44].

More strikingly, the bundles of fibres on top of the negative electrode shown in Figure 7.1 do not appear to be randomly oriented. Instead, the gel shows a directed alignment in the presence of the DC field, which is absent when no field is present. Figure 7.2a shows a larger scale SEM image of fibres deposited on top of one pair of electrodes, across which a 2V bias has been applied. Figure 7.2b shows an area of fibres deposited at the same time on a different electrode pair, under identical conditions but without an applied bias. Insets show two-dimensional FFTs measured across 5 × 5 µm squares centred on selected points on both images to characterise the relative alignment of the fibre bundles. These images imply that a field is not needed for the formation of the fibres, as proven by the presence of fibres even on the unbiased electrode, but that the alignment of the fibres is primarily driven by the presence of an electric field above and between the electrodes.

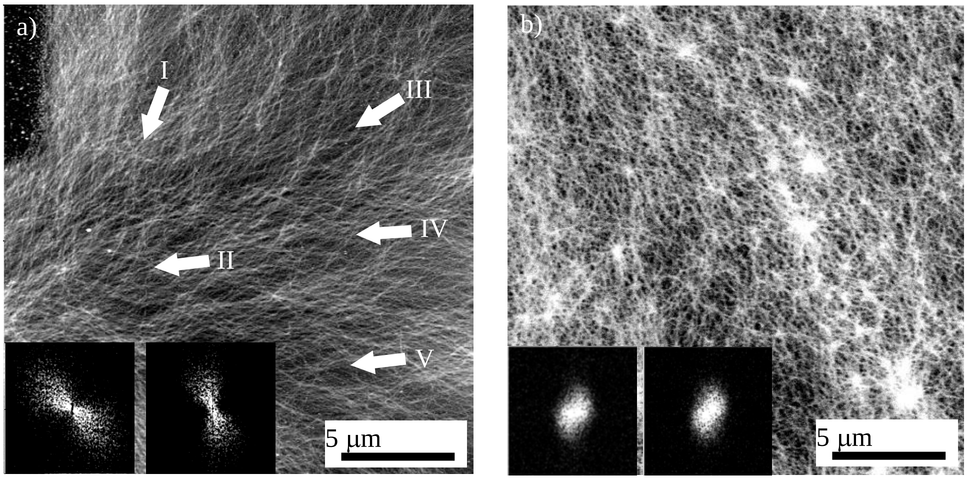

Figure 7.2: a) Inverted-contrast SEM image of the biased Au electrode coated by CTG fibres. The insets display the 2D Fast-Fourier transforms (FFTs) calculated on a 5 × 5 μm^2 area centred on two representative points (I and II) of the image. b) Inverted-contrast SEM image of fibres deposited on an unbiased electrode showing an isotropic orientation of the fibrils. The insets display two FFTs calculated on random 5 × 5 μm^2 areas. Reproduced from [44].

7.2. Modelling of the electric field

To understand the observed local alignment of CTG fibres seen in Figure 7.2a) the DC electric field in the vicinity of the electrodes was modelled using the COMSOL Multiphysics finite element analysis package (COMSOL Inc, USA). The model comprises two 20 nm thick gold electrodes overlaid on a 100 × 110 µm slab of insulating substrate and submerged in 500 nm of weakly conducting liquid, representing the CTG in 1-octanol solution. The electrodes are separated by a 5 µm gap and a total bias of 2V is applied across them (Figure 7.3).

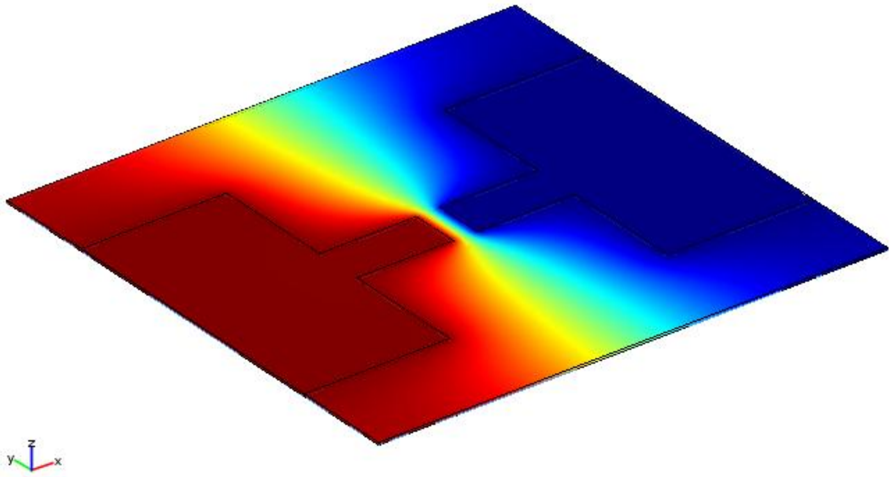

Figure 7.3: Electric potential in plane of electrode surface, scale runs from red +1V to blue -1V.

Current flowing through the system leads to a potential drop across the gold, giving rise to a small electric field component in the vicinity of the electrodes. To determine the structure of this field, the conductive properties of the materials in the system must first be quantified. Detailed modelling of the conductivity of sputtered gold is difficult without knowing its polycrystalline structure. However, previous work [202] suggests that the conductivity of a 20 nm sputtered gold film will be of order 5-10 times less than that of the bulk metal, which has typical conductivity of 4.5-5.0 × 10^7 S/m. The electrodes are therefore modelled as a metal with conductivity $\sigma_{gold} = 5 \times 10^6$ S/m.

The conductivity of the 1-octanol solution, σ_{sol}, is harder to quantify, since it will range over many orders of magnitude depending on the concentration of ions in the liquid. An additional problem arises because, given the fixed 2V bias, varying σ_{sol} necessarily affects the current flowing through the system. For low currents, the strength of the electric field above the electrodes approaches the same order as the numerical errors in the simulation. In practice, this numerical noise forces a lower bound on the solution conductivity of $\sigma_{sol} \geq 100$ S/m, which is used here. This corresponds to a minimum current of a few hundred micro-amps, several orders of magnitude higher than in the real system.

By examining the behaviour of the model over a range of σ_{sol} values however, it was found that the structure of the electric field present around the electrodes does not vary strongly provided that $\sigma_{sol} << \sigma_{gold}$, which will certainly be the case.

Figure 7.4 presents results for electric field strength and direction in the regime described above. It can be seen that the field above the electrodes is weak, of order 1V/cm, and exhibits a transverse component with structure strongly reminiscent of that displayed by the CTG fibres.

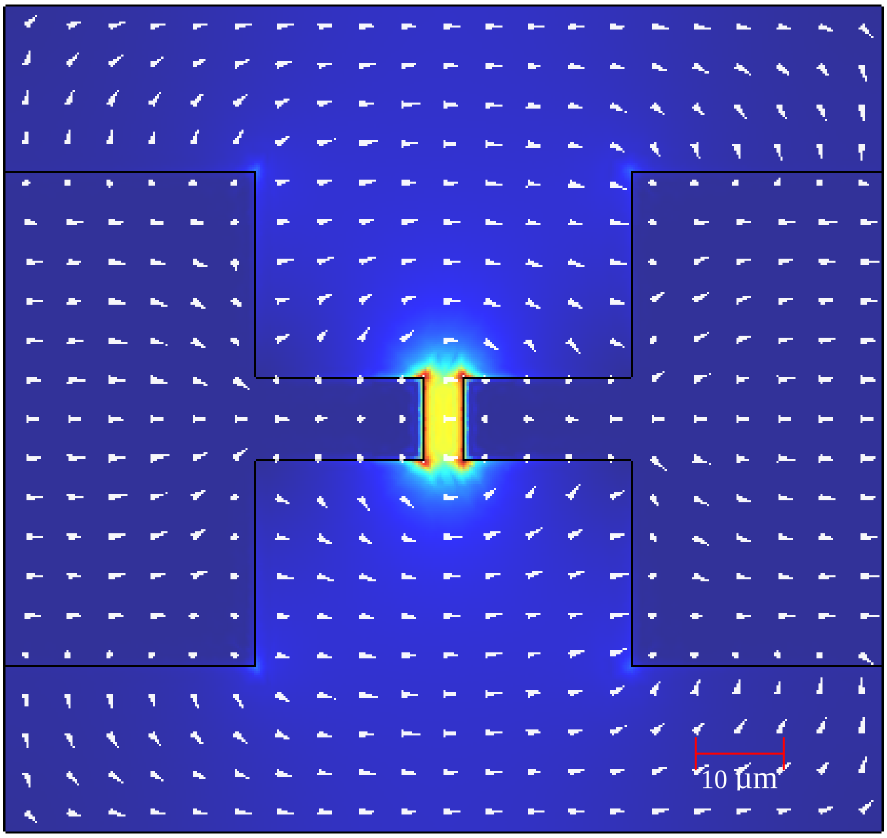

Figure 7.4: Finite element analysis modelling of the electrode structure as described in the text, with $\sigma_{gold} = 5 \times 10^6$ S/m and $\sigma_{sol} = 100$ S/m. Colouring indicates electric field strength in a plane 20 nm above the electrodes. Arrows indicate the three-dimensional direction of this field. Colour scale runs from 0 V/cm (blue) to 5 kV/cm (red).

To quantify the structure if this field, electric field stream-lines are constructed throughout the liquid layer in order to visualise the local field orientation. Insets (c-g) in Figure 7.5 show 5 × 5 µm stream line plots centred on points (I-V) while insets (h-l) present the 2D FFTs of these images. The strong similarity between the calculated field configuration and the orientation of adsorbed CTG fibres suggests that this orientation is very likely due to alignment of CTG dipoles with the local electric field during the adsorption process.

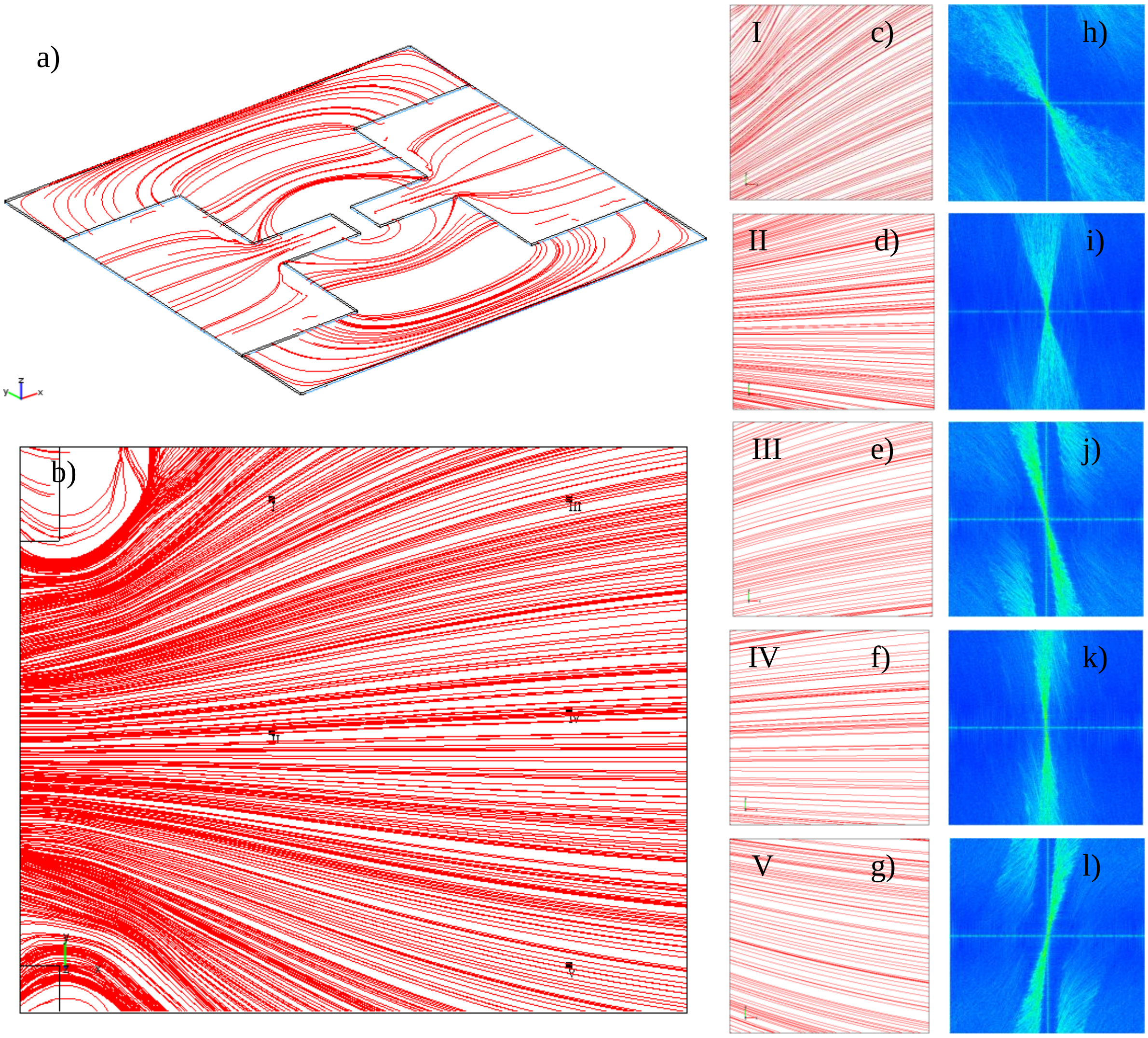

Figure 7.5: a) Overview of the electrode system showing general orientation of electric field streamlines. b) Simulated reproduction of the region imaged in Figure 7.2, with points (I-V) coinciding with the equivalent points in Figure 7.2a). Insets c-g, centred on (I-V) respectively, present 5 × 5 µm plots of the local electric field streamlines, collapsed into a single plane. The unequal spacing of the lines results from the non-uniform distribution of starting points used by the streamlining algorithm and is not intended to indicate field strength. Insets h-l are the 2D FFTs of these images, with arbitrary scale.

7.3. Comparison to experiment

The orientation of fibres within each area of either the simulated or measured images can be quantified using a standard 2D FFT. For each orientation angle α in the plane, the amplitude A of the angular spectrum may be calculated as:

$$A(\alpha)=\sum_{i=1}^{M/2-1}\left|F(M/2+i\cos(\alpha)\,,\,M/2+i\sin(\alpha))\right| \quad (7.1)$$

where $F(u,v)$ are the Fourier components of the image in reciprocal space and M is the number of angles over which α is defined (determined by the image resolution), with

(M/2, M/2) representing the DC contribution. The angle α_{max} having the highest amplitude A_{max} will be perpendicular to any preferred orientation of the image. In this case, it will pick out local alignment of fibres or streamlines.

To further quantify the degree of alignment in a particular area, the texture direction index S, was calculated from an average of A_{max} over the discrete spectral components $A(\alpha_i)$, such that:

$$S = \frac{\sum_{i=0}^{M-1} A(i\pi / M)}{M\, A_{\max}} \tag{7.2}$$

S tends to 0 for images with a single dominant orientation, and to 1 for isotropic patterns. Calculation of S and α_{max} was performed using SPIP. Table 2 presents measurements of α_{max} and S calculated at equivalent positions on the negative electrode (Figure 7.2) and simulation (Figure 7.5) from the 2D FFTs shown therein. For comparison, the S value for the unbiased electrode was found to be 0.88, with a broad angular spread.

Table 2: Measurements of S and $\alpha_{\max}$+90° for 5 × 5 µm streamline zones and SEM images centred on points I-V. Uncertainties on $\alpha_{\max}$ taken from typical spread of the angular spectrum

	Zone	**I**	**II**	**III**	**IV**	**V**
Simulation	$\alpha_{\max}$+90°	225±10°	186±10°	195±10°	182±5°	168±10°
	S	0.456	0.457	0.389	0.356	0.398
Experiment	$\alpha_{\max}$+90°	246±10°	186±10°	215±10°	184±10°	185±10°
	S	0.78	0.69	0.77	0.71	0.72

Comparing of the α_{max} and S for the simulation and the experiment shows that the alignment of the fibres does indeed follow the local alignment of the electric field, demonstrating that the technique causes the fibres to preferentially align. The texture direction indices for the experiment are significantly higher than those of the model. This arises from experimental noise in the real system, including thermal fluctuations and solvent effects as well as dynamic factors affecting the growth of the gel. The indices are significantly less than the index calculated from the isotropic fibres however.

7.4. Conclusions

In summary, is has been shown that supramolecular fibres can indeed be manipulated with a DC electric field, with the fibres adopting a preferential alignment along the field lines likely due to induced dipole effects. The induced alignment was quantified and compared to the stream-line orientation of an electric field simulated using finite-element analysis, with good qualitative and quantitative agreement. However, it has also been shown that the fibre alignment is not perfect, with significantly increased texture direction index compared to the randomly distributed streamlines. As described, this is most likely due to thermal effects being able to compete with the relatively low field energy above the electrodes. If the gel could be encouraged to form in the gap, either by reducing the electrode potential, generating an AC field or modifying the substrate material, then the much stronger field might allow a greater degree of alignment to be achieved.

8. References

1. Letheby, H., *On the production of a blue substance by the electrolysis of sulphate of aniline* Journal of the Chemical Society, 1862. **15**.
2. Little, W.A., *Possibility of Synthesizing an Organic Superconductor.* Physical Review, 1964. **134**(6A): p. A1416.
3. McNeill, R., et al., *Electronic Conduction in Polymers. I. The Chemical Structure of Polypyrrole.* Australian Journal of Chemistry, 1963. **16**(6): p. 1056-1075.
4. De Surville, R., et al., *Electrochemical chains using protolytic organic semiconductors.* Electrochimica Acta, 1968. **13**(6): p. 1451-1458.
5. McGinness, J., P. Corry, and P. Proctor, *Amorphous Semiconductor Switching in Melanins.* Science, 1974. **183**(4127): p. 853-855.
6. Chiang, C.K., et al., *Electrical Conductivity in Doped Polyacetylene.* Physical Review Letters, 1977. **39**(17): p. 1098-1101.
7. Burroughes, J.H., C.A. Jones, and R.H. Friend, *New semiconductor device physics in polymer diodes and transistors.* Nature, 1988. **335**(6186): p. 137-141.
8. Tang, C.W. and S.A. van Slyke, *Organic electroluminescent diodes.* Applied Physics Letters, 1987. **51**(12): p. 913-915.
9. Burroughes, J.H., et al., *Light-emitting diodes based on conjugated polymers.* Nature, 1990. **347**(6293): p. 539-541.
10. Forrest, S.R., *The path to ubiquitous and low-cost organic electronic appliances on plastic.* Nature, 2004. **428**(6986): p. 911-918.
11. Akcelrud, L., *Electroluminescent polymers.* Progress in Polymer Science, 2003. **28**(6): p. 875-962.
12. Bogdal, D. and A. Boron, *Polymer materials used as electroluminescent layers.* Polimery, 1999. **44**(10): p. 646-655.
13. Sirringhaus, H., et al., *High-resolution inkjet printing of all-polymer transistor circuits.* Science, 2000. **290**(5499): p. 2123-2126.
14. Thompson, B.C. and J.M. Fréchet, *Polymer-Fullerene Composite Solar Cells. Angew. Chem., Int. Ed.*, 2008. **47**(1): p. 58-77.
15. Perissinotto, S., et al., *Ultrafast optical switching in distributed feedback polymer laser.* Applied Physics Letters, 2007. **91**(19): p. 191108.
16. Clark, J., et al., *Blue polymer optical fiber amplifiers based on conjugated fluorene oligomers.* Journal of Nanophotonics, 2008. **2**: p. 17.
17. Basescu, N., et al., *High electrical conductivity in doped polyacetylene.* Nature, 1987. **327**(6121): p. 403-405.
18. Förster, T., *Zwischenmolekulare Energiewanderung und Fluoreszenz.* Annalen der Physik, 1948. **437**(1-2): p. 55-75.
19. Dexter, D.L., *A Theory of Sensitized Luminescence in Solids.* The Journal of Chemical Physics, 1953. **21**(5): p. 836-850.
20. Martens, H.C.F., H.B. Brom, and P.W.M. Blom, *Frequency-dependent electrical response of holes in poly(p-phenylene vinylene).* Physical Review B, 1999. **60**(12): p. R8489.
21. Wannier, G.H., *The Structure of Electronic Excitation Levels in Insulating Crystals.* Physical Review, 1937. **52**(3): p. 191.
22. Frenkel, J., *On the Transformation of light into Heat in Solids. I.* Physical Review, 1931. **37**(1): p. 17.

23. Bredas, J.L., et al., *Charge-transfer and energy-transfer processes in π-conjugated oligomers and polymers: A molecular picture.* Chemical Reviews, 2004. **104**(11): p. 4971-5003.
24. Coropceanu, V., et al., *Charge Transport in Organic Semiconductors.* Chemical Reviews, 2007. **107**(4): p. 926-952.
25. Flory, P.J., *Thermodynamics of High Polymer Solutions.* The Journal of Chemical Physics, 1941. **9**(8): p. 660-660.
26. Huggins, M.L., *Solutions of Long Chain Compounds.* The Journal of Chemical Physics, 1941. **9**(5): p. 440.
27. Adachi, C., et al., *Nearly 100% internal phosphorescence efficiency in an organic light-emitting device.* Journal of Applied Physics, 2001. **90**(10): p. 5048-5051.
28. Park, S.H., et al., *Bulk heterojunction solar cells with internal quantum efficiency approaching 100%.* Nature Photonics, 2009. **3**(5): p. 297-U5.
29. Peumans, P. and S.R. Forrest, *Very-high-efficiency double-heterostructure copper phthalocyanine/*C_{60} *photovoltaic cells.* Applied Physics Letters, 2001. **79**(1): p. 126-128.
30. Shaheen, S.E., et al., *2.5% efficient organic plastic solar cells.* Applied Physics Letters, 2001. **78**(6): p. 841-843.
31. Liang, Y., et al., *For the Bright Future - Bulk Heterojunction Polymer Solar Cells with Power Conversion Efficiency of 7.4%.* Advanced Materials, 2010. **22**(20): p. E135-E138.
32. Aparna, M., et al., *White organic LEDs and their recent advancements.* Semiconductor Science and Technology, 2006(7): p. R35.
33. Gather, M.C., et al., *Solution-Processed Full-Color Polymer Organic Light-Emitting Diode Displays Fabricated by Direct Photolithography.* Advanced Functional Materials, 2007. **17**(2): p. 191-200.
34. Subramanian, V., et al., *Progress toward development of all-printed RFID tags: Materials, processes, and devices. Proc. of the IEEE,* 2005. **93**(7): p. 1330-1338.
35. Cacialli, F., et al., *Fabrication of conjugated polymers nanostructures via direct near-field optical lithography.* Ultramicroscopy, 2004. **100**(3-4): p. 449-455.
36. Campbell, M., et al., *Fabrication of photonic crystals for the visible spectrum by holographic lithography.* Nature, 2000. **404**(6773): p. 53-56.
37. Cacialli, F. and P. Bruschi, *Site-selective chemical-vapor-deposition of submicron-wide conducting polypyrrole films: Morphological investigations with the scanning electron and the atomic force microscope.* Journal of Applied Physics, 1996. **80**(1): p. 70-75.
38. Rogers, J.A., Z. Bao, and V.R. Raju, *Nonphotolithographic fabrication of organic transistors with micron feature sizes.* Applied Physics Letters, 1998. **72**(21): p. 2716-2718.
39. Rogers, J.A., et al., *Printing Process Suitable for Reel-to-Reel Production of High-Performance Organic Transistors and Circuits.* Advanced Materials, 1999. **11**(9): p. 741-745.
40. Chou, S.Y., P.R. Krauss, and P.J. Renstrom, *Imprint lithography with 25-nanometer resolution.* Science, 1996. **272**(5258): p. 85-87.
41. Dong, B., et al., *Fabrication of High-Density, Large-Area Conducting-Polymer Nanostructures.* Advanced Functional Materials, 2006. **16**(15): p. 1937-1942.
42. Bao, Z., et al., *High-Performance Plastic Transistors Fabricated by Printing Techniques.* Chem. Mater., 1997. **9**(6): p. 1299-1301.

43. Gigli, G., et al., *Holographic nanopatterning of the organic semiconductor poly(p-phenylene vinylene).* Applied Physics Letters, 1998. **73**(26): p. 3926-3928.
44. Sardone, L., et al., *Electric-Field-Assisted Alignment of Supramolecular Fibers.* Advanced Materials, 2006. **18**(10): p. 1276-1280.
45. Yun, M., et al., *Electrochemically Grown Wires for Individually Addressable Sensor Arrays.* Nano Letters, 2004. **4**(3): p. 419-422.
46. Kameoka, J., et al., *Polymeric nanowire architecture.* Journal of Materials Chemistry, 2004. **14**(10).
47. Stabile, R., et al., *Organic-based distributed feedback lasers by direct electron-beam lithography on conjugated polymers.* Applied Physics Letters, 2007. **91**(10): p. 101110.
48. Piner, R.D., et al., *"Dip-pen" nanolithography.* Science, 1999. **283**(5402): p. 661-663.
49. Lim, J.-H. and C.A. Mirkin, *Electrostatically Driven Dip-Pen Nanolithography of Conducting Polymers.* Advanced Materials, 2002. **14**(20): p. 1474-1477.
50. Maynor, B.W., et al., *Direct-Writing of Polymer Nanostructures:â€‰ Poly(thiophene) Nanowires on Semiconducting and Insulating Surfaces.* Journal of the American Chemical Society, 2001. **124**(4): p. 522-523.
51. Granström, M., *Micropatterned luminescent polymer films.* Acta Polymerica, 1998. **49**(9): p. 514-517.
52. Fenwick, O., et al., *Thermochemical nanopatterning of organic semiconductors.* Nat Nanotechnology, 2009. **4**(10): p. 664-8.
53. Szoszkiewicz, R., et al., *High-Speed, Sub-15 nm Feature Size Thermochemical Nanolithography.* Nano Lett., 2007. **7**(4): p. 1064-1069.
54. Riehn, R., et al., *Near-field optical lithography of a conjugated polymer.* Applied Physics Letters, 2003. **82**(4): p. 526-528.
55. Sun, S. and G.J. Leggett, *Matching the resolution of electron beam lithography by scanning near-field photolithography.* Nano Letters, 2004. **4**(8): p. 1381-1384.
56. Kingsley, J.W., et al., *Optical nanolithography using a scanning near-field probe with an integrated light source.* Applied Physics Letters, 2008. **93**(21).
57. Nie, Z.H. and E. Kumacheva, *Patterning surfaces with functional polymers.* Nature Materials, 2008. **7**(4): p. 277-290.
58. Vettiger, P., et al., *The "millipede" - nanotechnology entering data storage.* IEEE Trans. on Nanotechnology, 2002. **1**(1): p. 39-55.
59. Durig, U., et al., *"Millipede" - an AFM data storage system at the frontier of nanotribology.* Tribology Letters, 2000. **9**(1-2): p. 25-32.
60. Humphris, A.D.L., J.K. Hobbs, and M.J. Miles, *Ultrahigh-speed scanning near-field optical microscopy capable of over 100 frames per second.* Applied Physics Letters, 2003. **83**(1): p. 6-8.
61. Lord Rayleigh, *Investigations in optics with special reference to the spectroscope.* Philos. Mag, 1879. **8**: p. 261-274.
62. Fang, N., et al., *Sub-diffraction-limited optical imaging with a silver superlens.* Science, 2005. **308**(5721): p. 534-537.
63. Boto, A.N., et al., *Quantum Interferometric Optical Lithography: Exploiting Entanglement to Beat the Diffraction Limit.* Physical Review Letters, 2000. **85**(13): p. 2733.
64. Synge, E.H., *A suggested method for extending microscopic resolution into the ultra-microscopic region.* Philosophical Magazine, 1928. **6**: p. 356-362.

65. O'Keefe, J.A., *Resolving Power of Visible Light.* J. Opt. Soc. Am., 1956. **46**(5): p. 359-359.
66. Fischer, U.C. and D.W. Pohl, *Observation of Single-Particle Plasmons by Near-Field Optical Microscopy.* Physical Review Letters, 1989. **62**(4): p. 458-461.
67. Malmqvist, L. and H.M. Hertz, *2-Color Trapped-Particle Optical Microscopy.* Optics Letters, 1994. **19**(12): p. 853-855.
68. Courjon, D., K. Sarayeddine, and M. Spajer, *Scanning Tunneling Optical Microscopy.* Optics Communications, 1989. **71**(1-2): p. 23-28.
69. Ash, E.A. and G. Nicholls, *Super-resolution Aperture Scanning Microscope.* Nature, 1972. **237**(5357): p. 510-512.
70. Lewis, A., et al., *Development of a 500 Å spatial resolution light microscope: I. light is efficiently transmitted through λ/16 diameter apertures.* Ultramicroscopy, 1984. **13**(3): p. 227-231.
71. Pohl, D.W., W. Denk, and M. Lanz, *Optical stethoscopy: Image recording with resolution λ/20.* Applied Physics Letters, 1984. **44**(7): p. 651-653.
72. Wessel, J., *Surface-enhanced optical microscopy.* J. Opt. Soc. Am. B, 1985. **2**(9): p. 1538-1541.
73. Zenhausern, F., M.P. O'Boyle, and H.K. Wickramasinghe, *Apertureless near-field optical microscope.* Applied Physics Letters, 1994. **65**(13): p. 1623-1625.
74. Bouhelier, A., *Field-enhanced scanning near-field optical microscopy.* Microscopy Research and Technique, 2006. **69**(7): p. 563-579.
75. Martin, O.J.F., C. Girard, and A. Dereux, *Generalized Field Propagator for Electromagnetic Scattering and Light Confinement.* Physical Review Letters, 1995. **74**(4): p. 526.
76. Martin, O.J.F. and C. Girard, *Controlling and tuning strong optical field gradients at a local probe microscope tip apex.* Applied Physics Letters, 1997. **70**(6): p. 705-707.
77. Valle, P.J., J.J. Greffet, and R. Carminati, *Optical contrast, topographic contrast and artifacts in illumination-mode scanning near-field optical microscopy.* Journal of Applied Physics, 1999. **86**(1): p. 648-656.
78. Milner, R.G. and D. Richards, *The role of tip plasmons in near-field Raman microscopy.* Journal of Microscopy-Oxford, 2001. **202**: p. 66-71.
79. Liu, L. and S.L. He, *Design of metal-cladded near-field fiber probes with a dispersive body-of-revolution finite-difference time-domain method.* Applied Optics, 2005. **44**(17): p. 3429-3437.
80. Furukawa, H. and S. Kawata, *Analysis of image formation in a near-field scanning optical microscope: Effects of multiple scattering.* Optics Communications, 1996. **132**(1-2): p. 170-178.
81. Krug, J.T., E.J. Sanchez, and X.S. Xie, *Design of near-field optical probes with optimal field enhancement by finite difference time domain electromagnetic simulation.* The Journal of Chemical Physics, 2002. **116**(24): p. 10895-10901.
82. Bethe, H.A., *Theory of diffraction by small holes.* Physical Review, 1944. **66**: p. 163.
83. Bouwkamp, C.J., *Diffraction Theory.* Reports on Progress in Physics, 1954(1): p. 35.
84. Stevenson, R. and D. Richards, *The use of a near-field probe for the study of semiconductor heterostructures.* Semiconductor Science and Technology, 1998. **13**(8): p. 882-886.
85. van Labeke, D., D. Barchiesi, and F. Baida, *Optical characterization of nanosources used in scanning near-field optical microscopy.* J. Opt. Soc. Am. A, 1995. **12**(4): p. 695-703.

86. Karrai, K. and R.D. Grober, *Piezoelectric Tip-Sample Distance Control for near-Field Optical Microscopes.* Applied Physics Letters, 1995. **66**(14): p. 1842-1844.
87. Riehn, R., *Optical Near-field Investigations of π-conjugated Polymers*. 2002, University of Cambridge.
88. Betzig, E. and J.K. Trautman, *Near-Field Optics: Microscopy, Spectroscopy, and Surface Modification Beyond the Diffraction Limit.* Science, 1992. **257**(5067): p. 189-195.
89. Naber, A., H. Kock, and H. Fuchs, *High-Resolution Lithography with Near-Field Optical Microscopy.* Scanning, 1996. **18**(8): p. 567-571.
90. Krausch, G., et al., *Near field microscopy and lithography with uncoated fiber tips: a comparison.* Optics Communications, 1995. **119**(3-4): p. 283-288.
91. Smolyaninov, I.I., D.L. Mazzoni, and C.C. Davis, *Near-field direct-write ultraviolet lithography and shear force microscopic studies of the lithographic process.* Applied Physics Letters, 1995. **67**(26): p. 3859-3861.
92. Sun, S.Q. and G.J. Leggett, *Generation of nanostructures by scanning near-field photolithography of self-assembled monolayers and wet chemical etching.* Nano Letters, 2002. **2**(11): p. 1223-1227.
93. H'Dhili, F., et al., *Near-field optics: Direct observation of the field enhancement below an apertureless probe using a photosensitive polymer.* Applied Physics Letters, 2001. **79**(24): p. 4019-4021.
94. Landraud, N., et al., *Near-field optical patterning on azo-hybrid sol-gel films.* Applied Physics Letters, 2001. **79**(27): p. 4562-4564.
95. Patanè, S., et al., *Near-field optical writing on azo-polymethacrylate spin-coated films.* Optics Communications, 2002. **210**(1-2): p. 37-41.
96. Yatsui, T., et al., *Fabrication of nanometric single zinc and zinc oxide dots by the selective photodissociation of adsorption-phase diethylzinc using a nonresonant optical near field.* Applied Physics Letters, 2002. **81**(19): p. 3651-3653.
97. Yin, X., et al., *Near-field two-photon nanolithography using an apertureless optical probe.* Applied Physics Letters, 2002. **81**(19): p. 3663-3665.
98. Sundaramurthy, A., et al., *Toward Nanometer-Scale Optical Photolithography: Utilizing the Near-Field of Bowtie Optical Nanoantennas.* Nano Letters, 2006. **6**(3): p. 355-360.
99. Tseng, A.A., *Recent developments in nanofabrication using scanning near-field optical microscope lithography.* Optics & Laser Technology, 2007. **39**(3): p. 514-526.
100. Comoretto, D., et al., *Optical properties of highly oriented poly(p-phenylene-vinylene).* Synthetic Metals, 2001. **124**(1): p. 53-58.
101. Wessling, R.A., *The Polymerization of Xylylene Bisdialkyl Sulfonium Salts.* Journal of Polymer Science-Polymer Symposia, 1985(72): p. 55-66.
102. Bradley, D.D.C., *Precursor-route poly(p-phenylenevinylene): polymer characterisation and control of electronic properties.* Journal of Physics D: Applied Physics, 1987. **20**(11): p. 1389.
103. Cotton, D.V., et al., *The origin of fine structure in near-field scanning optical lithography of an electroactive polymer.* Journal of Physics D-Applied Physics, 2008. **41**(19): p. 9.
104. Cotton, D.V., et al., *Investigation of the photochemistry of the poly {p-phenylenevinylene} precursor system: Implications for nanolithography (vol 126, art no 174703, 2007).* Journal of Chemical Physics, 2008. **128**(4): p. 2.

105. Prabhu, V.M., et al., *Direct measurement of the spatial extent of the in situ developed latent image by neutron reflectivity.* Journal of Vacuum Science & Technology B, 2007. **25**(6): p. 2514-2520.
106. Lieberman, K., et al., *A light-source smaller than the optical wavelength.* Science, 1990. **247**(4938): p. 59-61.
107. Palik, E.D., *Handbook of optical constants of solids*. 1985: Academic Press, Orlando.
108. Lee, C.K., C.C. Hua, and S.A. Chen, *Single-chain and aggregation properties of semiconducting polymer solutions investigated by coarse-grained Langevin dynamics simulation.* Journal of Physical Chemistry B, 2008. **112**(37): p. 11479-11489.
109. Cotton, D.V., et al., *Investigation of the photochemistry of the poly{p-phenylenevinylene} precursor system: implications for nanolithography.* J Chem Phys, 2007. **126**(17): p. 174703.
110. Fenwick, O.J., *Scanning Near-Field Optical Lithography and Microscopy of Conjugated Polymer Structures*, in *Department of Physics and London Centre for Nanotechnology*. 2007, University College London.
111. Credgington, D., et al., *High-Resolution Scanning Near-Field Optical Lithography of Conjugated Polymers.* Advanced Functional Materials, 2010. **20**: p. 2842-2847.
112. Charas, A., et al., *Photoacid cross-linkable polyfluorenes for optoelectronics applications.* Synthetic Metals, 2008. **158**(16): p. 643-653.
113. Li, X.C., et al., *A blue light emitting copolymer with charge transporting and photo- crosslinkable functional units.* Synth. Met., 1997. **84**(1-3): p. 437-438.
114. Winroth, G., et al., *Polyfluorene-based light-emitting diodes with an azide photocross-linked poly(3,4-ethylene dioxythiophene):(polystyrene sulfonic acid) hole-injecting layer.* Applied Physics Letters, 2008. **92**(10): p. 3.
115. Charas, A., et al., *Use of cross-linkable polyfluorene in the fabrication of multilayer polyfluorene-based light-emitting diodes with improved efficiency.* Applied Physics Letters, 2006. **89**(14): p. 3.
116. Bernardo, G., et al., *Improving polymer light-emitting diodes efficiency using interlayers based on cross-linkable polymers.* Applied Physics Letters, 2007. **91**(6): p. 3.
117. Kawata, S., et al., *Finer features for functional microdevices.* Nature, 2001. **412**(6848): p. 697-698.
118. Voigt, M., et al., *The interplay between the optical and electronic properties of light-emitting-diode applicable conjugated polymer blends and their phase-separated morphology.* Organic Electronics, 2005. **6**(1): p. 35-45.
119. Charas, A., et al., *Synthesis and luminescence properties of a new polyfluorene copolymer with regulated solubility.* Synthetic Metals, 2004. **147**(1-3): p. 275-279.
120. Castro Neto, A.H., et al., *The electronic properties of graphene.* Reviews of Modern Physics, 2009. **81**(1): p. 109-162.
121. Geim, A.K. and K.S. Novoselov, *The rise of graphene.* Nature Materials, 2007. **6**(3): p. 183-191.
122. Li, X., et al., *Chemically Derived, Ultrasmooth Graphene Nanoribbon Semiconductors.* Science, 2008. **319**(5867): p. 1229-1232.
123. Zheng, Y., et al., *Gate-controlled nonvolatile graphene-ferroelectric memory.* Applied Physics Letters, 2009. **94**(16).
124. Tans, S.J., A.R.M. Verschueren, and C. Dekker, *Room-temperature transistor based on a single carbon nanotube.* Nature, 1998. **393**(6680): p. 49-52.

125. Rowell, M.W., et al., *Organic solar cells with carbon nanotube network electrodes.* Applied Physics Letters, 2006. **88**(23): p. 3.
126. Kolb, H.C., M.G. Finn, and K.B. Sharpless, *Click Chemistry: Diverse Chemical Function from a Few Good Reactions.* Angewandte Chemie International Edition, 2001. **40**(11): p. 2004-2021.
127. Hill, J.P., et al., *Self-Assembled Hexa-peri-hexabenzocoronene Graphitic Nanotube.* Science, 2004. **304**(5676): p. 1481-1483.
128. Mynar, J.L., et al., *Radially Diblock Nanotube: Site-Selective Functionalization of a Tubularly Assembled Hexabenzocoronene.* Journal of the American Chemical Society, 2008. **130**(5): p. 1530-1531.
129. Brand, J.D., et al., *Functionalized Hexa-peri-hexabenzocoronenes: Stable Supramolecular Order by Polymerization in the Discotic Mesophase.* Chemistry of Materials, 2000. **12**(6): p. 1638-1647.
130. Kastler, M., et al., *Nanostructuring with a Crosslinkable Discotic Material.* Small, 2007. **3**(8): p. 1438-1444.
131. Paik, C.S. and H. Morawetz, *Photochemical and Thermal Isomerization of Azoaromatic Residues in side Chains and Backbone of Polymers in Bulk* Macromolecules, 1972. **5**(2): p. 171-&.
132. Karageorgiev, P., et al., *From anisotropic photo-fluidity towards nanomanipulation in the optical near-field.* Nat Mater, 2005. **4**(9): p. 699-703.
133. Stiller, B., et al., *Optical patterning in azobenzene polymer films.* Journal of Microscopy, 2005. **219**(3): p. 109-114.
134. Todorov, T., L. Nikolova, and N. Tomova, *Polarization holography. 1: A new high-efficiency organic material with reversible photoinduced birefringence.* Appl. Opt., 1984. **23**(23): p. 4309-4312.
135. Natansohn, A., et al. *Dipolar cooperative motion in amorphous azo copolymers: a molecular addressing possibility*. in *Photosensitive Optical Materials and Devices*. 1997. San Jose, CA, USA: SPIE.
136. Natansohn, A., et al., *Azo polymers for reversible optical storage. 1. Poly[4'-[[2-(acryloyloxy)ethyl]ethylamino]-4-nitroazobenzene].* Macromolecules, 1992. **25**(8): p. 2268-2273.
137. Rochon, P., E. Batalla, and A. Natansohn, *Optically Induced Surface Gratings in Azoaromatic Polymer-Films.* Applied Physics Letters, 1995. **66**(2): p. 136-138.
138. Darracq, B., et al., *Photoinscription of Surface Relief Gratings on Azo-Hybrid Gels.* Advanced Materials, 1998. **10**(14): p. 1133-1136.
139. Karageorgiev, P., et al., *Modification of the Surface Potential of Azobenzene-Containing Langmuir-Blodgett Films in the Near Field of a Scanning Kelvin Microscope Tip by Irradiation.* Langmuir, 2000. **16**(13): p. 5515-5518.
140. Mori, W., et al., *Nano-fabrication of azopolymer by scanning near-field optical microscope.* Electronics and Communications in Japan (Part II: Electronics), 2004. **87**(3): p. 55-61.
141. Davy, S. and M. Spajer, *Near field optics: Snapshot of the field emitted by a nanosource using a photosensitive polymer.* Applied Physics Letters, 1996. **69**(22): p. 3306-3308.
142. Lim, S.L., et al., *Conductivity Switching and Electronic Memory Effect in Polymers with Pendant Azobenzene Chromophores.* ACS Applied Materials & Interfaces, 2008. **1**(1): p. 60-71.
143. Tamaoki, N., S. Yoshimura, and T. Yamaoka, *A photochromic memory with a non-destructive read-out property.* Thin Solid Films, 1992. **221**(1-2): p. 132-139.

144. Ambrosio, A., et al., *Shape dependent thermal effects in apertured fiber probes for scanning near-field optical microscopy.* Journal of Applied Physics, 2006. **99**(8): p. 084303-084303-6.
145. Patane, S., et al., *Polarization-maintaining near-field optical probes.* Journal of Microscopy, 2008. **229**(2): p. 377-383.
146. Bublitz, D., B. Fleck, and L. Wenke, *A model for surface-relief formation in azobenzene polymers.* Applied Physics B-Lasers and Optics, 2001. **72**(8): p. 931-936.
147. Available from: http://www.leggett.group.shef.ac.uk/Snomipede.htm.
148. Basu, A.S., S. McNamara, and Y.B. Gianchandani, *Scanning thermal lithography: Maskless, submicron thermochemical patterning of photoresist by ultracompliant probes.* Journal of Vacuum Science & Technology B, 2004. **22**(6): p. 3217-3220.
149. Schaffer, E., et al., *Thermomechanical lithography: Pattern replication using a temperature gradient driven instability.* Advanced Materials, 2003. **15**(6): p. 514-517.
150. Szoszkiewicz, R., et al., *High-speed, sub-15 nm feature size thermochemical nanolithography.* Nano Letters, 2007. **7**(4): p. 1064-1069.
151. Wang, D., et al., *Direct writing and characterization of poly(p-phenylene vinylene) nanostructures.* Applied Physics Letters, 2009. **95**(23): p. 233108-3.
152. Hung, M.T., J. Kim, and Y.S. Ju, *Exploration of thermolithography for micro- and nanomanufacturing.* Applied Physics Letters, 2006. **88**(12): p. 3.
153. Pollock, H.M. and A. Hammiche, *Micro-thermal analysis: techniques and applications.* Journal of Physics D-Applied Physics, 2001. **34**(9): p. R23-R53.
154. Hammiche, A., et al., *Localized thermal analysis using a miniaturized resistive probe.* Review of Scientific Instruments, 1996. **67**(12): p. 4268-4274.
155. Lefevre, S., et al., *Thermal conductivity calibration for hot wire based dc scanning thermal microscopy.* Review of Scientific Instruments, 2003. **74**(4): p. 2418-2423.
156. Mills, G., et al., *Scanning thermal microscopy using batch fabricated thermocouple probes.* Applied Physics Letters, 1998. **72**(22): p. 2900-2902.
157. Dyba, M. and S.W. Hell, *Focal Spots of Size lambda /23 Open Up Far-Field Florescence Microscopy at 33 nm Axial Resolution.* Physical Review Letters, 2002. **88**(16): p. 163901.
158. Chappell, J., et al., *Correlating structure with fluorescence emission in phase-separated conjugated-polymer blends.* Nat Mater, 2003. **2**(9): p. 616-621.
159. Stevenson, R., et al., *Ultraviolet-visible near-field microscopy of phase-separated blends of polyfluorene-based conjugated semiconductors.* Applied Physics Letters, 2001. **79**(6): p. 833-835.
160. Stevenson, R., et al., *Fluorescence scanning near-field optical microscopy of polyfluorene composites.* Journal of Microscopy-Oxford, 2001. **202**: p. 433-438.
161. Trautman, J.K., et al., *Near-field spectroscopy of single molecules at room temperature.* Nature, 1994. **369**(6475): p. 40-42.
162. Reid, P.J., D.A. Higgins, and P.F. Barbara, *Environment-Dependent Photophysics of Polymer-Bound J Aggregates Determined by Time-Resolved Fluorescence Spectroscopy and Time-Resolved Near-Field Scanning Optical Microscopy.* The Journal of Physical Chemistry, 1996. **100**(10): p. 3892-3899.
163. Jahncke, C.L., M.A. Paesler, and H.D. Hallen, *Raman Imaging with Near-Field Scanning Optical Microscopy.* Applied Physics Letters, 1995. **67**(17): p. 2483-2485.
164. Stockle, R.M., et al., *Nanoscale chemical analysis by tip-enhanced Raman*

spectroscopy. Chemical Physics Letters, 2000. **318**(1-3): p. 131-136.

165. Festy, F., A. Demming, and D. Richards, *Resonant excitation of tip plasmons for tip-enhanced Raman SNOM.* Ultramicroscopy, 2004. **100**(3-4): p. 437-441.
166. De Wilde, Y., et al., *Thermal radiation scanning tunnelling microscopy.* Nature, 2006. **444**(7120): p. 740-743.
167. Huber, A.J., et al., *Simultaneous IR Material Recognition and Conductivity Mapping by Nanoscale Near-Field Microscopy.* Advanced Materials, 2007. **19**(17): p. 2209-2212.
168. Charra, F., et al., *Near-field electroluminescence probe of polymer light-emitting diodes.* Optical Materials, 1999. **12**(2-3): p. 249-253.
169. McNeill, C.R., et al., *Direct photocurrent mapping of organic solar cells using a near-field scanning optical microscope.* Nano Letters, 2004. **4**(2): p. 219-223.
170. McNeill, C.R., et al., *Near-field scanning photocurrent measurements of polyfluorene blend devices: Directly correlating morphology with current generation.* Nano Letters, 2004. **4**(12): p. 2503-2507.
171. Riehn, R., et al., *Local probing of photocurrent and photoluminescence in a phase-separated conjugated-polymer blend by means of near-field excitation.* Advanced Functional Materials, 2006. **16**(4): p. 469-476.
172. Fabre, N., et al., *Optical Near-Field Microscopy of Light Focusing through a Photonic Crystal Flat Lens.* Physical Review Letters, 2008. **101**(7): p. 073901.
173. Xin, H., F.S. Kim, and S.A. Jenekhe, *Highly Efficient Solar Cells Based on Poly(3-butylthiophene) Nanowires.* Journal of the American Chemical Society, 2008. **130**(16): p. 5424-5425.
174. Vandewal, K., et al., *Varying polymer crystallinity in nanofiber poly(3-alkylthiophene): PCBM solar cells: Influence on charge-transfer state energy and open-circuit voltage.* Applied Physics Letters, 2009. **95**(12): p. 3.
175. Luca, G.D., et al., *Self-assembly of discotic molecules into mesoscopic crystals by solvent-vapour annealing.* Soft Matter, 2008. **4**(10): p. 2064-2070.
176. Bertho, S., et al., *Controlling the morphology of nanofiber-P3HT:PCBM blends for organic bulk heterojunction solar cells.* Organic Electronics, 2009. **10**(7): p. 1248-1251.
177. Westenhoff, S., et al., *Supramolecular electronic coupling in chiral oligothiophene nanostructures.* Advanced Materials, 2006. **18**(10): p. 1281-1285.
178. Cacialli, F., et al., *Cyclodextrin-threaded conjugated polyrotaxanes as insulated molecular wires with reduced interstrand interactions.* Nature Materials, 2002. **1**(3): p. 160-164.
179. Cornil, J., et al., *Interchain interactions in organic π-conjugated materials: Impact on electronic structure, optical response, and charge transport.* Advanced Materials, 2001. **13**(14): p. 1053-1067.
180. Palermo, V., E. Susi, and D. Jones, *Morphological and electrical characterization of etched Si wafers.* Journal of the Electrochemical Society, 2004. **151**(9): p. G554-G558.
181. Williamson, R.L., et al., *Are artefacts in scanning near-field optical microscopy related to the misuse of shear force?* Ultramicroscopy, 1998. **71**(1-4): p. 165-175.
182. Nitzan, A. and M.A. Ratner, *Electron transport in molecular wire junctions.* Science, 2003. **300**(5624): p. 1384-1389.
183. Salomon, A., et al., *Comparison of electronic transport measurements on organic molecules.* Adv. Mater., 2003. **15**(22): p. 1881-1890.

184. Mayor, M., et al., *Electric current through a molecular rod - Relevance of the position of the anchor groups.* Angew. Chem.-Int. Edit., 2003. **42**(47): p. 5834-5838.
185. Schenning, A.P.H.J., et al., *Towards supramolecular electronics.* Synth. Met,, 2004. **147**(1-3): p. 43-48.
186. Grimsdale, A.C. and K. Müllen, *The chemistry of organic nanomaterials.* Angew. Chem.-Int. Edit., 2005. **44**(35): p. 5592-5629.
187. Van der Auweraer, M. and F.C. De Schryver, *Organic electronics: Supra solutions.* Nat. Mater., 2004. **3**(8): p. 507-508.
188. Kelley, T.W., E.L. Granström, and C.D. Frisbie, *Conducting probe atomic force microscopy: A characterization tool for molecular electronics.* Adv. Mater., 1999. **11**(3): p. 261-+.
189. Cui, X.D., et al., *Reproducible measurement of single-molecule conductivity.* Science, 2001. **294**(5542): p. 571-574.
190. Gomez-Navarro, C., et al., *Contactless experiments on individual DNA molecules show no evidence for molecular wire behavior.* Proc. Natl. Ac. Sci. USA, 2002. **99**(13): p. 8484-8487.
191. Tran, E., M.A. Rampi, and G.M. Whitesides, *Electron Transfer in a Hg-SAM//SAM-Hg Junction Mediated by Redox Centers.* Angew. Chem. Int. Engl. Ed., 2004. **43**: p. 3835.
192. Bezryadin, A., C. Dekker, and G. Schmid, *Electrostatic trapping of single conducting nanoparticles between nanoelectrodes.* Applied Physics Letters, 1997. **71**(9): p. 1273-1275.
193. Duan, X.F., et al., *Indium phosphide nanowires as building blocks for nanoscale electronic and optoelectronic devices.* Nature, 2001. **409**(6816): p. 66-69.
194. Maubach, G. and W. Fritzsche, *Precise positioning of individual DNA structures in electrode gaps by self-organization onto guiding microstructures.* Nano Letters, 2004. **4**(4): p. 607-611.
195. Chen, X.Q., et al., *Aligning single-wall carbon nanotubes with an alternating-current electric field.* Applied Physics Letters, 2001. **78**(23): p. 3714-3716.
196. Kumar, M.S., et al., *DC electric field assisted alignment of carbon nanotubes on metal electrodes.* Solid-State Electronics, 2003. **47**(11): p. 2075-2080.
197. Morkved, T.L., et al., *Local control of microdomain orientation in diblock copolymer thin films with electric fields.* Science, 1996. **273**(5277): p. 931-933.
198. Li, L.M., et al., *Assembling a lasing hybrid material with supramolecular polymers and nanocrystals.* Nat. Mater., 2003. **2**(10): p. 689-694.
199. Messmore, B.W., et al., *Synthesis, self-assembly, and characterization of supramolecular polymers from electroactive dendron rodcoil molecules.* J. Am. Chem Soc., 2004. **126**(44): p. 14452-14458.
200. Heeres, A., et al., *Orthogonal self-assembly of low molecular weight hydrogelators and surfactants.* Journal of the American Chemical Society, 2003. **125**(47): p. 14252-14253.
201. van Bommel, K.J.C., et al., *Responsive cyclohexane-based low-molecular-weight hydrogelators with modular architecture.* Angewandte Chemie-International Edition, 2004. **43**(13): p. 1663-1667.
202. Cornely, R.H. and T.A. Ali, *Resistivity and Microstructure of Polycrystalline Au Films Deposited by Rf Bias-Diode and Triode Sputtering.* Journal of Applied Physics, 1978. **49**(7): p. 4094-4097.